Heat flux analysis in a single-element LOx/C_3H_8 subscale rocket combustor with reactive-film cooling

Master Thesis

Faculty of Aerospace Engineering
Giacomo Carotti

Delft University of Technology

TU Delft

Heat flux analysis in a single-element LOx/C_3H_8 subscale rocket combustor with reactive-film cooling

Master Thesis

by

Giacomo Carotti

Student Number

4846605

TU Delft Supervisors:	Chiara Falsetti
	Francesca De Domenico
Isar Aerospace SE Supervisor:	Riccardo Simi
Project Duration:	November, 2020 - August, 2025
Faculty:	Faculty of Aerospace Engineering, TU Delft

TU Delft

Acknowledgements

This master thesis marks the end of a long journey, made of ups and downs within my academic carrier. I am grateful for all the people I met along the way, with whom I shared this important chapter of my life. A special thanks goes to Aydin and Vlad, who have always been there in both happy and difficult times. I would also like to thank Gigi, Uncio, and Davidino, who helped me feel home between a Carbonara and a Cannelloni dish.

Academically, I express my sincere gratitude to my TU Delft supervisors Dr. C. Falsetti and Dr. F. De Domenico, and my Isar Aerospace SE supervisor R. Simi, for their thoughtful mentorship and encouragement throughout this research project. I also would like to thank Dr. N. Perakis for his counseling and assistance in the early phase of this thesis, as well as Isar Aerospace SE for providing the experimental infrastructure and the possibility for conducting such a challenging but rewarding research.

Finally, I express my deepest gratitude to my family. Without their patience, unwavering support, and love I would have not been sitting here, typing the final dot of my academic journey.

Giacomo Carotti
Munich, August 2025

Abstract

This research, conducted in collaboration with Isar Aerospace SE, presents a heat transfer analysis on a single-element LOx/Propane subscale rocket combustor with reactive-film cooling. The work aims to firstly reconstruct the time/space-resolved wall heat flux distribution using an inverse method, and secondly to analyze how operating parameters influence the thermal loads.

A series of hot-fire experiments were conducted in a capacitively and film-cooled copper subscale chamber, instrumented with thermocouples in multiple axial and azimuthal locations to capture the thermal response. A solver called RoqFITT was used to compute the heat flux profiles from temperature measurements, by coupling a transient conduction model with an iterative Jacobian-based optimization loop.

The analysis was focused on the throat region, where thermal stress peaks, and relied on visual graphs and statistical tools. Although a strong collinearity between chamber pressure and film ratio emerged, highlighting the limitation of the experimental set-up to fully isolate the contribution of all variables, meaningful trends emerged. Among them are correlations between heat loads and both chamber pressure and pressure instabilities, as well as an optimal film ratio configuration with minimized heat flux.

By computing the wall heat flux from internal temperature measurements, the study provides thermal insight into combustion-driven heat loading without the need to directly model the complex chemical and turbulent flow dynamics occurring inside the chamber. The obtained results form a valuable foundation for further design decisions on regeneratively cooled chambers and multi-element injector configurations, using the innovative LOx/Propane propellant combination.

Contents

List of Figures

List of Tables

Nomenclature

Abbreviations

Abbreviation	Definition
A/D	Analog-to-Digital
CEA	Chemical Equilibrium Analysis
CFV	Critical-Flow Venturi
CH^* / OH^*	Chemiluminescent Radicals
CFD	Computational Fluid Dynamics
CV	Check Valve
DAQ	Data Acquisition
EMF	Electromotive Force
FEM	Finite Element Method
FDM	Finite Difference Method
FVM	Finite Volume Method
GCH4	Gaseous Methane
GN2	Gaseous Nitrogen
GOx	Gaseous Oxygen
HF	High Frequency
ICEM	Integrated Computer Engineering and Manufacturing
LF	Low Frequency
LOx	Liquid Oxygen
MLR	Multiple Linear Regression
$^O/_F$	Oxydizer-to-Fuel Ratio
P&ID	Piping and Instrumentation Diagram
PLC	Programmable Logic Controller
PP	Propane
PR	Pressure Regulator
Roq̇FITT	Rocket Heat Flux Inverse Thermal Tool
RV	Run Valve
SV	Safety Valve
VIF	Variance Inflation Factor

Symbols

Symbol	Definition	Unit
A_{th}	Throat area	[m]
A_e	Exit area	[m]
A_w	Chamber wall surface area	[m]
C	Empirical coefficient	[-]
C^*	Critical-flow Venturi coefficient	[-]
c	Exhaust velocity	[m/s]
c^*	Characteristic velocity	[m/s]
c_p	Specific heat capacity at constant pressure	[J/kg · K]
c_T	Thrust coefficient	[-]
d_{th}	Throat diameter	[m]
F	Thrust	[N]
f	Friction factor	[-]
g_0	Gravitational constant	$\left[\mathrm{m/s^2}\right]$
h	Sensible enthalpy	[J/kg]
h_g	Hot gas convective heat transfer coefficient	$\left[\mathrm{W/m^2 \cdot K}\right]$
h_{cc}	Coolant convective heat transfer coefficient	$\left[\mathrm{W/m^2 \cdot K}\right]$
$H_{p,T}$	Specific enthalpy at defined pressure and temperature	[J/kg]
I_{sp}	Specific impulse	[s]
J	Residual error function	[$\mathrm{W/m^2}$]
k_{cr}	Curvature correction factor	[-]
k_{Pr}	Correction factor for Prandtl	[-]
k_x	Correction factor for start-up transients	[-]
L_{eff}	Effective radiation path length	[m]
M	Molar Mass	[g/mol]
$\dot{m}$	Mass flow rate	[kg/s]
$\dot{m}_{cc}$	Coolant mass flow rate	[kg/s]
$\dot{m}_{core}$	Core mass flow rate	[kg/s]
$\dot{m}_{curt}$	Film mass flow rate	[kg/s]
$\dot{m}_{tot}$	Total mass flow rate	[kg/s]
$\dot{m}_E$	Entrainment mass flow rate	[kg/s]
Nu	Nusselt number	[-]
p	Pressure	[Pa]
p_c	Chamber pressure	[Pa]
p_e	Nozzle exit pressure	[Pa]
p_a	Ambient pressure	[Pa]
p'	Chamber pressure fluctuations	[Pa]
Pr	Prandtl number	[-]
Q	Vector of surface heat flux guesses	[$\mathrm{W/m^2}$]
$\dot{Q}$	Heat transfer rate	[W]
$\dot{q}$	Heat flux rate	[$\mathrm{W/m^2}$]
$\dot{q}_{rad}$	Radiative heat flux	[$\mathrm{W/m^2}$]
$\dot{q}_{loss}$	Heat loss	[$\mathrm{W/m^2}$]
r_{th}	Throat radius of curvature	[m]
Re	Reynolds number	[-]
R_a	Absolute gas constant	[J/kg.K]
R_u	Universal gas constant	[J/kmol.K]
S	Sensitivity matrix	[K/W]
S_h	Volumetric heat source	[$\mathrm{W/m^3}$]
T	Temperature	[K]
T_{aw}	Adiabatic wall temperature	[K]
T_w	Wall temperature	[K]

Symbol	Definition	Unit
T_{tot}	Total temperature	[K]
T_{film}	Film injection temperature	[K]
T_{calc}	Computed temperature	[K]
T_{meas}	Measured temperature	[K]
V_{cv}	Control volume	[m^3]
v_e	Exit velocity	[m/s]
x	Axial position	[m]
α	Thermal diffusivity	[m^2/s]
γ	Specific heat ratio	[-]
λ	Thermal conductivity	[$W/m \cdot K$]
ΔT	Temperature difference	[K]
Δq	Heat flux difference	[W/m^2]
Δx	Position difference	[m]
η_{c^*}	Combustion efficiency	[-]
η_r	Recovery factor	[-]
μ	Dynamic viscosity	[Pa.s]
ρ	Density	[kg/m^3]
σ	Stefan-Boltzmann constant	$\left[W/m^2 \cdot K^4\right]$
Σ	Bart correction factor	[-]
τ	Time delay	[s]
Ψ_r	Reference entrainment ratio	[-]
Θ_x	Film cooling effectiveness at axial position	[-]

1 Introduction

Since the launch of Sputnik I in 1957, marking the dawn of the Space Age, rocket development has largely been driven by government programs. However, over the past two decades, private and commercial entities have entered the sector, spurred by growing interest in space technologies and access. The success of privately funded ventures, most notably SpaceX in 2008, has catalyzed the rise of the NewSpace movement [1]: a global wave of commercial aerospace startups focused on flexible, sustainable, and cost-effective space access.

In addition to technical innovation, this movement has prompted growing concern about the environmental impact of rocket propulsion. Regulatory changes and sustainability targets have accelerated the development of green propellant combinations, with liquid oxygen (LOx) emerging as the leading oxidizer. Fuels such as hydrogen and light hydrocarbons have been proposed to react with LOx due to their cleaner combustion process and favorable storage properties [2].

Within this landscape, Isar Aerospace SE, a Munich-based startup founded in 2018, aims to deliver orbital launch capabilities using LOx/Propane with a gas-generator cycle. Despite notable progress in green propulsion research, particularly in LOx/CH_4 and LOx/Kerosene systems, limited experimental data are available on LOx/C_3H_8 configurations. This thesis aims to investigate the thermal loads in a LOx/Propane subscale rocket combustor through a detailed sensitivity analysis, responding to the current lack of empirical data for this propellant combination in space applications and contributing to the development of Isar Aerospace SE's Aquila engine.

1.1. Motivation

Thermal control is one of the central challenges in the design and operation of liquid rocket engines. The combustion chamber is exposed to extreme heat loads driven by high-pressure, high-temperature reactive flows, requiring cooling strategies tailored to dynamic operating conditions. The ability to predict wall heat fluxes is essential, as it directly shapes the sizing of cooling channels, influences material selection, and constrains allowable run-times and throttle configurations.

From an engineering perspective, these considerations are particularly necessary in the early phases of engine development, when empirical data is limited and design configurations, such as injector geometry, cooling architecture, and chamber scaling, are still under iteration. Single-element subscales serve as foundational test platforms, enabling a systematic evaluation of injector geometries and the possibility of mapping chamber performance under different operating conditions. The use of a hybrid cooling system, by combining capacitive conduction and film cooling, allows for a preliminary assessment of thermal loads during short tests, while preserving the chamber integrity in the event of underestimated heat loads and/or chamber pressure instabilities. Heat flux analysis offers insight into possible thermal constraints and reveals how key operating conditions, such as chamber pressure, mixture ratio, and film injection, affect thermal behavior. This understanding supports informed decision making prior to mid-scale or full-scale engine implementations.

Figure 1.1: Inaugural flight of Spectrum, courtesy of Isar Aerospace SE [3]

From a research viewpoint, subscale single-element combustors provide a uniquely controlled environment for investigating heat transfer phenomena in isolation. Unlike mid- or full-scale multi-element chambers, where interactions between injectors complicate the analysis, single-element configurations allow for cleaner interpretation of localized behaviour, such as flame dynamics and film interaction.

Despite the growing interest in LOx/Propane liquid rocket engines, experimental data remain scarce compared to legacy combinations such as LOx/Methane or LOx/Kerosene, particularly regarding wall heat flux behavior with a reactive-film cooling strategy. This lack of empirical insight poses a challenge in optimizing cooling methods, which are crucial for the reliability and performance of next-generation propulsion systems.

1.2. Research Question

While the motivation has been framed around both practical and academic interest in characterizing thermal behavior within LOx/Propane rocket engines, the scope of this thesis is defined by the following main research question:

"What are the dominant drivers of the wall heat flux in a single-element LOx/Propane capacitive subscale combustor with reactive-film cooling system?"

This question reflects two primary research goals:

- To identify and quantify how wall heat flux responds to key load-point parameter, such as chamber pressure, oxidizer-to-fuel ratio, film-to-core mass-flow ratio and propellant injection temperatures
- To evaluate the role of injector/film-induced asymmetries and circumferential variations in shaping the distribution of thermal loads, captured through azimuthally distributed instrumentation.

The characterization carried out in this thesis builds a foundation for understanding the interaction between operational variables and thermal performance, with the aim of supporting future and preliminary design efforts involving LOx/Propane rocket engines.

1.3. Thesis Outline

In this section, the thesis structure is presented:

- Chapter 2 introduces the theoretical background relevant to heat flux analysis in rocket engines. It reviews basic propulsion principles, details the LOx/Propane propellant combination, explains

the dominant heat-transfer modes in rocketry and list the used cooling methods

- Chapter 3 surveys the literature on heat-flux measurement techniques, focusing on inverse methods and particularly on the RoqFITT solver applications, but it also reviews past sensitivity analyses of similar rocket-engine configurations, highlighting how key operating parameters relate to wall heat flux
- Chapter 4 describes the experimental setup used in the test campaigns, including the test facility fluid system, the subscale assembly chamber and the instrumentation used. The operational procedures and safety logic adopted during hot-fire testing are also discussed
- Chapter 5 presents the methodology employed for computing and analysing the wall heat flux. The RoqFITT inverse solver used for the reconstruction is introduced, together with its working structure and output. The averaging framework is then described, including variable selection and data normalization. Finally, the tools used for the sensitivity analysis are presented, along with an error analysis to support the reliability of the heat flux results
- Chapter 6 provides the main results of the heat flux analysis. It begins with visual observations of the data obtained in the test campaigns, followed by statistical modeling and multivariate interpretation. Key physical trends and dominant operating parameters affecting wall heat flux are here identified and discussed
- Chapter 7 summarizes the findings and conclusions derived from the thermal analysis, answering the initially posed research question
- Chapter 8 concludes the thesis with an outlook, where potential research continuations are discussed, including the transition toward regenerative cooling systems, further film optimization, and multi-element injector configurations.

2

Theoretical Background

To support the heat flux investigation in a subscale rocket chamber, this chapter provides a comprehensive theoretical foundation over propulsion physics, propellant thermodynamics, heat transfer theory, cooling strategies, and heat transfer measurement techniques. After introducing the fundamentals of rocketry, the LOx/Propane propellant combination is analyzed in comparison to more conventional choices, focusing on combustion characteristics, handling, and cooling properties. The dominant modes of heat transfer, conduction, convection, and radiation are then presented, along with key models used for heat flux estimations. The chapter also reviews the various cooling methods applicable to rocket engines, with an emphasis on the capacitive and film cooling approaches adopted in this study. Lastly, the main experimental techniques for wall heat flux measurements in subscale chambers are introduced.

2.1. Basics of Rocket Propulsion

A rocket is generally used to carry payloads into Earth's orbit or for interplanetary missions, while in military applications, rockets are used as missiles. The different types of propulsion systems, classified by their way of generating kinetic energy to accelerate the rocket, are chemical, nuclear, and electric.

In chemical rocket engines, which are by far the most widely used, the energy is released from the molecular bonds of the propellants. The reaction can be of combustion in case two propellants are present (fuel and oxidizer) or of decomposition for a mono-propellant (by use of a catalyst).

A further classification for chemical propulsion systems can be made on the aggregate state of the propellants. Solid rocket engines, which are reliable, durable, and can deliver a high thrust, are usually used for weapons systems or as boosters for the first stages of a launch. Once ignited, the propellant keeps burning until completion, which is why this configuration cannot be used when engine multi-ignition is required. Hybrid propulsion systems instead use propellants in more phases, allowing for start and stop operations, but presenting low efficiencies compared to other possible choices. Finally, liquid rocket engines, which deliver the highest efficiency among the family of chemical propulsion systems, are usually the preferred ones, introducing, however, great complexity and higher design costs.

In addition to chemical propulsion systems, alternative technologies have been explored with varying degrees of development and applicability. Nuclear thermal propulsion, although not yet fully realized, operates by heating a separate working fluid, typically hydrogen, via nuclear reactions, which is then expelled at high velocity to generate thrust. Electric propulsion systems, on the contrary, rely on external power sources, such as solar panels, to accelerate propellants through electric or magnetic fields. Although they offer high efficiency and precise thrust control, their limited power output and dependency on heavy energy systems restrict their use to in-space flights only.

Main equations

To reach space, a rocket needs high velocity and great thrust to escape gravity pull. In 1903, Tsiolkovsky proposed an equation that describes the basic motion of a rocket [4]:

$$\Delta v = v_e \ln\left(\frac{m_0}{m_f}\right) \tag{2.1}$$

Where Δv is the increase in velocity, v_e the exhaust velocity, m_0 the wet mass (including propellant) and m_f the dry mass (without propellant). The concept behind Equation 2.1 is that an object can accelerate itself by expelling part of its mass, therefore producing thrust, and will continue to move due to the conservation of momentum.

The force produced by a rocket engine is made up of two terms, which can be explained using the following simple equation:

$$T = \dot{m} v_e + A_e(p_e - p_a) \tag{2.2}$$

Where $\dot{m}$ is the mass flow of the exhaust gas, while the subscripts e and a stand for exit and ambient, respectively. The first term, which gives the highest contribution to the thrust, is called momentum thrust and is a result of Newton's third law of motion. It is clear how important it is to increase the velocity of the exhaust gas to obtain a high thrust. For this purpose, a convergent-divergent section is used at the end of the cylindrical section of a combustion chamber, in which the flow is accelerated from subsonic to sonic conditions until the throat, and its velocity further increased to supersonic in the divergent part. This acceleration is obtained at the expense of the pressure, which decreases along the process. To better understand this concept, the velocity and pressure profiles are shown with a simple rocket combustor sketch in Figure 2.1.

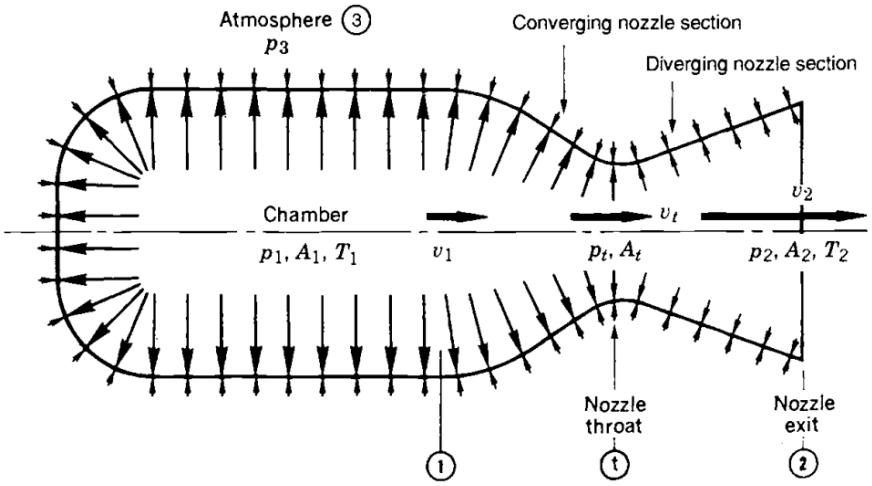

Figure 2.1: Pressure and velocity profile on a rocket combustion chamber [5]

The second term of Equation 2.2 is called pressure thrust and is given by the difference in pressures between exhaust gases and ambient. The optimum thrust is achieved when this term equals zero, so when exit and ambient pressures are equal (adapted nozzle). When a nozzle is under-expanded, the exit pressure is higher than the ambient pressure, and there is momentum loss in the exhaust gas. If a nozzle is over-expanded instead, the pressure thrust simply becomes negative in Equation 2.2, acting in the opposite direction of the momentum thrust.

In order to combine both thrust terms into one, the effective exhaust velocity c is defined as follows:

$$c = v_e + (p_e - p_a)\frac{A_e}{\dot{m}} = \frac{F}{\dot{m}} \tag{2.3}$$

If the right term of Equation 2.3 is divided by the gravitational constant of the Earth g_0, the specific impulse I_{sp} can be defined:

$$I_{sp} = \frac{F}{\dot{m} g_0} \tag{2.4}$$

The specific impulse is an important parameter that is used to characterize a rocket engine, as it is a measure of the efficiency with which an engine creates thrust. It can be referred to either sea-level or vacuum conditions, and it is strongly dependent on the source of energy used for propulsion. For chemical propulsion systems, the I_{sp} range is typically between 200-410 s [5].

In case of bipropellant rocket engines, fuel and oxidizer are combusted, and the ratio between them is defined as follows:

$$O/F = \frac{\dot{m}_{ox}}{\dot{m}_f} \tag{2.5}$$

Another important parameter for the performance analysis of a rocket engine is the characteristic velocity c^*, which is used to identify the effects of the combustion process in the chamber independently of the expansion of the nozzle:

$$c^* = \frac{p_c A_{th}}{\dot{m}} \tag{2.6}$$

The equivalent parameter used to describe the effects of gas expansion in the nozzle independently of the combustion process is the thrust coefficient c_T:

$$c_T = \frac{F}{A_{th} p_c} \tag{2.7}$$

By multiplying c^* and c_T, the effective exhaust velocity is obtained:

$$c^* \cdot c_T = \frac{p_c A_{th}}{\dot{m}} \cdot \frac{F}{A_{th} p_c} = \frac{F}{\dot{m}} = c \tag{2.8}$$

To quantify how efficiently a combustion chamber converts chemical energy into thermal energy, the combustion efficiency η_{c^*} is used:

$$\eta_{c^*} = \frac{c^*_{\text{real}}}{c^*_{\text{ideal}}} \tag{2.9}$$

Where c^*_{real} is obtained from real combustion data, while c^*_{ideal} is computed from thermochemical equilibrium models (such as NASA CEA), based on propellant properties and chamber conditions.

2.2. LOx/Propane Combination

Although a comparison between propane and methane carried out by Martin [6] showed that the former presents higher advantages for single-stage orbit vehicles, LOx/Propane rocket engines have been mainly proposed and tested, but only used once in an orbital launch (on the first test flight of Isar Aerospace SE). In this section, an analysis of propane as a possible rocket fuel is carried out. Characteristics of this propellant such as chemical reaction, performance, handling, and cooling properties are presented and compared to the characteristics of other conventional fuel candidates. Focus is given to the comparison between propane and methane, being the latter the most employed light hydrocarbons used as rocket propellant in the recent years.

Chemical reaction

The chemical reaction of a light hydrocarbon reacting with oxygen under stoichiometric conditions produces water and carbon dioxide, and it can be derived using the following formula:

$$C_aH_b + \left(a + \frac{b}{4}\right) O_2 \rightarrow aCO_2 + \frac{b}{2}H_2O \tag{2.10}$$

Propane, which is a three-carbon alkane with chemical formula C_3H_8, follows therefore the following chemical reaction when reacting with oxygen and at the condition of equivalence ratio equal to 1:

$$C_3H_8 + 5O_2 \rightarrow 3CO_2 + 4H_2O \tag{2.11}$$

For rocket engines, the stochiometric condition is usually not the preferred one because it does not correspond to the highest thrust efficiency.

Methane, which completes the carbon atom with 4 hydrogen atoms (CH_4), has the highest concentration of hydrogen in the light hydrocarbon group. Because the H-C bond requires a higher specific energy to break in comparison to a C-C bond, propane needs a lower amount of energy to react and combust with oxygen. This characteristic translates into the possibility to use smaller and/or less powerful igniters when propane is employed compared to rocket engines fueled by methane.

Performance

Figure 2.2 shows a comparison among LOx/Propane and other typical propellant combinations of ideal vacuum I_{sp} in function of $^{O}/_{F}$, for a chamber configuration with $p_c = 100\ bar$ and $A_e/A_{th} = 45$.

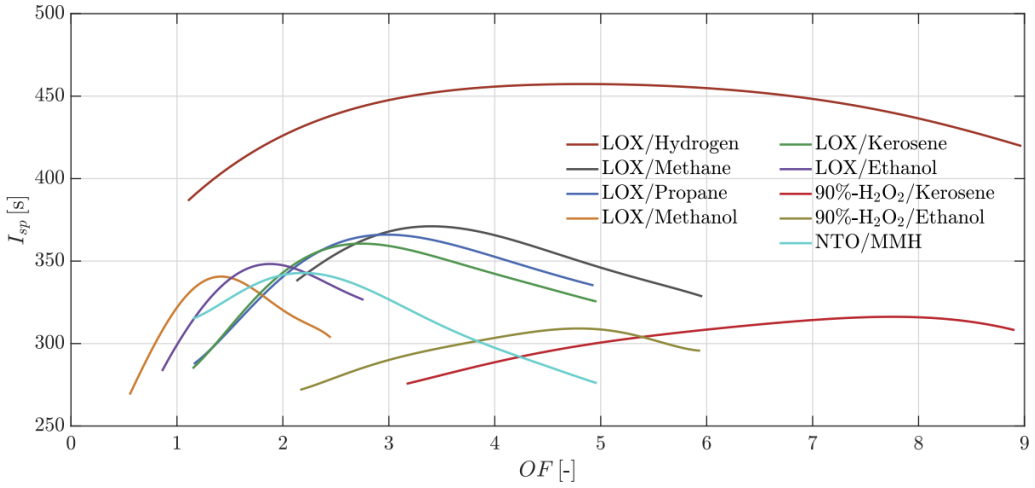

Figure 2.2: Ideal vacuum specific impulse of typical rocket propellant combinations, with p_c = 100 bar and A_e/A_{th} = 45 [7]

Before comparing the actual value of I_{sp} among the propellants, it can be observed that each peak does not correspond to the stoichiometric condition. The reason behind this phenomenon can be explained by analyzing a different form of the effective exhaust velocity formula shown in Equation 2.3:

$$c = \sqrt{\frac{2\gamma}{\gamma - 1}\frac{R_a}{M}T_c\left(1 - \left(\frac{p_e}{p_c}\right)^{\left(\frac{\gamma-1}{\gamma}\right)}\right)} \tag{2.12}$$

Where γ is the specific heat ratio, R_a the absolute gas constant, M the molar mass, T_c the temperature of the combustion gases and p_e/p_c the pressure ratio between the exit and chamber locations. The molar mass of the exhaust gas negatively influences the exhaust velocity (heavier molecules accelerate less

than lighter ones). For this reason, for the propellant combinations of LOx and most fuels in Figure 2.2, the highest peak in I_{sp} is reached under fuel rich conditions (being O_2 heavier than most of the C_xH_y compounds shown). For LOx / Propane, the highest I_{sp} is obtained at $^O/_F \cong 2.9$ (versus the stoichiometric condition of $^O/_F = 3.64$).

By comparing the I_{sp} peak amplitude in Figure 2.2, it is evident that LOx / Hydrogen has by far the highest value. However, for practical reasons, the choice of using light hydrocarbons is usually preferred because of their higher density, which allows the use of smaller tanks, which reduces the structural mass and compensates for the lower I_{sp}, and their easier handling. The advantages of hypergolic propellant combinations such as hydrazine (NTO/MMH) or hydrogen peroxide as oxidizer in allowing for simpler engine configurations by removing the presence of the igniter are countered by their attributes of high toxicity and low specific impulse, respectively. Among light hydrocarbons, the difference in the maximum achievable I_{sp} is relatively small, with methane leading the group and closely followed by propane.

Handling

Although propane and methane belong to the same family of light alkanes, there are significant differences among their thermodynamic properties. It is important to consider these quantities during the selection of a fuel candidate because its phase diagram can give an insight on possible future handling costs. Table 2.1 shows the freezing and boiling temperatures, as well as the critical point of typical rocket propellants and propane.

Table 2.1: Thermodynamic properties of typical rocket propellants and propane [7]

Property	**C_3H_8**	**CH_4**	**RP − 1**	**H_2**	**O_2**
Freezing Temperature [K]	85.5	90.7	226.0	14.0	54.4
Boiling Temperature (1 bar) [K]	231.0	111.6	450.0	20.4	90.6
Critical Temperature [K]	369.8	190.6	679.0	33.1	154.8
Critical Pressure [bar]	42.5	46.0	23.4	12.9	50.4

For storability reasons, it is convenient to keep the propellants in the liquid state. Although propane at room temperature and pressure is in the gaseous state, by slightly increasing its pressure, it can be liquefied. However, methane needs to be pressurized and subcooled to change its phase to liquid, resulting in higher handling costs.

As, on the one hand, storing propellants in the gaseous state is not ideal, on the other hand, their change phase into solid should be avoided. Although methane and propane have a similar freezing point (90.7 K and 85.5 K respectively), the fact that oxygen liquefies at 90.6 K can raise concerns for methane. In the launch vehicle, the two propellant tanks are usually close to each other, and during prelaunch tanking operations, temperatures in the inter-tank compartment can be quite low. When methane is used, insulation between tanks must be employed to prevent the propellant from freezing, leading to an increase in vehicle weight.

Cooling Properties

In the regenerative cooling system of a rocket engine, the fuel is usually chosen as the coolant fluid. Propane and methane have superior cooling properties compared to the other hydrocarbons in nominal wall heat fluxes [8]. Methane has a higher specific heat capacity, while the heat transfer coefficient of propane is greater, as shown in the work by Urbano et al. [9]. Hydrocarbons at high temperatures undergo soot deposition (coking), which reduces the cooling capabilities. Methane has a higher coking limit than propane and kerosene, as shown by Younglove [10] et al. and Gross [11]. On the other hand, when the ratio between wall heat flux and coolant mass flow becomes too high, methane can experience a greater heat transfer deterioration than propane, as described by Nasuti et al. [12].

Given these premises, propane presents several advantages compared to other green propellants. Although its regenerative cooling performances are slightly lower in comparison to methane, as also

summarized in the work of Y. M. Kose et al. [13], the high availability, low cost, and easy handling of propane make it still a valid candidate to be chosen as fuel for rocket engines.

2.3. Heat Transfer Phenomena

During the combustion process in a liquid rocket engine, a small part of the energy produced (from 0.5 to 5 %) is transferred as heat to injector plate, chamber and nozzle walls, which are directly exposed to the hot gases [5]. Most of the heat is transferred by convection, while the remaining part by radiation. Conduction, which is considered negligible from the hot gas to the chamber walls, plays a role only in the heat transfer through the chamber material.

If, on the one hand, having a higher chamber pressure brings greater performance, the increase of heat transfer with chamber pressure imposes limit in the engine design. The most critical part is known to be the throat, where the heat flux reaches the highest peak because of the presence of the smallest cross-sectional area along the chamber/nozzle profile. Injector head and nozzle exit experience instead the lowest amount of heat flux. Figure 2.3 shows a typical axial heat transfer distribution for chemical rocket chambers.

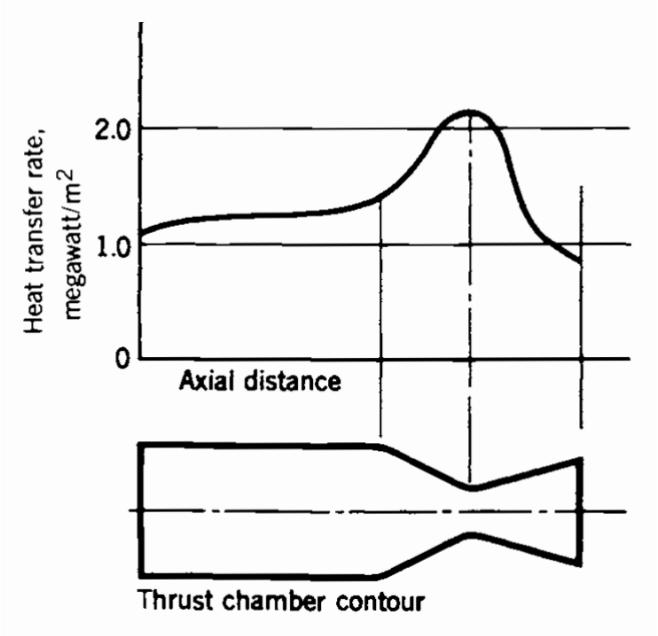

Figure 2.3: Typical axial heat transfer distribution for chemical rocket engines [5]

The study of the heat transfer phenomena is therefore important because it allows to design cooling systems able to ensure a structural integrity of the engine given the high hot gas temperatures in the chamber. In addition, characterizing heat transfer can offer indirect insight into combustion dynamics, as thermal loading patterns are shaped by flame structure, reaction zones, and the spatial distribution of energy release. Although heat transfer analysis does not directly resolve combustion chemistry, it supports a broader understanding of how chemical and thermal processes interact within the chamber. The theory behind conduction, convection, and radiation as well as some empirical models used for the estimation of heat transfer coefficients in rocket chambers are described in the following sub-sections.

Conduction

As previously stated in the introduction to Chapter 2.3, conductive heat transfer from the hot gas to the chamber wall is negligible. Within the chamber material itself, however, the thermal conduction plays a dominant role in transporting heat. The governing equation for this phenomenon is Fourier's law, which, for simple one-dimensional and steady-state applications, is expressed as follows:

$$\dot{Q} = -\lambda A \frac{\Delta T}{\Delta x} \tag{2.13}$$

In the present study, the liquid rocket chamber has a cylindrical shape and therefore Equation 2.13 is reformulated in cylindrical coordinates as:

$$\dot{Q} = 2\pi\lambda l \frac{T_1 - T_2}{\ln\left(r_2/r_1\right)} \tag{2.14}$$

This expression highlights how the temperature distribution within the cylindrical wall material follows a logarithmic profile, unlike the linear trend observed in conduction through a planar slab.

It is important to note that while the total heat transfer rate across the wall remains constant (under one-dimensional assumptions), the local heat flux varies with radius due to the changing surface area available for conduction. Specifically, this variation contributes to localized peaks in heat flux, such as the one observed in the throat region in Figure 2.3, due to the elevated thermal gradients and energy release concentrated in that area.

Convection
In a rocket chamber, most of the heat from the chemical reaction transferred to the walls is attributed to forced convection, which is caused by the temperature gradient between hot gas and chamber wall. Newton's law of cooling describes the convective heat flux:

$$\dot{q} = h_g \left(T_{aw} - T_w\right) \tag{2.15}$$

Where h_g is the convective heat transfer coefficient of the gas, T_{aw} the adiabatic wall temperature while T_w the actual wall temperature.

The adiabatic wall temperature is the temperature that the chamber wall would have in case of adiabatic wall conditions ($\dot{q}_w = 0$). To calculate it, the relation between total and static temperature of the hot gas must be defined first:

$$T_{tot} = T\left(1 + \frac{\gamma - 1}{2} M^2\right) \tag{2.16}$$

With the assumption of ideal isentropic flow, the temperature in the boundary layer increases to the total temperature (since the velocity drops to zero). In rocket chambers, however, the temperature is not fully recovered at the wall due to radiative heat transfer in the boundary layer, resulting in slightly lower values compared to the total temperature [14]. Figure 2.4 shows the temperature profiles in the boundary layer with the adiabatic wall assumption, where T_c is intended as total temperature and T_∞ as static temperature.

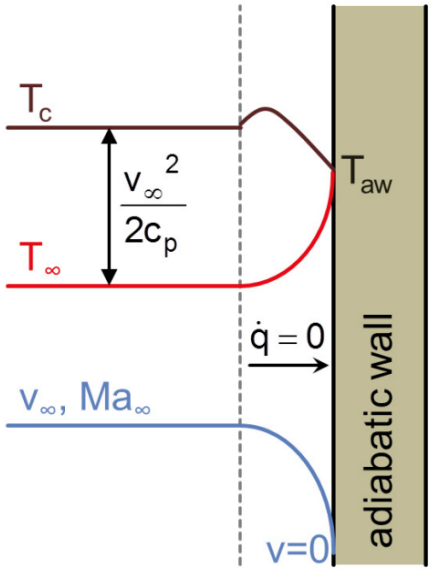

Figure 2.4: Schematic of temperature profiles with adiabatic wall assumption [14]

A recovery factor is therefore introduced and the adiabatic wall temperature is defined:

$$T_{aw} = T\left(1 + \eta_r \frac{\gamma - 1}{2} M^2\right) \tag{2.17}$$

For turbulent flows, the recovery factor is modeled as $\eta_r = \sqrt[3]{Pr}$, where Pr stands for Prandtl number. For practical reasons, since the Prandtl number is considered approximately 1, the adiabatic wall temperature is assumed to be equal to the total temperature.

The convective heat transfer coefficient h_g depends on flow parameters such as viscosity μ, thermal conductivity λ, density ρ, heat capacity c_p and velocity v. Several empirical correlations have been derived in recent years with the aim of describing an average heat transfer coefficient of the hot gas in a rocket chamber. Most of these correlations used the three following dimensionless numbers:

$$Pr = \frac{\mu c_p}{\lambda} \qquad Re = \frac{\rho v d_h}{\mu} \qquad Nu = \frac{h d_h}{\lambda} \tag{2.18}$$

The Prandtl number Pr is the ratio of momentum diffusivity to thermal diffusivity, the Reynolds number Re is the ratio of inertial forces to viscous forces and the Nusselt number Nu is the ratio of convective to conductive heat transfer. The relation among these dimensionless numbers used in the derived empirical correlations usually has the following form:

$$Nu = C \cdot Re^a \cdot Pr^b \cdot corrections \tag{2.19}$$

With C, a and b fitting parameters, while $corrections$ stands for correction functions which account for curvature effects and boundary layer development.

The most famous correlation used to calculate the heat transfer coefficient in a rocket chamber has been proposed by Bartz [15]:

$$h_g = 0.026 \left(\frac{p_c d_{th}^2}{c^* d_h^2}\right)^{0.8} \cdot \left(\frac{\mu c_p}{\lambda}\right)^{0.4} \cdot \left(\frac{d_{th}}{r_{tc}}\right)^{0.1} \cdot \Sigma \tag{2.20}$$

Where d_h is the hydraulic diameter, d_{th} the throat diameter, r_{tc} the radius curvature in the nozzle and Σ a factor that was considered equal to 1 in the first publication of Bartz's correlation in 1957. In a revised version, the factor Σ has been included to account for the influence of the Mach number and the temperature gradient in the boundary layer [16].

$$\Sigma = \left[\frac{1}{2}\frac{T_w}{T_{aw}}\left(1 - \frac{\gamma-1}{2}M^2\right) + \frac{1}{2}\right]^{-0.68} \cdot \left(1 + \frac{\gamma-1}{2}M^2\right)^{-0.12} \tag{2.21}$$

Radiation
In a rocket combustion chamber, the radiative heat transfer phenomenon occurs between the hot gas and the chamber walls. The magnitude of heat transfer depends on the composition of the combustion products, the geometry of the chamber, the wall material, and the temperature of the hot gas.

Several empirical correlations have been derived with the aim of quantifying the radiative heat transfer of combustion products in rocket engines. A model for estimating the radiative heat flux of water and carbon dioxide was proposed by Barrére et al. [17]:

$$\dot{q}_{rad,H_2O} = 4.07 \cdot \left(p_{H_2O}\right)^{0.8} \cdot \left(L_{eff}\right)^{0.6} \cdot \left(\left[\frac{T_{aw}}{100}\right]^3 - \left[\frac{T_w}{100}\right]^3\right) \tag{2.22}$$

$$\dot{q}_{rad,CO_2} = 4.07 \cdot \left(p_{CO_2} \cdot L_{eff}\right)^{0.33} \cdot \left(\left[\frac{T_{aw}}{100}\right]^{3.5} - \left[\frac{T_w}{100}\right]^{3.5}\right) \tag{2.23}$$

Where p_{H_2O} and p_{CO_2} are the partial pressures of water and carbon dioxide, respectively, while L_{eff} is the effective radiation path. Similar correlations are derived by Shack [18], with slightly different coefficients and temperature exponents.

The work of Wang et al. [19] shows that radiative heat transfer is about two orders of magnitude lower than convective heat transfer for LOX/LH2 rocket engines. Although for LOX/Hydrocarbons mixtures the main reaction products are considered strong radiation emitters, the studies performed by Goebel at al. [20] estimated a contribution of 3-5 % of radiative heat flux with respect to total heat loads for oxygen / methane and oxygen / hydrogen propellant configurations. It can therefore be stated that the major contribution to the wall heat flux is given by convective heat transfer.

2.4. Cooling Methods

Due to the high temperatures reached in a rocket chamber during combustion, a cooling system is required to prevent the chamber wall from becoming too hot. If certain temperatures are reached, the wall material decreases its strength and becomes weaker, ultimately bringing the chamber-nozzle system to failure.

This section provides a description of the cooling techniques used in rocketry, with particular focus on the ones employed in the research experiments (capacitive and film cooling). In anticipation of future iterations of the subscale chamber, the regenerative cooling method is also discussed in more detail.

Capacitive Cooling
The capacitive cooling method, also known as the heat sink cooling method, is a passive cooling technique in which the heat transferred to the chamber walls is diffused in the material. High thermal conductivity and large heat capacity of the wall material are essential for the effectiveness of this method, as these properties enable efficient dissipation of the incoming heat at the wall surface, preventing the material from exceeding its temperature limit.

Using this method, the heat transferred into the wall never reaches steady-state condition, and the increase in temperature within the material is described by the following parabolic heat diffusion differential equation.

$$\frac{\partial}{\partial t} = \frac{\lambda}{\rho c_p} \nabla^2 T \tag{2.24}$$

Figure 2.5 presents a typical temperature distribution through a wall of a rocket capacitive chamber as a function of the heating time, highlighting the transient behavior.

The heat sink cooling method is usually applied to subscale versions of rocket engines for preliminary tests, given its simplicity, low cost, and ease to manufacture. The hot-fire tests typically last few seconds, after which the temperature becomes too high for the wall to withstand. The material used for these chambers is usually copper (or a copper alloy), given its good thermal conductivity and heat capacity.

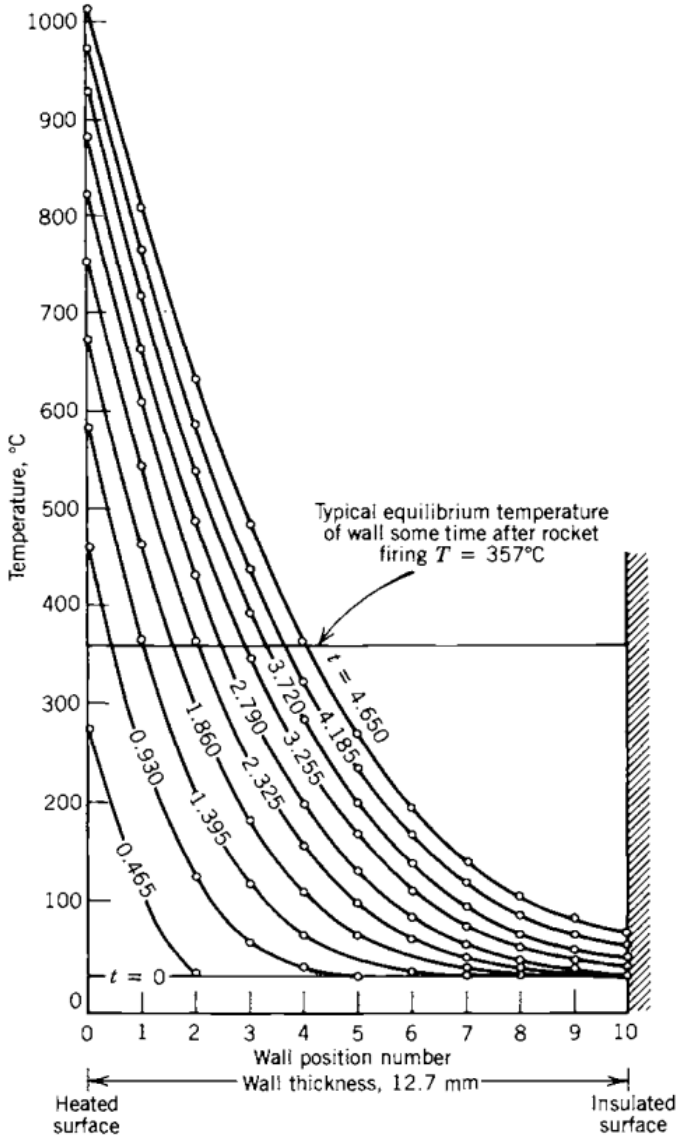

Figure 2.5: Typical temperature distribution within a capacitive chamber wall as function of heating time [5]

Film Cooling

Film cooling involves the injection, close to the chamber wall, of a fluid colder than the hot gases, which decreases the temperature in the boundary layer, therefore reducing the convective heat transfer. The coolant fluid can be the result of propellants burned in fuel-rich mixtures, pure fuel, or turbine exhaust

gases (for example, from a gas generator). The film can be injected in liquid or gaseous form via slots, holes, or outer injectors in the injector head.

The film cooling efficiency Θ, which correlates wall temperatures with and without the presence of the film, is shown in the following equation [21]:

$$\Theta(x) = \frac{T_{w,no\ film} - T_{w,film}}{T_{w,no\ film} - T_{film}} \tag{2.25}$$

In NASA SP-8124 [22], a model for a gaseous film coolant is presented, assuming that turbulence effects cause an entrainment between film and core flow (hot gases), resulting in a decrease in the cooling effectiveness. The entrainment mass flow ratio presents the following relation:

$$\frac{\dot{m}_E}{\dot{m}_{cc}} = \frac{\dot{m}_{tot} - \dot{m}_{cc}}{\dot{m}_{cc}} \left[2 \cdot \frac{\Psi_r \cdot \overline{x}}{r_{c,i} - s_i} - \left(\frac{\Psi_r \cdot \overline{x}}{r_{c,i} - s_i} \right)^2 \right] \tag{2.26}$$

Where $\dot{m}_E$ is the entrainment mass flow, $\dot{m}_{cc}$ the coolant mass flow, $r_{c,i}$ and s_i the chamber radius and the film thickness, respectively, at the injector location. The variable $\overline{x}$ stands for the effective contour distance. Its formula, which employs an empirical fraction multiplier Ψ_m, is as follows:

$$\overline{x} = \int_{x_i}^{x} \frac{r_{c,i}}{r} \cdot \frac{\left(\rho_{core} v_{core}\right)_{2D}}{\left(\rho_{core} v_{core}\right)_{1D}} \cdot \Psi_m \cdot dx \tag{2.27}$$

The last term of Equation 2.26 not yet introduced is the reference entrainment ratio Ψ_r, which is given by an empirical correlation assuming a plain film with constant mass flow and velocity:

$$\Psi_r = \frac{0.1 \cdot \left(\frac{v_{cc}}{v_{core}} \right)}{\left(\frac{\rho_{cc}}{\rho_{core}} \right)^{0.15} \cdot \left(\frac{\rho_{cc} v_{cc} s_i}{\mu_{cc}} \right)^{0.25} \cdot f} \tag{2.28}$$

Where f is a velocity-ratio correlation function.

Figure 2.6 shows a semi-empirical relation provided by NASA SP-8124 [22] between the cooling effectiveness of the film and the entrainment ratio.

Although the presence of film cooling can partially protect the chamber wall from the high temperatures of the hot gas, it introduces losses. The lower temperature of the boundary layer, which is responsible for a decrease in exhaust velocity, coupled with the fact that the coolant flow may not at all, or only to some extent, take part in the combustion process, lead to a decrease in the combustion performance. The present cooling method is generally utilized in small satellite engines or as an auxiliary cooling system complemented by the regenerative cooling method for larger rocket engines.

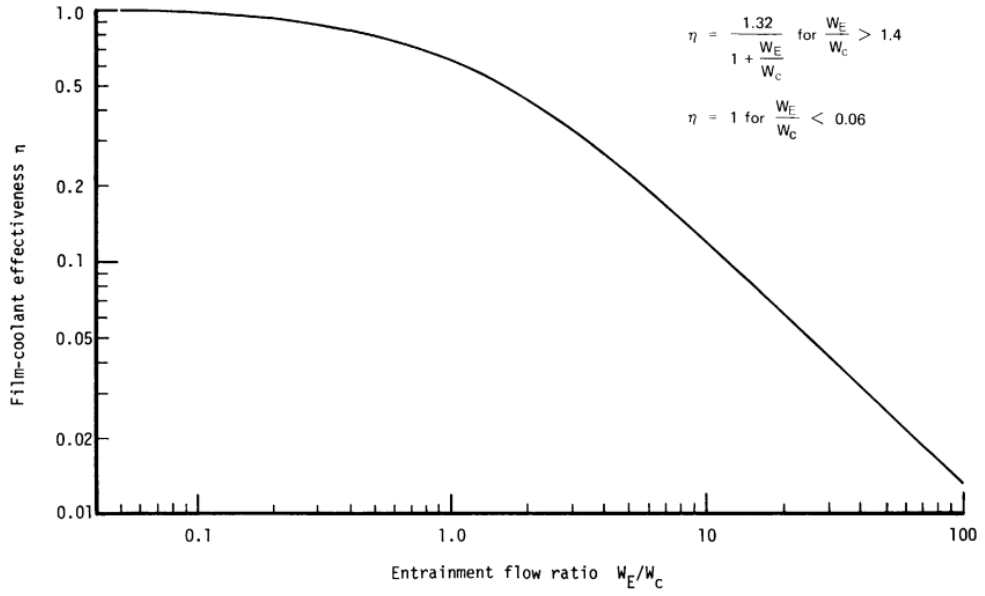

Figure 2.6: Film coolant effectiveness as function of entrainment ratio [22]

Regenerative Cooling

The regenerative cooling system usually employs one or two propellants, which flow inside cooling channels located in the chamber and nozzle walls, to dissipate part of the heat absorbed by the material during combustion. This cooling method, which can be utilized for both transient and steady-state operations, is generally used in high-performance engines operating at great pressures. The functioning principle of a regenerative cooling system is very similar to that of a heat exchanger, since the coolant increases its temperature while flowing in the cooling channel.

For a closed regenerative cooling system, the coolant is injected into the chamber, minimizing the energy loss. Although a higher injector temperature is usually preferred to achieve a great combustion efficiency, it could become unfavorable for the system robustness, when both temperature and pressure are close to critical conditions. Given the sensitivity of the fluid density to the thermodynamic state around this region, the injection velocity can rapidly change, leading to combustion instabilities.

The heat flux from the chamber wall to the coolant can be described using the following equation:

$$\dot{q} = h_{cc} \cdot (T_w - T_{cc}) \tag{2.29}$$

Where h_{cc} is the convective heat transfer coefficient of the coolant, while T_{cc} the temperature of the coolant. Figure 2.7 shows a typical temperature distribution in the radial direction of a regeneratively cooled rocket chamber under steady state conditions.

To calculate the convective heat transfer coefficient h_{cc}, Nusselt number correlations are usually used. An accurate correlation for general pipe flows in turbulent and transition regions has been proposed by Gnielinski [23]:

$$Nu = \frac{(f/8) \cdot (Re - 1000) \cdot Pr}{1 + 12.7 \cdot (f/8)^{1/2} \cdot \left(Pr^{2/3} - 1\right)} \cdot k_x \cdot k_{Pr} \tag{2.30}$$

Where f is the friction factor while k_x and k_{Pr} the correction factors for the start-up and temperature-dependent properties, respectively. Equation 2.29 is valid for $2300 < Re < 106$ and $0.5 < Pr < 500$.

Kraussold [24] also proposed a correlation for the Nusselt number, which has been widely applied for cooling channels in rockets:

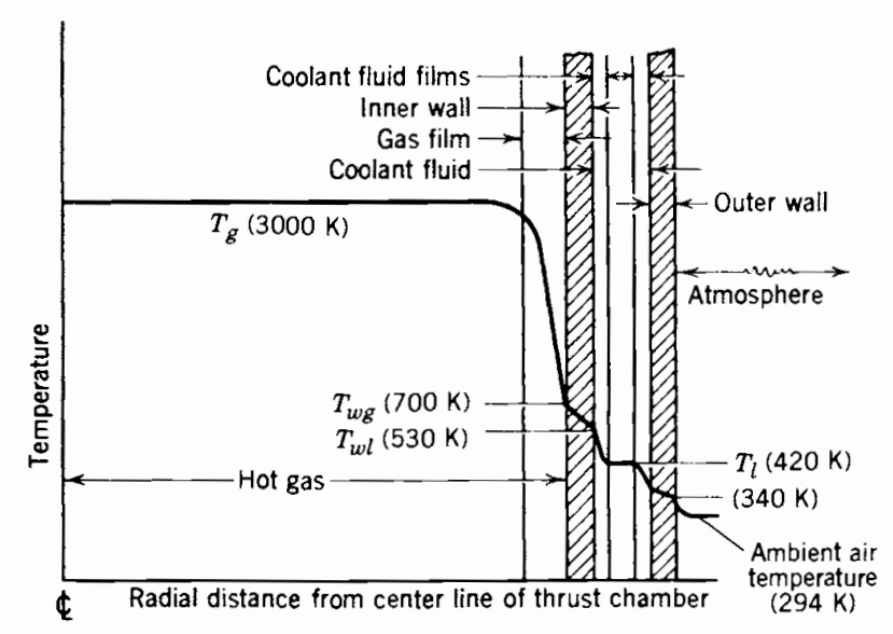

Figure 2.7: Temperature gradients in regeneratively cooled rocket chamber, with typical temperature values [5]

$$Nu = 0.024 \cdot Re^{0.8} \cdot Pr^{0.37} \cdot k_r \cdot k_{cr} \tag{2.31}$$

Where k_{cr} is a correction factor for the curvature of the cooling channel. Other empirical correlations have been derived for hydrocarbons by NASA [25, 26], with a particular focus on methane, propane and ethane.

Given the presence of secondary flows in the cooling channel due to the curvature of the chamber contour and the asymmetric heat transfer, thermal stratification must be considered [27, 28] in the design process. Another parameter that influences heat transfer is the aspect ratio, as it modifies both the flow path and the effective area in the cooling channel for heat exchange [29]. Other effects such as heat deterioration under supercritical conditions [30, 31] and improved heat transfer due to increased wall roughness [32] should also be taken into account.

Other Cooling Methods

Transpiration cooling is similar in principle to film cooling, with the key difference being that the coolant film is injected through a perforated or porous wall rather than through the injector head. By introducing coolant directly into the boundary layer of the hot gas flow, the local thickness of the boundary layer increases. However, excessive coolant injection can lead to boundary layer separation, which enhances heat transfer due to increased vorticity, bringing the hot gases closer to the wall. Although various experimental and numerical studies have explored the complex flow-dynamic phenomena associated with transpiration cooling, this technology has not yet been implemented in flight hardware.

In ablative cooling systems, an ablative material is applied to the chamber wall. During combustion, this material undergoes controlled degradation, which releases gases that help removing heat from the surface. Heat dissipation occurs through the melting, vaporization, and chemical reactions of the ablative material. The resulting gases, which have a relatively lower temperature compared to the primary combustion gases, create a protective film along the wall, further reducing thermal loads by lowering the boundary layer temperature. Ablative cooling has been extensively employed in solid propellant boosters. However, because its efficiency decreases under high chamber pressures and its replacement is costly and impractical, this method is unsuitable for reusable liquid engine designs.

Small engines, such as those employed for orbital control in satellite systems or nozzle extensions of upper-stage propulsion systems, utilize radiative heat transfer as a cooling mechanism. The heat flux radiated from the outer chamber or nozzle wall into the surrounding environment increases with both

the material's emissivity and the wall temperature. Consequently, the amount of heat that can be effectively transmitted using this method is constrained by the thermal and radiative properties of the chamber or nozzle material.

2.5. Heat Transfer Measurements Techniques

Direct measurements of a combustion flame in a rocket combustor are difficult to implement due to its hostile environment, where temperatures reach 3500 K. In laboratory experiments, the use of a transparent window that provides optical access to the chamber can allow the implementation of several measurement techniques. Among the most applied in rocket subscale rocket engines, OH^* and CH^* radical chemiluminescence (with hydrocarbon fuels) has been used as markers of the heat release rate [33] and to study combustion dynamics [34] and instabilities [35], while Coherent Anti-Stokes Raman Spectroscopy (CARS) for temperature measurements [36, 37]. However, these measurement techniques come with several disadvantages: limited access to the chamber due to the window size, the need for an additional cooling system for the window, and high equipment costs.

For these reasons, indirect measurements of the combustion process, such as wall heat flux evaluations, serve as valuable alternatives to study flow and thermodynamic conditions in rocket combustors. This chapter presents the most widely used techniques for heat flux measurements in subscale rocket engines.

Calorimetric Method

For subscale rocket engines using a regenerative cooling system, the heat transferred to the wall from the hot gas can be calculated using the calorimetric method. In particular, if the chamber is in thermal equilibrium (steady-state condition) and the natural convection of the walls to the ambient environment is neglected, the heat transfer rate from the hot gas to the wall is equal to the heat transfer rate from the wall to the coolant. With the calorimetric method, the increase in enthalpy of the coolant, provided by temperature and pressure measurements at inlet and outlet, is used to estimate an average heat flux along the cooling channel, as shown in the following equation:

$$\dot{q} = \frac{\dot{m}_{cc}}{A_w} \cdot \left[H(p,T)_{out} - H(p,T)_{in} \right] \tag{2.32}$$

Where A_w is the surface area of the chamber wall exposed to hot gas and $\dot{m}_{cc}$ is the mass flow of the coolant. Although the global heat flux can be estimated with great confidence, the lack of resolution of the calorimetric method in both the azimuthal and axial directions limits its use. To increase such resolution, a higher number of cooling channel segments should be used, bringing to an increase in system complexity and manufacturing costs. For this reason, when a more detailed resolution is needed, for example to characterize the heat flux profile along the axial direction, other heat transfer measurement methods are usually employed.

Gradient Method

The gradient method, which depends on the placement of two or more thermocouples (generally from 2 to 5) at different radial locations within the chamber material, is one of the simplest techniques used for wall heat flux measurements of subscale rocket chambers. It can be used for actively cooled but also capacitively cooled chambers, allowing heat flux measurements at both steady-state and transient conditions. The concept behind the gradient method is that by estimating the temperature gradient in the normal direction of the chamber wall, the heat flux can be obtained. Equation 2.33 and 2.34 show the formula to compute the heat flux using the assumption of steady-state condition, for a rectangular and cylindrical chamber respectively:

$$\dot{q} = \lambda \cdot \frac{T_{r_2} - T_{r_1}}{r_2 - r_1} \tag{2.33}$$

$$\dot{q} = \lambda \cdot \frac{T_{r_2} - T_{r_1}}{r_c \cdot \ln(r_1/r_2)} \tag{2.34}$$

For regenerative chambers, the gradient method can provide a smaller sensor spacing compared to the calorimetric one, given its simplified sensor placement. In addition, it is possible to have heat flux resolution not only in axial but also in azimuthal direction. Although the calorimetric method is very accurate and requires a low computational cost for capacitive cooling chambers, the approximation implied in Equations 2.33 and 2.34 to calculate the heat flux of the wall can become invalid in the presence of cooling channels. The heat flux relation in fact should follow a more complex expression, given the distortion of the temperature fields caused by the cooling system.

Transient Method

The transient method is used only on combustors with no active cooling. Capacitive chamber configurations, in which the temperature field does not reach a steady state during the test, are usually preferred for the application of this technique.

The concept behind the transient method is to define a control volume around the thermocouple in which the temperature is assumed to be constant. The equation describing the wall heat flux is the following:

$$\dot{q} = \frac{\rho V_{cv} c_p}{A_w} \cdot \frac{dT}{dt} + \dot{d}_{loss} \tag{2.35}$$

Where V_{cv} is the control volume and $\dot{q}_{loss}$ the heat flux that leaves the control volume without contributing to its rise in temperature.

When the temperature gradient is very high inside the control volume, the results from the transient method present high uncertainties, given the assumption of constant temperature variation in time over the whole control volume, as measured by the thermocouple.

Inverse Methods

Inverse methods are among the most advanced techniques for computing wall heat fluxes in rocket engines. Similarly to gradient and transient methods, temperature data is extracted by using thermocouples placed at different locations in the chamber material. The reason why they are called inverse methods is because the cause (heat flux) is calculated from the effect (temperature increase).

The concept of the inverse methods is to iteratively update boundary conditions, which are unknown, to minimize the difference between measured and calculated temperature at each thermocouple location. The residual function J that must be minimized [38] is presented as:

$$J = \frac{1}{M} \cdot [\boldsymbol{T}_{means} - \boldsymbol{T}_{calc}]^T \, [\boldsymbol{T}_{means} - \boldsymbol{T}_{calc}] \tag{2.36}$$

Where M stands for the number of sensor positions. Heat transfer calculations are performed at each iteration step using the Finite Difference Method (FDM), Finite Element Method (FEM), or Finite Volume Method (FVM) and applying the boundary conditions obtained from the previous iteration [7]. The difference between the computed temperature and the measured one from the thermocouple is used to update the boundary conditions until the method converges. Inverse heat transfer techniques can be employed for both transient and steady-state conditions, allowing the calculation of wall heat flux and also coolant heat transfer coefficient, when a regenerative cooling system is present.

3

Literature Study

Building on the theoretical background, this chapter reviews the existing literature related to wall heat flux calculations and the sensitivity of heat transfer to variations in operational parameters within subscale bi-propellant rocket combustors. It begins with an overview of applications of the measurement techniques mentioned earlier used to quantify heat flux, followed by studies that correlate heat transfer behavior with key operating parameters such as chamber pressure, pressure instabilities, film ratio, and mixture ratio.

3.1. Applications of Heat Flux Calculation Methods

This section focuses on how various heat flux measurement methods have been applied in a prior rocket engine test. Each technique offers a distinct balance of complexity, resolution, and compatibility with specific chamber configurations. The literature is examined with particular attention to subscale setups, highlighting approaches best suited for the short-duration tests conducted in this research using a capacitively film-cooled chamber. This review serves to motivate the choice of the heat flux calculation method adopted in the thesis.

3.1.1. Inverse Methods

These techniques estimate unknown heat fluxes by adjusting boundary conditions in a conduction mode until simulated temperatures match those measured by embedded sensors. Inverse methods have become increasingly prominent in rocket propulsion research, offering unmatched spatial and temporal resolution, particularly in configurations with steep heat load profiles.

Schacht et al. [39] laid the groundwork with a 1D analytical formulation for hydrogen–oxygen engines, showing how the axial and circumferential flux distributions could be captured through iterative refinement. Kuhl et al. [40] later extended this concept to a 2D model using a conjugate direction method, allowing simultaneous estimation of both the heat transfer coefficients from the wall and the coolant side in regeneratively cooled configurations.

Suslov et al. [41] validated inverse reconstructions against calorimetric results in a LOx/H_2 chamber. Their study demonstrated that inverse outputs reliably captured heat flux distributions while also resolving film efficiency, a key to understanding wall shielding effects. Celano et al. [42, 43, 44] advanced the technique to 3D with conjugate-gradient implementations, testing both single and multi-element GOx/GCH_4 chambers. These works not only mapped axial flux profiles but also revealed sharp azimuthal discrepancies in heat loading, particularly when misaligned injectors or recirculation zones were present.

Together, these studies underscore the strength of inverse approaches in extracting detailed thermal information from experimental data, which surpasses the capabilities of transient and gradient techniques. Their ability to resolve spatial complexity and capture transient conduction effects makes them well suited for the chamber design and testing conditions employed in this research. For this reason, a previously validated inverse-method solver, RoqFITT [45], was selected for heat flux calculations.

RoqFITT

RoqFITT (Rocket Heat Flux Inverse Thermal Tool), first developed in 2019 by N. Perakis & O. Haidn at the Technical University of Munich [45], is an inverse solver built around a 3D finite-difference conduction model and a Jacobian-based optimization loop, which reconstructs spatial and temporal heat flux profiles from wall-embedded thermocouple data.

In its first application, Perakis et al. [45] used it for heat flux measurements on a capacitively cooled single-injector CH_4/O_2 subscale combustor, equipped with 14 Type-K thermocouples arranged in four azimuthal planes. The reconstructed heat fluxes agreed, within 5%, with results obtained independently with gradient and calorimetric methods. Beyond validating the solver accuracy, they captured localized hot-spot peaks driven by film-hole misalignments and injector-recess vortices.

Shortly thereafter, Strauß [46] applied the same inverse heat flux framework to a water-jacket-cooled, five-injector CH_4/O_2 chamber, operating at 30-50 bar. With 42 thermocouples embedded across five axial cooling segments, he generated 3D wall flux reconstructions that matched calorimetric averages within ±10%, yet revealed intra-injector interaction zones where local flux surged by up to 20%.

In 2021, Preis et al. [47], extended the use of the RoqFITT solver to a full-scale, regeneratively cooled LOx/H_2 upper-stage engine at 100 bar. Here, 28 embedded thermocouples monitored both the hot-gas wall and the water-coolant channels. By coupling the results on both sections, the reconstructed flux profiles of the hot gas and the coolant side were obtained simultaneously, allowing the calibration of the Nusselt correlation multipliers on the fly and reducing the uncertainty of the channel side by roughly 25% compared to standard gradient methods. During 2000 s of testing, the predicted transients stayed within ±7% of the stagnation flux calorimetry.

Finally, F. Longhetti's work [48] pushed RoqFITT into a cold-flow context. He designed and tested an unlike-triplet impinging injector in a purely capacitive copper chamber using ethanol/LOx, and then combined gradient-based heat flux estimates with high-speed imaging to map spray formation. By tuning the jet spacing and the impingement distance, Longhetti reduced the recirculation zones, narrowed the spray plume by approximately 20%, and achieved a more uniform film layer.

Together, these works establish RoqFITT as a validated high resolution tool for the reconstruction of transient heat flux in a wall of capacitive, film and regenerative cooling configurations, and across CH_4/O_2 and H_2/O_2 propellant systems. In addition, they provide a foundation on the literature gap for applying inverse method reconstructions to LOx/Propane rocket chambers, specifically with the coupled capacitive and reactive-film cooling methods in a single-element configuration.

3.1.2. Other Methods

Calorimetric Method

This method, which estimates average wall heat flux by quantifying the enthalpy gain of coolant flowing through the cooling channels under steady-state conditions, has been adopted in subscale rocket combustors equipped with regenerative cooling systems.

Welsh et al. [49] used this technique in a water-cooled NTO/Hydrazine thrust chamber, obtaining results consistent with theoretical predictions from the Bartz correlation [15], which confirmed its precision for heat flux estimation. Based on that, Kirchberger et al. [50] and Schlieben et al. [51] applied the method to LOx/Kerosene chambers with segmented water cooling, allowing them to extract film cooling efficiencies and injector performance. Their use of four cooling segments enabled rough axial resolution while maintaining simplicity in thermal modeling.

Silvestri et al. [52, 53] advanced the approach to a multiinjector GOx / GCH_4 setup, again with segmented water cooling. By resolving average axial flux across five chamber sections, they provided essential validations for numerical tools and illustrated how injector interaction zones influenced thermal distribution. Importantly, these campaigns emphasized the robustness of calorimetry in comparing different injector configurations when precise time-dependent data are not critical.

Despite its strengths, the calorimetric method cannot be applied in the current study because the chamber lacks regenerative cooling and operates in the transient regime. However, it remains a valuable reference for future work on channel sizing in regenerative designs.

Gradient Method
The gradient method uses embedded thermocouples at varying chamber depths to compute local heat flux via radial temperature gradients and Fourier's law, and it has been widely adopted in both actively and passively cooled rocket chambers due to its simplicity and adaptability across geometries.

Celano et al. [42] applied the gradient method to a single-element GOx/GCH_4 heat-sink chamber, embedding thermocouples at fixed radial depths to reconstruct axial heat flux profiles under varying mixture ratios and pressures. Their work highlighted the feasibility of the method in short-duration tests while also revealing limitations in capturing transient dynamics near the throat. Similarly, Conley et al. [54] employed a two-point gradient approach in a LOx/CH_4 capacitive chamber, investigating the influence of chamber pressure and fuel mass flow rate on the wall heat flux. Cirací [55] further explored the gradient method in a rectangular GOx/GCH_4 heat-sink chamber, comparing its outputs with inverse reconstructions. His analysis emphasized the utility of the gradient method for coarse heat flux estimation, but also underscored its limitations in resolving steep gradients and time-dependent effects, particularly in regions of high thermal asymmetry.

Complementing these capacitive applications, Suslov et al. [56] conducted gradient-based measurements in LOx/H_2 regenerative chambers using five radially spaced sensors, allowing resolution of the axial flux distribution. In a follow-up study [57], he compared calorimetric and gradient methods directly, highlighting a roughly four-fold improvement in axial resolution with the latter.

These works collectively highlight the flexibility of the gradient method for both capacitive and regenerative chamber configurations, as well as its limitations in resolution and accuracy for short-duration transient tests with steep thermal gradients. Gradient techniques may offer validation for steady phases of a hot-fire, but they might not be sufficient to capture the spatial and temporal dynamics characteristic of the short-duration tests conducted in this research.

Transient Method
The transient method estimates heat flux by tracking how the wall temperature changes over time, and has mostly been used in heat-sink (capacitive) chambers during short hot-fire tests where the wall does not reach thermal equilibrium.

Locke et al. [58] implemented a discretized transient approach with multiple nodes in a LOx / GCH_4 subscale combustor, to evaluate the heat flux of the wall under varying chamber pressure and mixture ratios. Their results highlighted the method's ability to track temporal changes, but also noted growing uncertainty at sharp thermal gradients (such as near the throat). Droppers et al. [59] followed a similar path with oxygen/hydrogen subscale hardware using coaxial temperature sensors. Their focus was on the dynamic interaction between combustion instabilities and wall heating. Although the transient method captured general trends, its simplified modeling became a source of error where localized phenomena dominated.

Celano et al. [42] applied a zero-dimensional transient model in a GOx/GCH_4 single-element chamber of rectangular shape, founding higher peak heat fluxes than those derived by gradient or inverse techniques, possibly due to unmodeled spatial non-uniformities and film effects.

Although the transient method is compatible with short-duration capacitive testing, its simplified assumptions introduce significant uncertainty near areas of steep gradients and local asymmetries, such as critical sections such as the chamber throat. For these reasons, it is not pursued further.

3.2. Studies of Heat Flux versus Operating Parameters

To complement the review of the applications of heat flux measurement methods and tie into the present work, this section examines how key operating parameters have been correlated with wall heat flux in prior rocket engine studies. Rather than relying on purely empirical fits, sensitivity analyses on the available literature is instead emphasized, to qualitatively relate the heat flux response to changes in chamber pressure, pressure instabilities, film ratio and mixture ratio.

Chamber Pressure
The relationship between wall heat flux and chamber pressure has been extensively explored in many rocket engine studies. Early works established a clear positive correlation, often quantified through

empirical models such as Bartz's correlation [15], introduced in Equation 2.20, which predicts the scaling of the convective heat transfer coefficient as $h_g \propto p_c^{0.8}$. This formulation suggests that even modest increases in chamber pressure yield significant rises in wall heat flux, making pressure one of the most influential operating parameters in thermal analysis.

Building on this foundation, Schacht et al. [39] and Sinyarev et al. [60] reported similar power law dependencies in hydrogen-oxygen single-element chambers, refining the exponent to approximately 0.82. These findings reinforced the generality of the chamber pressure / heat flux relationship across combustion chemistries and injector designs. Silvestri et al. [52] investigated a multi-injector GOx/GCH_4 combustor, correlating throat heat flux with chamber pressure over a 20–40 bar range. Their results demonstrated a consistent exponent of 0.80 ± 0.05, even within radial non-uniformities caused by inter-injector flow interactions. Statistical regression in their work further confirmed pressure as the single strongest predictor of heat flux trends.

Locke et al. [58] conducted a detailed sensitivity study using gradient and transient methods in a LOx/CH_4 subscale chamber. They found that the wall heat flux varied proportionally with chamber pressure with the relation $h_g \propto p_c^{0.78\pm0.03}$, attributed to boundary layer thickening effects from film cooling, which introduce nonlinearities in convective transfer.

As a result of these studies, the chamber pressure exhibits a consistent and strong positive correlation with the wall heat flux. Empirical models and experimental data suggest a scaling exponent of ~0.8, applicable across fuels and geometries. Even in film-cooled setups, pressure remains the dominant thermal driver, although its influence may be moderated by boundary-layer effects.

Combustion Instabilities

Combustion instabilities play an important role in transient heat-flux behavior, as shown by the foundational work of Harrje et al. [61], compiled in NASA SP-194, who first quantified these effects. They observed that pressure fluctuations within liquid-propellant chambers could drive heat flux spikes up to 25%, depending on the instability amplitude and modal structure. These fluctuations influence both core gas dynamics and boundary layer stability, compounding thermal sensitivity. Ueta et al. [62] examined flame–acoustic coupling in a model hydrogen combustor, demonstrating how pressure oscillations modulate boundary layer thickness at 300–800 Hz. Their use of chemiluminescence imaging revealed that heat flux peaks were phase-locked to pressure cycles, emphasizing the repeatable nature of instability-induced loading.

Arnold [21], in high-pressure LOx/H_2 tests, documented local heat-flux surges exceeding 50% above nominal values during unstable operation. These events were attributed to periodic film peeling by vortice structures, which momentarily exposed the copper wall to hot core gases. Zandbergen et al. [63] further explored thermoacoustic coupling in a hybrid-cooled LOx/H_2 chamber. Even with film and regenerative cooling, they found that instabilities raised time-averaged heat flux by ~10%, with transient spikes reaching 30% above baseline.

Together, these studies show that oscillatory pressure modes, particularly at high frequencies, introduce transient and localized increases in the wall heat flux. Combustion instabilities can alter the chamber's internal flow field, modulate the thickness of the boundary layer, and move the position of the flame near the wall, affecting the convective heat transfer and resulting in localized thermal load peaks.

Film Cooling Ratio

Film cooling plays an important role in modulating wall heat flux by creating a thermally protective layer between the core combustion gases and the chamber wall. The effectiveness of this method depends not only on the physical properties of the coolant but also on its relative mass flow rate compared to that of the core flow.

Zandbergen et al. [63], though focused on instability coupling in LOx/H_2 chambers, incorporated film effects into their models. They confirmed a baseline reduction of ~20% in steady-state heat flux due to film cooling, but found that this shield was still vulnerable to transient pressure waves, reinforcing the importance of both ratio and flow stability.

Arnold et al. [64] carried out systematic experiments in LOx/H_2 showerhead-injected chambers to quantify heat flux reductions in different film ratios ranging from 0.0 to 0.10. Their data revealed a non-

linear trend, with optimal cooling occurring at intermediate ratios, resulting in up to 30% reduction in wall heat flux. At higher ratios, the film entrainment in the core flow degraded the cooling performance and reversed the benefit. Silvestri et al. [52] studied multi-injector GOx/GCH_4 configurations and compared throat heat flux across three curtain ratios (0.02, 0.04, 0.06). Their calorimetric data supported Arnold's findings, showing that low film ratios yielded modest protection, mid-range ratios optimized shielding, and high ratios reduced performance due to flow mixing.

In a further effort, Suslov et al. [41] showed film-induced asymmetries of up to 25%, by rotating a LOx/GH_2 chamber injector plate, to resolve azimuthal flux variations. These effects were directly related to the arrangement and orientation of the curtain holes. Their inverse and gradient reconstructions proved that even at fixed film ratios, directional flow structures significantly influenced local thermal behavior.

These investigations demonstrate that the effectiveness of film cooling is strongly dependent on the mass flow ratio between curtain and core streams. In addition, intermediate ratios seem to deliver maximum thermal protection, while higher ratios lead to entrainment and reduced shielding. Asymmetries in hole geometry and flow alignment further complicate local heat flux behavior, making film ratio and geometry a crucial control parameter for thermal management.

Mixture Ratio

The oxidizer-to-fuel ($^O/_F$) mixture ratio affects both the temperature and composition of combustion products, with direct implications for wall heat transfer, especially in chamber configurations without protective film. Sutton & Biblarz [5] note that peak flame temperatures typically occur on the fuel-rich side of stoichiometry, which for LOx/C_3H_8 is around $^O/_F \approx 2.9$. This implies that even modest shifts in the mixture ratio can change the adiabatic wall temperature and alter the convective gradient.

Locke et al. [58] investigated LOx/GCH_4 combustors across a range of $^O/_F$ values (2.5 to 3.5) and observed wall heat flux variations under 8%. Their findings suggested that film cooling creates a buffer zone between core combustion and wall heating, effectively decoupling mixture effects from direct thermal response. Silvestri et al. [52], operating multi-injector GOx/GCH_4 chambers, reported heat flux changes below 10% across $^O/_F$ values from 2.8 to 3.4. Chamber pressure and film loading emerged as the primary flux drivers, while mixture ratio remained a secondary factor. Similar conclusions were drawn by Zandbergen et al. [63] in hybrid-cooled LOx/H_2 chambers: even a 10% swing in $^O/_F$ altered the average wall flux by less than 5%, confirming a buffered response.

From these findings, the mixture ratio influences flame characteristics and theoretical wall temperatures, but its direct impact on heat flux is often masked by film shielding or other dominant effects. Variations in core $^O/_F$ ratio yield relatively modest changes in wall thermal loading, suggesting that, in film-cooled systems, the mixture ratio plays a secondary role compared to chamber pressure, combustion instabilities and film characteristics.

4

Experimental Set-Up

This chapter presents the infrastructure and hardware used for the experimental tests. The hardware employed is a subscale rocket combustor equipped with a hybrid capacitive and reactive-film cooling system, with thermocouples embedded within the chamber material to allow for accurate heat flux measurements.

Two test campaigns were conducted, each with distinct objectives. The first aimed to screen various core injector geometries to identify a stable and efficient configuration. The second focused on evaluating the selected injector under a range of operating conditions to more broadly assess its stability and performance.

After introducing the test facility fluid system, the subscale combustor assembly is discussed in detail, together with the instrumentation used. Finally, the pre-test procedures and the hot-fire sequence are briefly presented.

4.1. Test-rig Fluid System

The Plumbing and Instrumentation Diagram (P&ID) of the test-rig fluid system is shown in Figure 4.1. The fluid plan uses color-coding to distinguish the fluid paths: propane is marked in red, oxygen in blue, and gaseous nitrogen in green. On the left side, the diagram shows the interfaces with the supply tanks and GN_2, while on the right side, the interface to the test article (subscale chamber). Starting from the supply tanks, each propellant feed-line is split into two branches, one feeding the core manifold and the other the curtain manifold, to allow independent mass flow control of each side.

All four feed-lines share a similar layout, consisting of the following components:

- Pressure regulator (PR): sets the target line pressure
- Thermocouple and pressure sensor (T, P): monitor flow temperature and pressure
- Critical flow Venturi nozzle (CFV): used to characterize mass flow rate
- Run valve (RV): controls propellant delivery to the test article
- Safety valve (SV): provides overpressure protection
- Check valve (CV): prevents backflow in the line

The major difference between fuel and oxidizer feed-lines lies in the post-test handling of the remaining propellants in the run-lines. While oxygen is simply vented into ambient after the hot-fire, propane requires to be disposed differently: it is routed through a dedicated drain line to a burn pit, where it is safely combusted.

At last, gaseous nitrogen (GN_2) is used for multiple roles: it purges the lines before and after testing, pilots the pressure regulators, and powers the pneumatic actuators for the run valves.

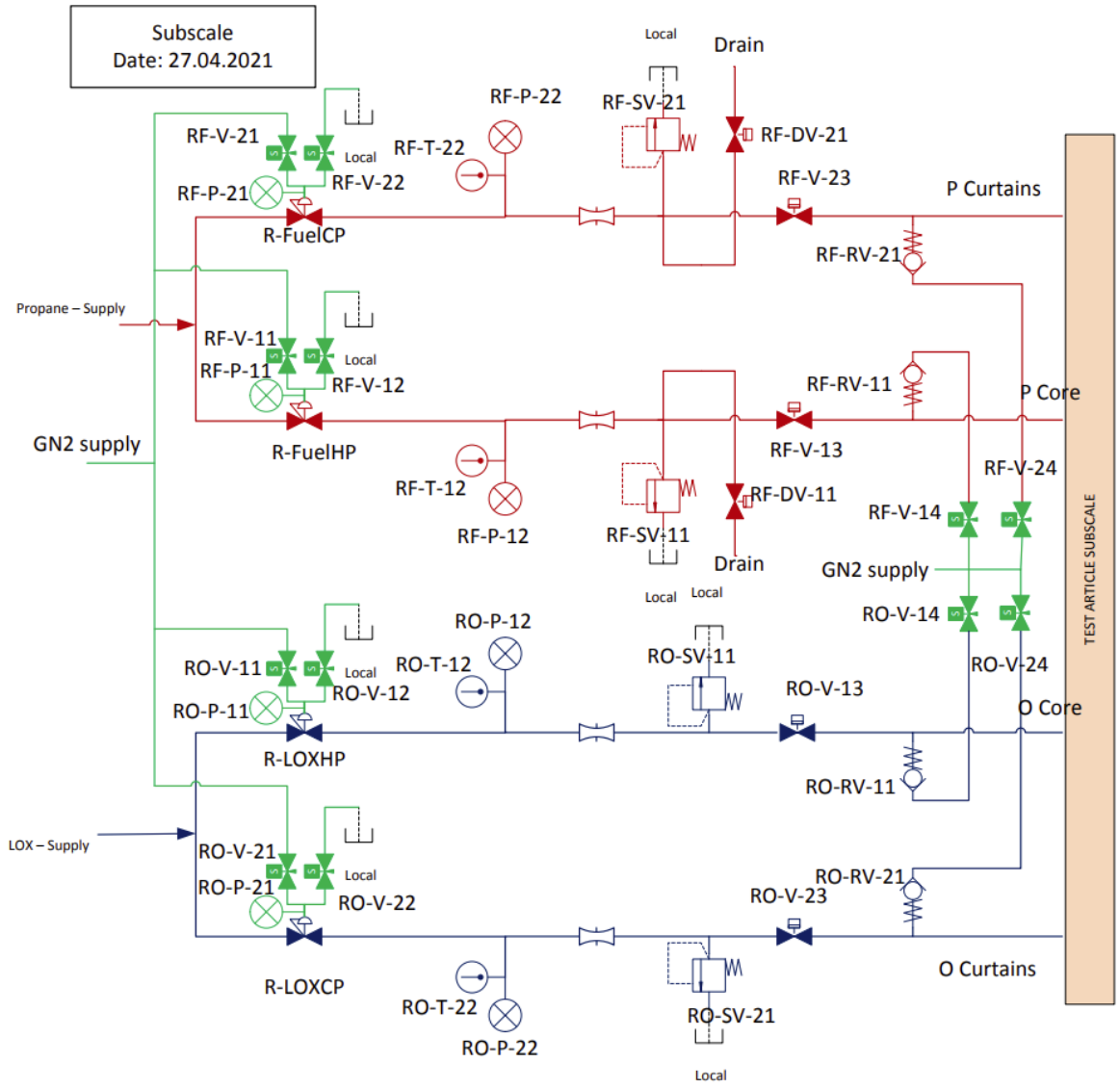

Figure 4.1: P&ID of the subscale fluid-plan (provided by Isar Aerospace SE)

Critical-Flow Venturi Nozzle

For fluids at high pressure and cryogenic temperature, measuring (and setting) the correct mass flow rates is quite a challenge. Coriolis-based mass flow meters are commonly employed due to their high precision; however, since their correct measurement is obtained with a delay of several seconds, they are not suited for measuring mass flows in short-duration tests. For this reason, Critical-flow Venturi nozzles have been employed instead.

The working principle of a CFV is based on reaching choked flow conditions at the Venturi throat, where the fluid velocity becomes sonic. This occurs when the upstream-to-downstream pressure ratio exceeds the critical pressure ratio: once choked, the flow rate becomes independent of the downstream conditions, enabling the use of only upstream temperature and pressure to compute the mass flow.

This principle was successfully applied to both propellants used:

- Oxygen, which enters the chamber in a supercritical state, behaves like a dense real gas. It supports choked flow conditions, and it requires empirical correction factors to account for real-gas behavior for the mass flow calculation
- Propane, on the other hand, is injected as a sub-cooled liquid. Under expansion through the

Venturi, it may partially flash or cavitate, but choking can still occur, and mass flow becomes downstream-independent as well.

The equation used for the mass flow calculation is the following:

$$\dot{m} = A_{th} \cdot p_0 \cdot \sqrt{\frac{M}{R_u T_0}} C^* \tag{4.1}$$

Where A_{th} is the Venturi throat area, M the molar mass of the fluid, R_u the universal gas constant, p_0 and T_0 the stagnation pressure and temperature, respectively, while C^* the critical flow function, which accounts for real gas effects and is empirically determined.

Before the start of the test campaigns, the CFV have been calibrated using Khrone Coriolis mass flow meters during cold long-run tests, allowing to create a fitted curve. During the test campaigns, CFVs with various throat diameters were swapped in as needed, depending on the required flow rate and inlet pressure at each load point.

4.2. Subscale Chamber

The subscale chamber was designed as a modular single-element assembly, able to interchange both injector elements and chamber sections when needed. The cooling system used is a combination of active (film) and passive (capacitive) cooling methods, which allowed only short-duration tests. Film cooling is obtained using a reactive propellant curtain at low oxidizer-to-fuel ratio, while capacitive cooling is achieved with the thick copper wall of the chamber, which acts as a heat-sink due to its high thermal conductivity.

The selected configuration offers several safety advantages during the initial development of a rocket chamber, allowing for a more prudent step towards the following regeneratively cooled design. In fact, starting with a capacitive chamber allows early tests to be conducted even under potential chamber instability, with a lower chance of incurring catastrophic failures.

4.2.1. Chamber Assembly

The combustor assembly, shown in Figure 4.2, consists of:

- A stainless-steel injection manifold with four inlets (core and curtain for both LOx and Propane)
- A single-element injector plate, housing the core injector and 2 outer rings of curtain film holes
- Four main copper segments (igniter ring, 2x cylindrical section and a nozzle segment
- A torch igniter, mounted to the igniter ring, which provides ignition using GOX-GCH4 as propellant mixture
- Steel tie rods for axial compression and graphite seals for leak-tightness between segments
- Ports for instrumentation (thermocouples and pressure sensors)

This modular setup allows controlled interchangeability between configurations and parts, ensuring both test repeatability and adaptability.

During the first test campaign, two chamber geometries were used, differentiating only by the size of the throat diameter. The first, used in the early stages of the injector selection, is Mach scaled, keeping the dynamic similarity with respect to the full-scale design over the Mach number distribution. The second is instead Pressure scaled, with a reduced throat diameter to achieve higher chamber pressures.

The reason behind choosing these two scaling methods is that while the Mach-scale configuration serves as an initial tool for studying the flow structure and combustion anchoring, the Pressure-scaled one is used to better match the higher full-scale chamber pressure and thermal loads. The transition between the two configurations was carried out conservatively, on the basis of observed chamber pressure levels, instability trends, and wall heat fluxes recorded during Mach-scaled tests.

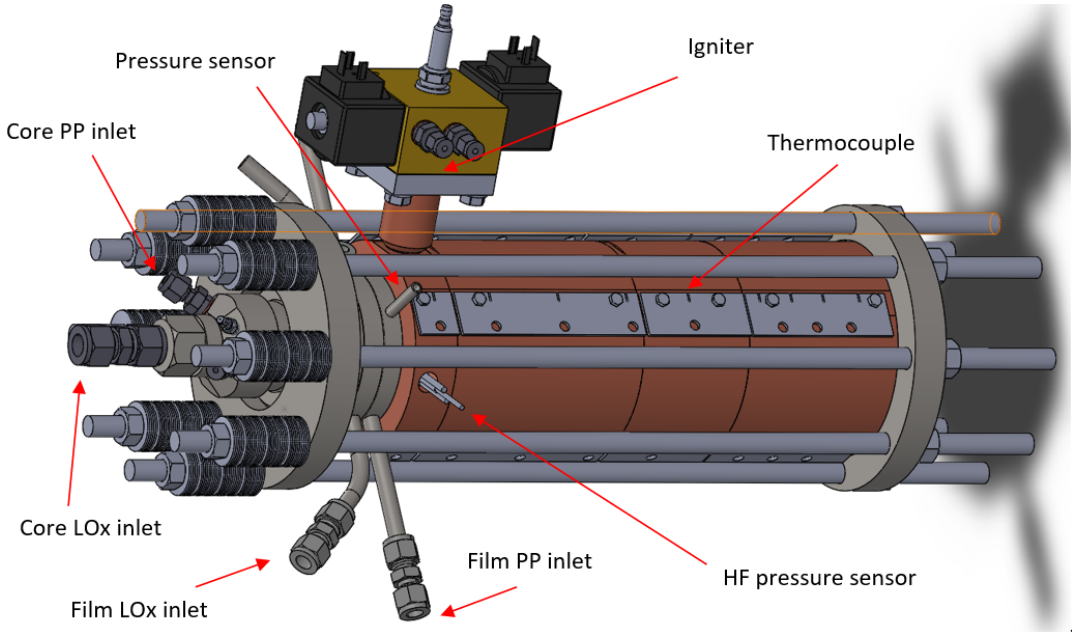

Figure 4.2: CAD view of subscale combustor (provided by Isar Aerospace SE)

4.2.2. Injector hardware

The injector plate used in the subscale combustor, shown in Figure 4.3, features a central core injector surrounded by two rings of showerhead holes, which have the function of creating a protective film close to the chamber wall.

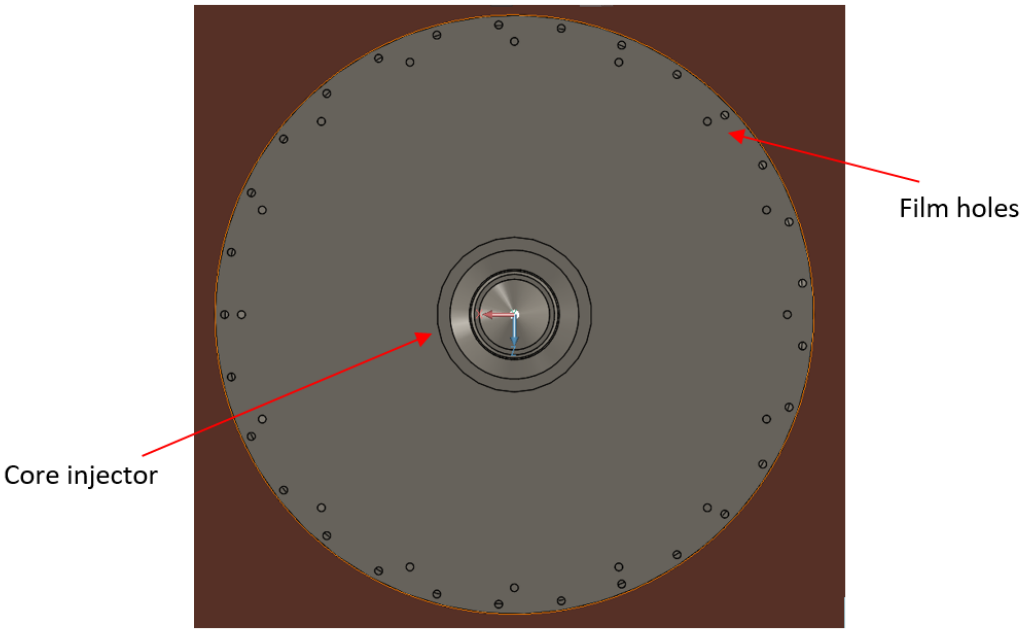

Figure 4.3: Injector plate with core injector and curtain holes (provided by Isar Aerospace SE)

Film Configuration

The curtain injection configuration, chosen to be reactive, consists of injecting propane from the outer ring and oxygen from the inner ring. Given the high reactivity of oxygen with metals, this combination ensures a better protection of the chamber wall from oxidation. The showerhead arrangement, which

intentionally promotes limited propellant mixing, is designed to maintain the film under fuel-rich conditions. Due to the different number and placement of propane and oxygen holes, the radial arrangement of the curtain is inherently non-uniform and this geometric asymmetry is expected to influence local heat flow behavior.

The design choice of using a reactive curtain film went through a careful trade-off between combustion efficiency and cooling effectiveness. Although nonreactive films (using only one propellant, typically the fuel) offer superior thermal protection, they also lower the overall combustion performance because of incomplete propellant participation in the combustion process. The chosen strategy of injecting both oxidizer and fuel into the curtain film was aimed at providing a balance between effective wall shielding and acceptable efficiency.

Core Element

At the center of the injector plate lies the core injector, a coaxial semi-swirler, which operates under close-to-stochiometric conditions. Its working principle, shown in Figure 4.4, consists in:

- Oxidizer injection via small tangential annuluses that impart swirl into an inner oxidizer post
- Fuel injection through concentric annuluses without swirl, delivering flow into an annular sleeve surrounding the oxidizer jet

This geometry provides a shear-driven mixing between the two streams, with the swirl component used to enhance recirculation and for flame anchoring. A recess in the oxidizer post is applied to the injector(s) used, as it has been shown to improve the mixing performance [65].

During the first test campaign, several coaxial semi-swirler injectors with different geometric features were tested, such as recess depth, inlet annulus dimensions, and exit chamfer angle. This allowed elements to be tested with variated flow characteristics, such as injection velocity, propellant entrainment ratio, and the resulting spray cone.

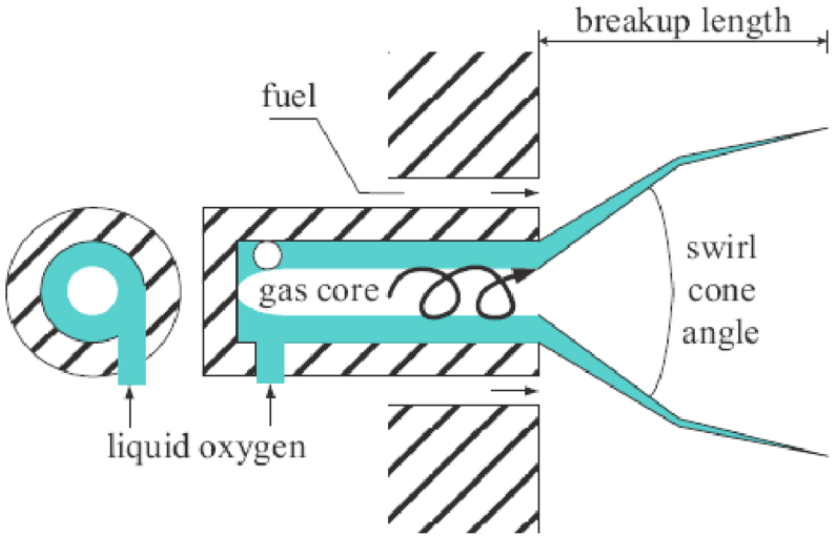

Figure 4.4: Schematic section of a general coaxial semi-swirler injector [66]

4.2.3. Instrumentation

To perform a high-resolution thermal analysis of the tests, the subscale chamber was instrumented with 42 thermocouples (Electronic Sensor Type K, Class I, with 0.5 mm tip and accuracy of $\pm 1.5K$) embedded within the copper wall. These sensors were not exposed directly to the combustion gases, because they would have rapidly failed, given the extreme temperatures reached inside the chamber. They have been instead placed inside pre-drilled cavities, with the sensor tip (or pearl) seated at the bottom of the hole (typically distant 1.5 mm from the inner wall surface), kept in place by a spring applying 4 N. In

this way, an accurate temperature reading was possible while the sensor's survivability and correct placement were ensured even during vibrations.

To capture potential azimuthal asymmetries in the combustion process, the thermocouples were distributed in four azimuthal planes, 90° apart. Each azimuthal location was instrumented with sensors placed along the axial direction, from the igniter section to the throat restriction. Two of the azimuths (1 & 5) were configured with a higher resolution layout (14 sensors each, as shown in Figure 4.5), while the remaining two (3 & 7) with a lower one (7 sensors each, as shown in Figure 4.6).

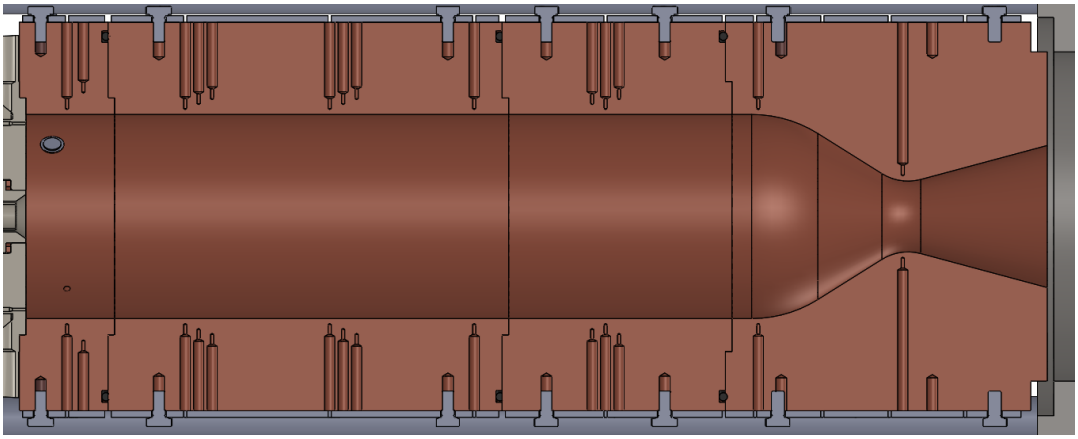

Figure 4.5: Section view the subscale chamber used in the test campaigns, for azimuthal locations 1 & 5 (provided by Isar Aerospace SE)

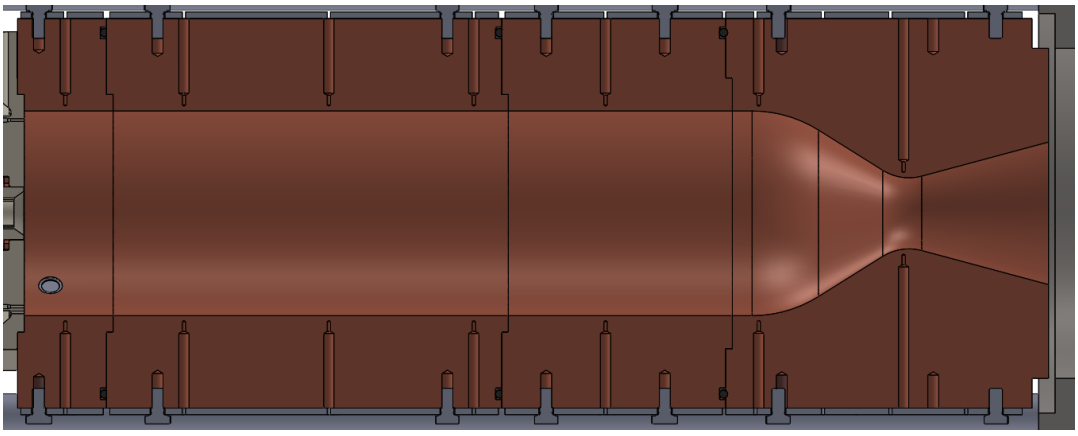

Figure 4.6: Section view of the Pressure-scaled subscale chamber used in the test campaigns, for azimuthal locations 3 & 7 (provided by Isar Aerospace SE)

The azimuthal numbering follows a clockwise convention starting from the igniter position, as shown in Figure 4.7: Azimuth 1 is located 45° clockwise from the igniter port, followed by Azimuths 3, 5, and 7 in sequence.

In addition to the thermocouples embedded into the chamber material, the subscale assembly was instrumented with pressure sensors (and extra thermocouples) to monitor both injection and chamber conditions:

- 4x Wika S-20 pressure sensor (0-160 bar, with accuracy of ±0.25% of span) in the injector head to monitor core and curtain injection pressure of both propellants (one each manifold)
- 1x Wika S-20 pressure sensor (0-160 bar, with accuracy of ±0.25% of span) in the chamber to record mean combustion pressure at low-frequency sampling rates

- 1x Kistler water-cooled pressure sensor in the chamber for high-frequency measurements to better characterize combustion instabilities (not used for the analysis carried out in this research)
- 4x Electronic Sensor thermocouples, Type T, Class I, with 1.5 mm tip, to monitor the propellant injection temperature in injector manifold.

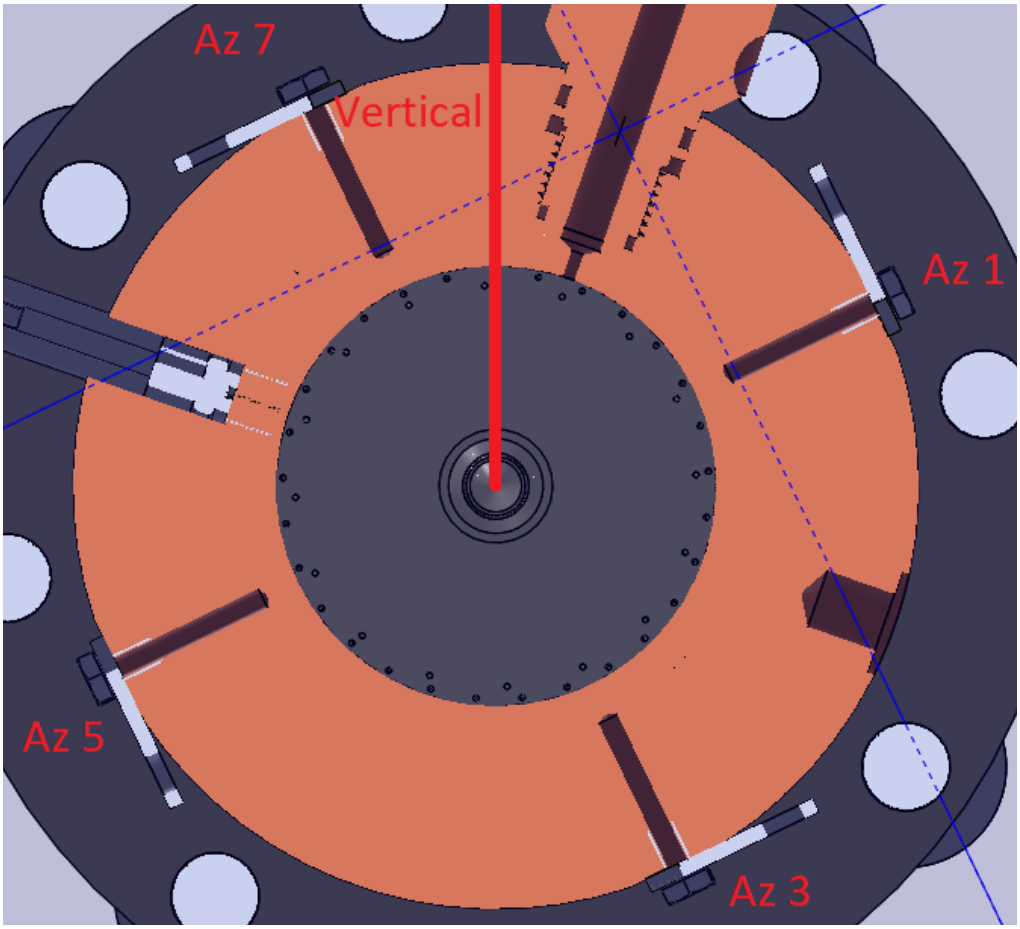

Figure 4.7: Radial section view of the subscale chamber at igniter location (provided by Isar Aerospace SE)

4.3. Testing Operations

This chapter defines the operations involved in preparing and executing the hot-fire tests, from the initial setup and safety checks to the actual hot-fire sequence.

4.3.1. Hot-fire Preparations

All mechanical parts, including the chamber components, feed-lines, valves and interfaces, were carefully assembled, with particular attention to cleanliness, especially in regions exposed to liquid oxygen. Any residual contaminants, such as dust or grease, could result in orifice blockage, leaking valve or unwanted reaction (when in contact with pure oxygen).

After mechanical integration, the cryogenic feed-lines were thermally insulated and all sensors and actuators were connected. Input/output (I/O) checks were then performed to ensure that each component was working and assigned correctly to the control system. This step is critical to ensure full control over the system and to avoid command errors such as valve cross-actuations.

Pre-Test System Checks and Validation

A series of checks and validation procedures were conducted prior to the hot-fire sequence, listed as follows:

- CFV Characterization: Critical flow Venturi nozzles were pre-calibrated using Coriolis mass flowmeters during long-run cold-flow tests. This allowed selection of appropriate CFVs for the target load point
- Pressure Checks: By locking the nozzle exit with a blind flange, the subscale chamber was pressurized, to verify that weak points such as pressure sensor ports or inter-segment interfaces were leakage-tight at least in static pressure conditions
- Cold Flows: Liquid nitrogen was used to simulate cryogenic conditions in the propellant lines and to assess pressure drops on both facility and test article. These tests helped to predict the chilling time of each line and to evaluate whether the insulation was effective enough
- Standalone Ignition: Prior introducing LOx and Propane into the chamber, the igniter functionality was checked along with ignition temperature and (possible) ignition delays
- Curtain-Only Hot Fire: A partial hot-fire test was also conducted, flowing propellants only through the curtain holes, with GN_2 through the core side to preserve internal flow dynamics. This intermediate step was used in the early stage of the first test campaign to confirm a proper film ignition and to allow for a safe progression towards the core + curtain (full) hot-fire.

Propellant Loading and Conditioning
On test day, propellants were transferred from storage tanks (large in volume, rated for low pressure) to run tanks (small in volume, rated for high pressure). Each fluid followed a distinct path:

- Oxygen was flown to the run tank in cryogenic condition and allowed to boil there, enabling self-pressurization. Tank pressure was regulated via periodic venting and refilling
- Propane, supplied at ambient conditions, was cooled by injecting liquid nitrogen inside the run tank. Through LN2 boiling and mixing, the propane was then slowly reaching the target cryogenic temperature.

Before reaching the hot-fire sequence, the test article and feed-lines were thermally conditioned, ensuring that the propellant temperature remained constant as much as possible throughout the run. This step was crucial to maintain injection repeatability, as fluid properties, such as density and viscosity, directly affect mixture ratio, atomization behavior, and combustion dynamics.

4.3.2. Hot-fire Sequence

The hot-fire sequence, described in more detail in Appendix A, can be summarized in the following four main stages:

1. Pre-Ignition:
   - Feed-line chill-down using cryogenic propellants or LN_2
   - Run tank pressurization ramp-up to desired injection pressure
2. Ignition:
   - Curtain ignition: LOx and Propane are introduced in the outer rings to establish the protective film and initiate the combustion
   - Core ignition: Once the film is stable, the core propellants are injected and ignited
3. Hot Fire:
   - Steady-state combustion, typically for 0.5-1 s. This ensured safe operation under capacitive cooling constraints, while still capturing thermal transients
4. Shutdown:
   - Fuel-rich shutdown procedure: LOx was shut off before propane, to avoid crossing the stochiometric ratio.
   - Post-burn GN_2 purging of fuel and oxidizer lines.
   - Run tank depressurization, safe venting and draining of any propellant residuals.

5

Methodology

With the experimental setup defined, this chapter introduces the analytical framework used to compute and analyze the heat flux data. After providing a workflow overview of the methodology applied, the RoqFITT inverse solver is presented along with the relative inverse method used to reconstruct the heat flux. The chapter then details how test phases were chronologically segmented, how signal alignment was performed, and which variables were chosen for the sensitive study. Finally, the visual and statistical tools used to analyze the data are discussed, along with an error analysis on the heat flux results.

5.1. Workflow Overview

Given the number of steps required to compute and analyze the wall heat flux, this chapter is used to provide clarity to the methodology followed in the research project. The different operations performed are grouped and presented chronologically with a simple, yet effective, flowchart, shown in Figure 5.1.

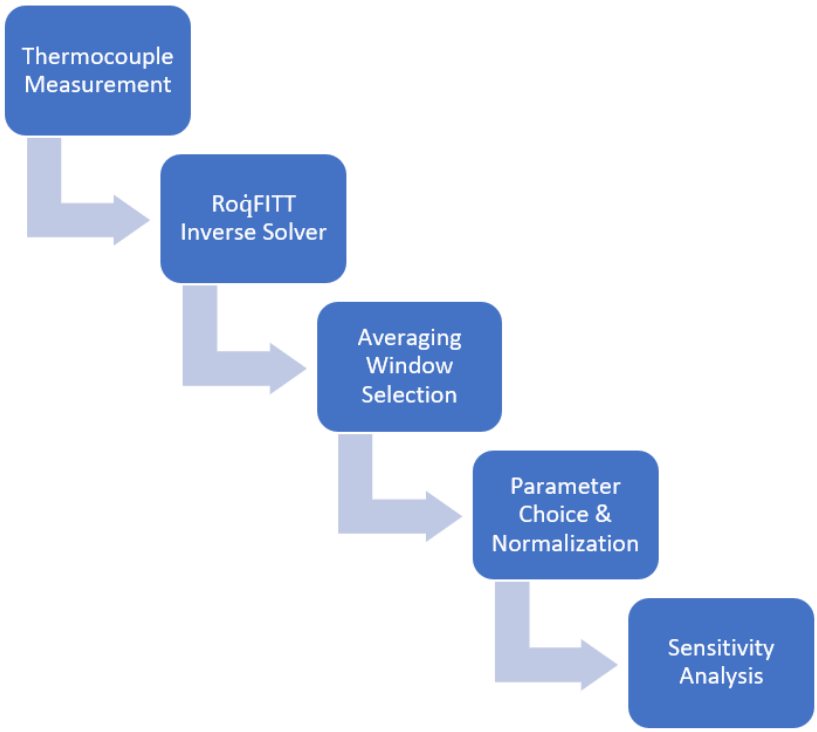

Figure 5.1: Methodology workflow overview

5.2. RoqFITT Inverse Solver

Inverse methods have been widely used to solve heat transfer problems in rocket applications, where direct measurement of the surface temperature is not feasible due to extreme operating conditions. Rather than trying to model the complex chemistry and turbulent phenomena that occur inside the chamber, these techniques allow the heat flux to be calculated indirectly, treating the combustion process as a 'black box' and relying solely on temperature readings.

In this work, the inverse solver RoqFITT was used to reconstruct the transient surface heat flux distribution. Developed at TUM by N. Perakis et al., the code resolves the inverse heat conduction problem for capacitive chambers of cylindrical and rectangular geometry [45, 67]. Later improved by J. Strauß with the possibility of computing the heat flux also in regenerative chambers [46], the solver implements a Jacobian-based optimization algorithm coupled with a finite-volume solver, iteratively adjusting the heat flux boundary condition to minimize the difference between measured and computed temperatures.

The main steps of the algorithm are shown with a flow chart in Figure 5.2, for better clarity.

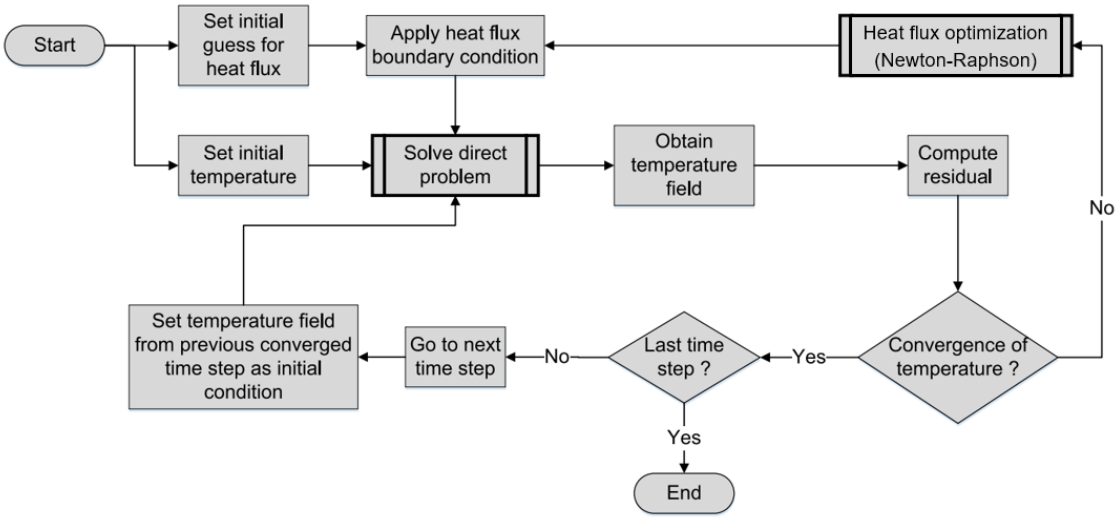

Figure 5.2: RoqFITT iterative algorithm [45]

The process begins with an initial guess for the surface heat flux, which is used to solve the direct heat conduction problem by applying the defined boundary conditions and the initial temperature field. The resulting temperature distribution is then compared with the experimental data recorded by the thermocouples, and a residual is calculated. If this residual falls below a defined threshold, the iteration is considered converged, and the solution advances to the next time step, using the current temperature field as the new initial condition. If convergence is not achieved, the surface heat flux is updated through a Newton-Raphson optimization method until the temperature residual is below a defined value.

The RoqFITT solver, written in Python, was configured to process the specific copper chamber configuration of the subscale test hardware.

5.2.1. Computational Domain and Boundary Conditions

The computational domain for the subscale rocket combustor was constructed in ICEM CFD, using the CAD model of the relevant chamber configuration as a reference. Due to the geometric simplicity and azimuthal symmetry of the system, a two-dimensional contour was selected to represent the domain. Once the contour was finalized, the surface zones were labeled to uniquely define each physical boundary of the model.

An unstructured mesh was generated to discretize the domain, offering flexibility in local refinement and better conformity to the curved geometry. Particular attention was paid to the inner wall adjacent to

the combustion region, where steep thermal gradients were expected. In this area, the mesh density was significantly increased to capture rapid spatial variations in temperature and ensure accurate resolution of the conductive heat flux. A representative view of the meshed geometry and the labeled boundaries is shown in Figure 5.3.

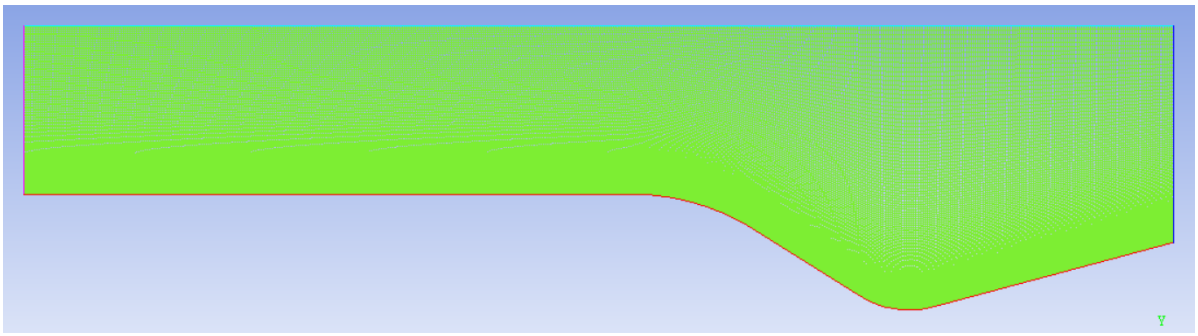

Figure 5.3: Chamber geometry contour with unstructured mesh generated in ICEM CFD

Following mesh generation, ANSYS Fluent [68] was used to define the thermal test case by applying the energy equation across the solid copper domain. The material properties were treated as temperature dependent, reflecting the non-constant behavior of copper under elevated heat loads.

Each surface boundary was assigned with physically appropriate thermal conditions, as shown by the different colors visible Figure 5.3:

- Light blue (ambient side): natural convection
- Dark blue (nozzle side): adiabatic
- Red (hot gas side): prescribed heat flux
- Pink (injector side): adiabatic

Adiabatic conditions were applied to the injector and nozzle ends of the chamber, where axial heat transfer was considered negligible due to the low thermal gradients. On the ambient side, heat loss was modeled using Newton's law of cooling (Equation 2.15) to represent natural convection. Radiative losses were neglected based on established literature indicating that, for metallic surfaces such as copper operating at moderate temperatures, natural convection dominates over radiation in terms of heat dissipation [69].

The hot gas wall, which is subject to intense thermal loading, was modeled with a spatially varying heat flux boundary. RoqFITT [45], a previously validated inverse solver, was used to reconstruct the wall heat flux based on thermocouple measurements within the copper structure. Since the inverse method yields discrete values only at thermocouple locations, the flux data were interpolated to generate a continuous profile along the chamber contour, providing a realistic thermal boundary condition for simulation.

5.2.2. Direct Problem and Optimization

The energy conservation equation used by ANSYS Fluent for solid domains has the following general form:

$$\frac{\partial}{\partial t}(\rho h) + \nabla \cdot \left(\vec{v}\rho h\right) = \nabla \cdot (\lambda \nabla T) + S_h \tag{5.1}$$

Where h is the sensible enthalpy, S_h the volumetric heat source, while $\vec{v}$ the velocity field applied to the motion of the solid zone [70]. For the present analysis, the chamber walls are assumed to be stationary and without internal heat generation, allowing the equation to be simplified to:

$$\frac{\partial}{\partial t}(\rho h) = \nabla \cdot (\lambda \nabla T) \tag{5.2}$$

Expressed in Cartesian coordinates, this reduces to:

$$\frac{\partial T}{\partial t} = \frac{\lambda}{\rho c_p}\left(\frac{\partial^2 T}{\partial x^2} + \frac{\partial^2 T}{\partial y^2} + \frac{\partial^2 T}{\partial z^2}\right) \tag{5.3}$$

Solving this equation provides the temperature field as a function of space and time within the copper chamber. At the hot gas interface, the imposed boundary condition is therefore a surface heat flux, defined as:

$$\dot{q} = -\lambda \left.\frac{\partial T}{\partial n}\right|_s \tag{5.4}$$

ANSYS Fluent solves this system using a finite-volume discretization. The computational domain of the subscale chamber is divided into finite control volumes, called cells, where a mean value is calculated and assigned to the center of the cell, called node. By imposing appropriate boundary and initial conditions, an algebraic system of conservation equations, numerically solvable, is then computed by balancing flows on the cell surfaces [70].

After solving the direct problem in Fluent, the resulting temperature field is evaluated at the discrete locations corresponding to the positions of the thermocouples, and then grouped in the vector $\boldsymbol{T}_{calc}$. The set of surface heat flux values used to define the boundary condition of the hot wall is collected in the vector $\boldsymbol{Q}$, while the temperature measured by the thermocouples is stored in the vector $\boldsymbol{T}_{meas}$.

Vectors $\boldsymbol{T}_{calc}$ and $\boldsymbol{Q}$ have size $N \times 1$, with N corresponding to the number of optimization points, while vector $\boldsymbol{T}_{meas}$ has size $M \times 1$, with M being the number of thermocouples. For the problem to not be ill-posed, $N \leq M$, since a larger number of optimization points than thermocouple measurements does not increase the input of information, but only the degrees of freedom of the problem.

The goal of the optimization is to minimize the residual between the calculated and measured temperatures. The residual function is defined as follows:

$$f(\boldsymbol{Q}) = \boldsymbol{T}_{calc}(\boldsymbol{Q}) - \boldsymbol{T}_{meas} = 0 \tag{5.5}$$

To solve the heat fluxes vector $\boldsymbol{Q}$ in the next iteration step, the problem is linearized and the Newton-Raphson method is applied [71]:

$$\boldsymbol{S}^T \boldsymbol{Q}_{k+1} = -\left(\boldsymbol{T}_{calc}(\boldsymbol{Q}_k) - \boldsymbol{T}_{meas}\right) + \boldsymbol{S}^T \boldsymbol{Q}_k \tag{5.6}$$

Where k is the iteration step, while S the Jacobian Matrix of partial derivatives:

$$\boldsymbol{S} = \frac{\partial \boldsymbol{T}}{\partial \boldsymbol{Q}} = \begin{bmatrix} \frac{\partial T_1}{\partial Q_1} & \cdots & \frac{\partial T_M}{\partial Q_1} \\ \vdots & \ddots & \vdots \\ \frac{\partial T_1}{\partial Q_N} & \cdots & \frac{\partial T_M}{\partial Q_N} \end{bmatrix} \tag{5.7}$$

Once the convergence criterion on the temperature residual is met, the solution progresses to the next time step.

This process is supported by the Jacobian matrix, which represents the sensitivity of each calculated temperature with respect to each heat flux component. In other words, it captures how heat applied at the surface “travels" through the solid wall to affect the thermocouple reading, acting as a map of influence.

Since the Jacobian matrix, as demonstrated by N. Perakis et al [45, 62], is determined solely by the geometry of the chamber, the thermocouple positions and the thermal properties of the material, it

remains constant in all tests performed on the same hardware. This allows the sensitivity matrix to be computed once and then reused, significantly improving computational efficiency. In this study, the Jacobian matrix was calculated separately for each chamber configuration and azimuthal pair, to account for variations in the thermocouple arrangements. Specifically, Azimuthal positions 1 and 5 (with 14 thermocouples, as shown in Figure 4.5), producing a 14×7 sensitivity matrix, while Azimuthal positions 3 and 7 (with 7 thermocouples, as visible in Figure 4.6), resulting in a 7×7 matrix.

5.2.3. Solver Inputs and Outputs

A summary of the solver input settings used for the optimization is provided in Table 5.1. These values were selected to ensure convergence while maintaining a reasonably low computational cost.

Table 5.1: Inverse solver configuration parameters

Parameter	Value	Description
Time step Δt	10 ms	Fixed time increment
Max iterations solver	50	Maximum allowed solver iterations
Max iterations Fluent	15	Maximum allowed Fluent iterations
Convergence criterion	Mean < 0.1 K	Residual of averaged temperature error below a threshold
Extrapolation method	Cubic	Type of temporal extrapolation for boundary condition updates
Local minimum value	0.01 K	Minimum residual change
Local minimum iterations	5	Enables early stopping if residual stagnates for consecutive iterations

The run length, which depends on the criteria mentioned above and the evaluation time window, was about 90 - 120 minutes per azimuthal position of each test.

The results of the inverse solver RoqFITT, which is the heat flux profile on the chamber wall, spatially and temporally resolved, are shown with the respective thermocouple measurements in Figure 5.4. The graph shows the relationship between the input and output of the solver for a reference test, at a chosen azimuthal location, while Figure 5.5 complements it by the spatial location of the thermocouple placement / heat flux calculation along the chamber contour.

In general, seven locations were chosen, on the chamber x-axis, for the heat flux calculation (solid line) from the temperature measurements (dashed line), regardless of whether the thermocouples at the selected azimuthal were 7 or 14.

Location 7, corresponding to the throat section, consistently exhibited the highest thermal loading, as expected due to its geometric and flow characteristics: high gas velocity, high dynamic pressure, and thin boundary layers result in intensified convective heat transfer to the wall. For this reason, making it the most critical region for evaluating chamber durability and cooling effectiveness, the throat location was selected as reference for the comparative discussion and sensitivity analysis throughout this thesis.

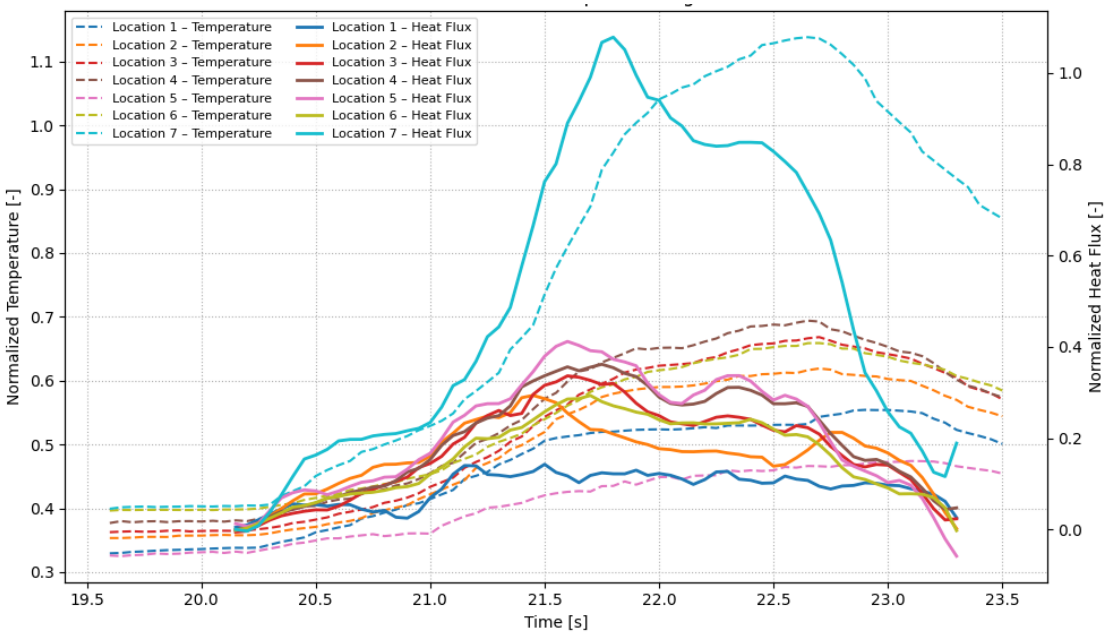

Figure 5.4: Heat flux reconstruction vs temperature measurement over time

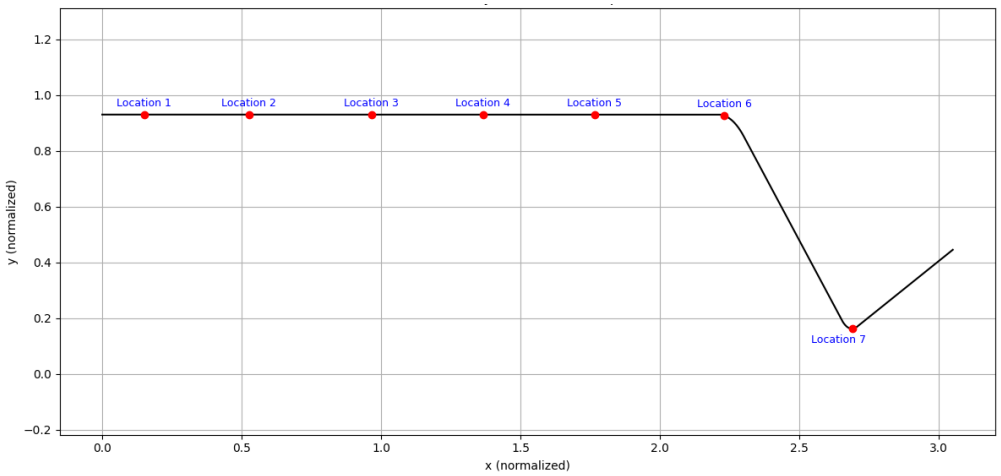

Figure 5.5: Chamber contour and thermocouple locations

5.3. Hot-fire Timing Framework

To properly interpret the time-evolving heat flux profiles obtained from the inverse solver, this chapter establishes a consistent framework for reading the hot-fire data. This includes segmenting each test chronologically into clearly defined combustion phases, aligning the transient heat flux results to the chamber pressure signal, and defining averaging windows, in preparation to the sensitivity study.

Test Key Phases

To aid in the interpretation of the evolution of the combustion process time, five key phases have been identified, based on chamber pressure progression. Figure 5.6 shows them for a reference nominal hot-fire test, together with chamber signal and computed heat flux (in the throat) for the four azimuthal positions.

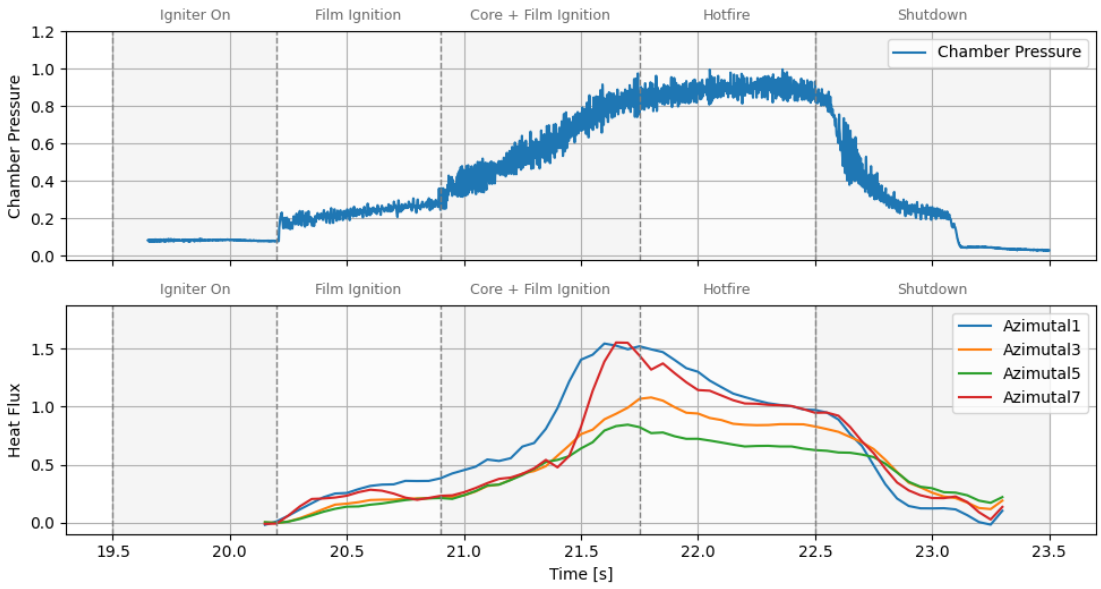

Figure 5.6: Hot-fire key phases

The test key phases can be summarized as follows:

1. Igniter On – pre-ignition where only LOX curtain and igniter are on
   - Chamber pressure is very low, with minimal pressure oscillations
   - Combustion is not yet established with Propane, therefore no heat flux is computed
2. Film Ignition – Propane curtain is injected in the chamber
   - Chamber pressure and pressure oscillations rise
   - Initial heat flux is calculated, as the wall begins to absorb heat
3. Core + Film Ignition – core propellants are injected, initiating transient flame establishment and anchoring
   - Pressure increases sharply, so the fluctuations
   - Usually the most thermodynamically aggressive transient
4. Hotfire – steady state combustion
   - Chamber pressure stabilizes, and heat flux remains high
5. Shutdown – fuel rich shutdown, where LOX is stopped before Propane
   - Both chamber pressure and wall heating decay rapidly

Although the inverse method solution could have been applied to the entire length of the test, only a focused time window for the evaluation was chosen, starting just before film ignition and extending almost until the end of the shutdown phase. This allowed to capture all physically significant stages of the hot-fire and, at the same time, reduce the computational cost of the inverse method.

The analysis presented in the results section will focus exclusively on the hot-fire phase, defined as the time window where the mean chamber pressure is relatively constant and combustion is fully established. By concentrating on this portion of the signal, the analysis becomes more reliable, minimizing sensitivity to transient uncertainties.

Temporal Alignment

Looking at Figure 5.4, there is a short time delay between heat flux evaluations and thermocouple measurements, where the heat flux appears to be 'faster' than the temperature reading itself. This offset is a direct consequence of thermal conduction within the copper wall; the inverse method calculates the heat flux at the inner chamber surface, while the thermocouple is embedded deeper in the wall. As the heat diffuses inward, the temperature response at the sensor is naturally delayed.

The inverse solution was performed with time delay $\tau = 0$, justified by the assumption of very fast response time (around 30-50 ms) when using 0.5 mm Type *K* Classe *I* thermocouples embedded in a highly thermally conductive metal. A manual time shift of 100 ms was applied to the heat flux profile (forward) to better align it with the chamber pressure evolution, enhancing the accuracy of the sensitivity analysis that will be presented in the results. However, this adjustment does not compensate for the inherently slower rise behavior of the thermocouple signal, which may result in a systematic underestimation of peak heat flux values.

To reinforce the robustness of the chosen assumption of $\tau = 0$, the possibility of a thermocouple response delay, estimated at approximately 50 ms, was included in the error analysis presented later in Chapter 5.7. When quantified, the resulting impact on the heat flux magnitude was found to be negligible. This confirms that the chosen temporal alignment, including the 100 ms shift and $\tau = 0$ assumption, does not introduce significant bias in the reconstructed thermal profiles.

Averaging Window Selection

To enable a consistent and comparative evaluation across tests, four averaging windows, customized for each test, have been selected within the hot-fire key phase. Figure 5.7 shows the intervals selected for a reference test, with respect to the chamber pressure signal and the heat flux profile of all four azimuthals.

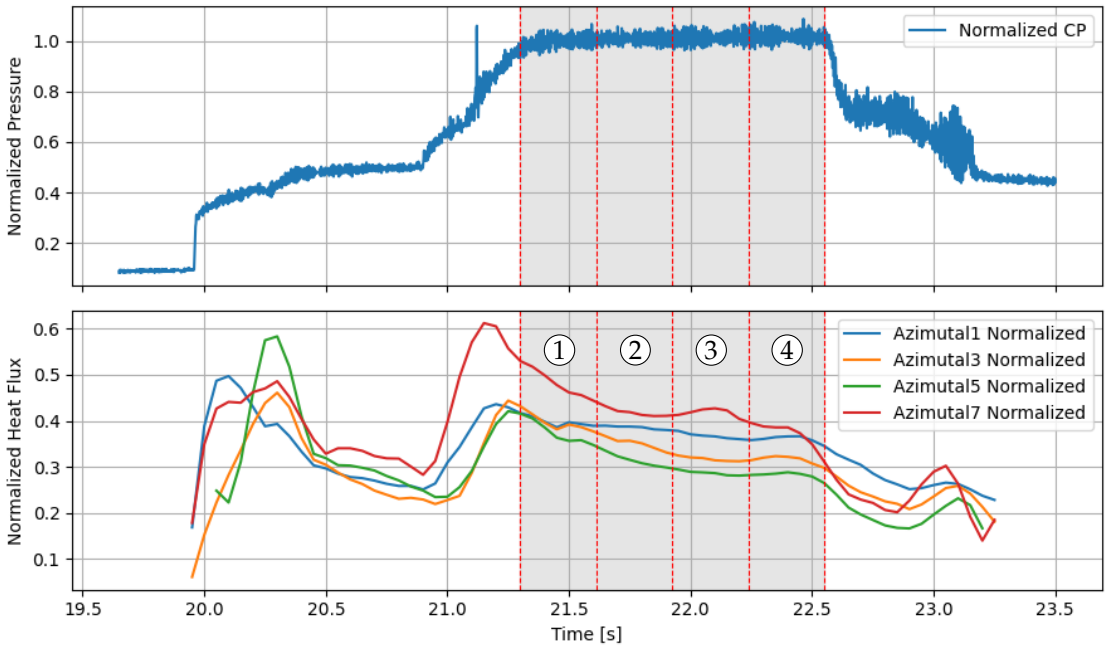

Figure 5.7: Averaging window selection on the reference test 1005_0

Intervals 2-3 were used for most of the sensitivity study, since these intervals correspond to a well-established combustion process. Intervals 1 & 4 instead, were used only as additional data points for a qualitative study on the relationship between combustion instabilities and heat flux, being these edge-intervals usually more subject to pressure fluctuations.

5.4. Variable Classification & Normalization

In this section, the different variables chosen for the sensitivity analysis are presented along with the normalization process employed.

Variables Analyzed

The variables considered in the sensitivity analysis are grouped on the basis of their nature: initial parameters, which are directly commanded or set prior to each test, and derived parameters, which are outcomes of the combustion process or measured system response. This categorization was made to support a clearer cause-effect interpretation for the following analysis.

Initial parameters:

- O/F curtain → Film oxidizer-to-fuel ratio
- O/F core → Core oxidizer-to-fuel ratio
- Total mass flow → Core + curtain propellant total mass flow
- Curtain ratio → Ratio of curtain-to-core mass flow
- Temperature fuel → Injection temperature, averaged between core and curtain
- Temperature oxidizer → Injection temperature, averaged between core and curtain

Derived parameters:

- Chamber pressure → Averaged over intervals 2-3
- Pressure oscillations → Computed with standard deviation over all intervals
- Combustion efficiency → Obtained from ideal and real c-star (Equation 2.9)
- Heat flux → Azimuthally resolved, averaged over intervals 2-3 (and 1-4 when compared to pressure oscillations)

Normalization Criteria

Two approaches were used to process and present the data, depending on the purpose of the analysis:

Normalization for Comparative Graphics:

- Applied in heat flux plots, comparing graphs and test matrix
- Preserved qualitative relevance while masking company-sensitive data through division by a constant reference value

Standardization for Statistical Modelling:

- Used for data of the second campaign, where statistical models were applied
- Variables were standardized (mean-centered and scaled to unit variance) to facilitate numerical stability and proper weighting in regression models, preventing bias caused by differing physical units or ranges
- This enabled a more interpretable and robust assessment of how parameters such as O/F or propellant temperature influence wall heat flux distribution

By tailoring the data treatment to the analysis goal, clarity was improved without sacrificing physical rigor.

5.5. Test Campaigns Logic

The two test campaigns carried out in this research differ substantially in their objectives, which are presented in this chapter along with a description of how the initial parameters were varied.

1st Campaign: Injector Screening
The first campaign involved qualitative screening of six different core injector geometries, with the aim of selecting a candidate that would satisfy the requirements of stability (low chamber pressure oscillations), efficiency (high η_{c^*}) and did not disrupt the film flow (showing low wall heat flux). No more than four tests were performed per injector design, as the element was replaced whenever it failed to meet one of the aforementioned requirements. During the first campaign, the chamber hardware was also changed from the Mach-scaled to the Pressure-scaled configuration.

Due to the limited amount of tests per injector design, the increased complexity of including geometrical parameters as variables, and the use of two different chamber configurations, limited variations among the initial parameters were applied, mostly driven by safety considerations rather than systematic mapping intent:

- O/F core was swept from conservative values to more optimal and performance-drive ratios, which was part of the injector evaluation effort to screen by combustion efficiency and pressure stability
- O/F curtain was gradually increased during the campaign, for safety reasons due to initial heat flux uncertainties
- Curtain ratio and total mass flow rate were held relatively constant throughout the campaign
- Propellant temperatures, especially the fuel one, varied substantially across tests; variations over 20 K between tests with the same injector, as well as up to 40 K across tests with different injector

2nd Campaign: Load-point Mapping
The second campaign, focused on a single injector candidate, allowed the analysis to isolate how individual physical parameters influence wall heat transfer and combustion dynamics. With a fixed geometry, the initial parameters could then be varied more systematically, as reflected by the variable evolution:

- O/F core was swept from conservative to optimal values
- O/F curtain was held at the target value, with small (unwanted) deviations
- Curtain ratio was intentionally swept across three clusters of values
- Core mass flow rate was maintained nearly constant along the campaign, to keep a fixed core injector mass-loading
- Total mass flow shifted accordingly with the curtain-side adjustments
- Propellant temperatures were varied mildly from test to test, with small variations in between core & curtain of the same propellant

5.6. Sensitivity Analysis Tools

To support the interpretation of inverse heat flux trends and trying to identify the dominant physical drivers, several techniques were employed in this work. These tools were used to quantify the relative importance of different parameters and reveal potential coupling or redundancy between inputs.

The approach integrates multiple perspectives, visual, statistical, and interpretive, to ensure that findings are robust across both numerical and physical reasoning. The following subsections summarize the key techniques used and explain the rationale behind their selection.

Visual Trend Analysis
After analyzing asymmetries in heat flux profiles among different azimuthal positions, 2D scatter plots were used in the early phase to investigate how individual parameters influence the wall heat flux. This approach enables direct visual inspection of potential trends without the abstraction of numerical models, making it possible to observe patterns, offsets, or nonlinear behavior inherent to the experimental data.

For 2D scatter plots, each data point represents an averaged value evaluated over a fixed sub-interval. The horizontal axis reflects a selected input parameter, while the vertical axis captures the resolved heat flux (also averaged within the same sub-interval). Although not explicitly plotted on either axis,

chamber pressure was also encoded using color gradients to convey its role as a contextual variable, knowing its well established relation with heat flux. This format offers a clear and intuitive view of how key variables interact at a steady-state level, making it easier to detect physical tendencies or outliers early in the analysis. Unlike time-resolved visualizations, which emphasize dynamic evolution, these plots emphasize condition-dependent behavior and support a qualitative interpretation of the test matrix structure.

Pearson and Partial Correlations

To analyze linear relations among input variables and their dependence with the wall heat flux, both Pearson and Partial correlations were used. Pearson correlation served as an initial diagnostic tool, quantifying the strength and direction of the dependencies with its coefficients. It helped identify strong couplings, redundancies, and variables that could be heat flux drivers.

To further refine these insights, partial correlation was used to assess whether the observed relationships were maintained when controlling for the influence of other variables. This was particularly important in the presence of collinearity, where apparent associations could be misleading. By isolating the unique contribution of each variable, the partial correlation helped to distinguish genuine effects from secondary correlations.

Variance Inflation Factor

Variance Inflation Factor (VIF) analysis was used to further probe interdependencies between input variables. Although partial correlation isolates relationships between pairs of variables while controlling for the rest, VIF extends this idea by quantifying how much each predictor is linearly explained by all other predictors in the set. In doing so, it provides a numerical measure of multicollinearity, a condition that can compromise the reliability of regression modeling.

VIF values indicate how much the variance of a regression coefficient would be inflated because of the overlap with other variables. A high VIF suggests that a given input may be redundant in the presence of others, meaning that any model that includes it may struggle to distinguish its unique effect. By highlighting such cases, the VIF served as a filtering tool to identify predictors that could undermine the stability or interpretability of subsequent modeling.

Multiple Linear Regression

Finally, multiple linear regression was employed as a tool to evaluate how multiple physical input parameters jointly influence the wall heat flux reconstructed from the inverse method. The purpose was to identify which variables have the greatest impact and how their effects combine under realistic conditions.

In essence, MLR works by fitting a best-fit linear relationship between several inputs and the observed heat flux output. Each input is assigned a coefficient that describes the strength and direction of its contribution. This approach is particularly effective when the data set contains enough variation to distinguish the effect of one parameter from the other. It was chosen for its balance of simplicity and interpretability. MLR offers a quantitative foundation for assessing physical trends and identifying potential interactions.

Overall, MLR allowed the analysis to go beyond visual inspection and into measurable attribution, highlighting which physical variables might drive the heat transfer behavior and which might be more secondary under the tested conditions.

5.7. Error Analysis

To provide a meaningful analysis of the heat flux data, it is essential to quantify the sources of error affecting the wall heat flux evaluation. All errors, here expressed as a percentage of the average steady-state heat flux at the throat location, are divided into two categories: systematic and random.

Systematic errors are those that consistently bias the measurements in a predictable way across all tests and azimuthal locations. Among them, sensor placement uncertainties, resulting from tolerances in seat depth and hole drilling, are among the most influential. A small deviation in the mounting position alters the effective thermal path length, misrepresenting the reconstructed heat flux values. Similarly,

modeling the temperature-dependent thermal conductivity of copper introduces a fixed uncertainty, since it is based on interpolated data sets (such as those provided by NIST) which may not perfectly reflect the actual test hardware. The outer wall boundary condition is treated as purely convective, which neglects minor radiative losses to ambient, also introducing a small systematic offset. Further contributions come from the thermocouple calibration tolerance itself, defined by Class I specifications under IEC standards. Lastly, thermal gradients along signal cables and cold junctions can generate voltage offsets, small but consistently present in every measurement. All systematic errors considered in this analysis, with their relative weighted error, are presented in Table 5.2.

Table 5.2: Systematic error

Source	**Rationale**	$\Delta T[K]$	**% of** $\bar{q}_{th}$
Thermocouple calibration offset	Type K, Class I, 0.5 mm tip	± 1.5 K	± 0.53%
Cable and cold-junction EMF	Temperature differences along cable and cold junction	± 0.3 K	± 0.11%
Seating-depth bias	± 0.2 mm uncertainty of sensor placement	± 8.2 K	± 2.87%
Hole depth	± 0.2 mm from CNC tolerance	± 8.2 K	± 2.87%
Copper $\lambda(T)$ modelling accuracy	± 2% of NIST database + interpolation	± 5.7 K	± 2%
Exterior boundary condition (no radiation)	Radiative loss on colder wall to ambient (~5%)	± 1 K	± 0.35%
Systematic Error	Square root of sum of quadratic error source terms	± 13.1 K	**± 4.57%**

Random errors, on the other hand, vary from test to test depending on environmental conditions, sensor dynamics, and operational fluctuations. A prominent source is signal noise, which includes acquisition jitter, electromagnetic interference, and quantization effects introduced by analog-to-digital conversion during data processing. These components, though relatively small individually, can collectively degrade the fidelity of transient temperature readings. Another random contributor with moderate relevance is the inherent response delay of the thermocouple, which results from the time required for the heat to pass from the copper wall to the sensor pearl. Although this might seem systematic, since the time delay should be constant, the error itself depends on the steepness of the thermal gradient, which varies within tests; this delay can alter the temporal alignment and affect the heat flux magnitude, especially near heat flux peaks. Seating misalignments due to mechanical re-clamping originated by in-test vibration can further vary the thermal contact quality between sensor and wall, influencing heat transfer locally. One of the most physically significant contributors to the random error is the soot layer deposition, which may form during combustion. These carbon-based layers act as thermal insulators on the surface of the inner wall, masking the true heat flux reaching the copper. Their thickness and distribution can vary across tests depending on propellant ratios, ignition efficiency, and burn duration, rendering this shielding effect inherently random. The list of random errors taken into account in this investigation is shown in Table 5.3, along with their error weight.

Combined, systematic and random errors result in a total uncertainty of approximately 6.7%.

For the heat flux error calculation, the Jacobian matrix at the throat location was used, which expresses how sensitive the local heat flux is to a temperature perturbation, through the following relation:

$$\Delta q = \frac{dq}{dT} \cdot \Delta T \tag{5.8}$$

Variations in heat flux resulting from a different sensor position Δx or change in material thermal conductivity $\lambda(T)$ were instead calculated using Fourier's law of heat conduction, shown in Equation 2.13.

Table 5.3: Random error

Source	**Rationale**	$\Delta T[K]$	**% of** $\bar{q}_{th}$
Solver residual	Mean $\Delta T < 0.1$ K, assumed high local gradient	± 0.5 K	± 0.175%
Thermocouple lag	50 ms sensor delay	± 7.1 K	± 2.5%
DAQ + SG filter noise	Data acquisition and filtering noise	± 0.05 K	± 0.018%
EMI / vibration cable jitter	Electromagnetic and vibration influence	± 0.1 K	± 0.035%
PLC A/D quantization	16-bit analog / digital conversion	± 0.02 K	± 0.007%
Sensor re-clamp misalignment	± 0.2 mm sensor movement under vibration	± 8.2 K	± 2.87%
Soot layer thermal, shielding	± 0.05 mm soot layer with low thermal conductivity	± 8.5 K	± 3.0%
Random Error	Square root of sum of quadratic error source terms	± 10.9 K	**± 4.85%**

During most of the following analysis, the heat flux results are analyzed at one azimuthal location at a time, which means that the absolute amplitude of heat flux (systematic error) is less relevant, and that what matters is the variation between tests at the same location (random error). For this reason, the random error (< 5%) is the dominant uncertainty component in the analysis (except for chapter 6.1.1, where the azimuthal difference is discussed).

6

Results

This chapter presents the outcome of the heat flux analysis carried out on the two test campaigns performed. During the First Campaign, six coaxial semi-swirler core injectors were tested, to select a candidate design that balanced low combustion instabilities, high combustion efficiency, and moderate heat loads. The P1I injector emerged as the top candidate, satisfying these requirements, and it has been employed in the Second Campaign, in which load-point parameters were systematically varied to map their effect on combustion efficiency, combustion instabilities, and heat flux loads.

For each test run, the RoϱFITT inverse solver reconstructed the temporal heat flux profile at seven axial locations, in four different azimuthal positions. The results shown in this chapter refer only to the heat flux obtained at the throat location, which corresponds to the most critical region for thermal loads. As discussed in Chapter 2.3 and illustrated in Figure 2.3, the throat region experiences peak heat flux due to the combination of high gas velocity and minimal boundary layer thickness. This concept is also supported by the Bartz correlation [15], commonly used to estimate convective coefficients, with its area-dependent relation.

To enable consistent comparisons among key operating parameters, heat flux profiles were averaged over four sub-intervals within a steady hot-fire phase, as defined in Chapter 5.3, along with the mean chamber pressure and its standard deviation p'. For most of the analysis presented in this study, only averages on the window of sub-intervals 2-3 combined were selected, corresponding to the most stable portion of the hot-fire phase. However, in Chapter 6.1.2, where the relationship between chamber pressure fluctuations and wall heat flux is explored, intervals 1 and 4 are also used to calculate the averages, to include instabilities typically manifested near ignition and shutdown transients. It is worth mentioning that after this section, only heat flux results of the Second Campaign are considered, given the increased complexity introduced by the multiple hardware transition in the First Campaign.

The complete test matrix, including all tests and their respective initial conditions, is provided in Appendix B. Appendix C shows the corresponding heat flux profiles and chamber pressure signal for each individual test. What follows in this chapter is first a visual observation of the influence of different parameters on the heat flux of the throat wall and then a statistical quantification of the role of each variable through correlation and regression techniques.

6.1. Visual Trend Analysis

Before diving into formal statistical correlations and modeling, this section introduces a visual interpretation aimed at revealing dominant physical trends within the test data set. It begins by highlighting differences in heat flux evaluations across azimuthal locations, followed by an analysis of key operating parameters plotted against computed heat flux. The chamber pressure is encoded through color mapping in each plot, given its well-established influence on heat transfer. These visual insights offer a statistics-free perspective, potentially revealing direct dependencies, non-linear patterns, and threshold effects, while laying the groundwork for interpreting subsequent correlation and regression results.

6.1.1. Heat Flux Azimuthal Discrepancies

The calculated throat heat flux across different azimuthal locations reveals a significant spread in values, especially in the Pressure-scaled chamber tests of the Second Campaign. Figure 6.1 illustrates a representative example of this phenomenon, showing the normalized chamber pressure and the reconstructed heat flux at the throat for the four azimuthal locations. As seen in this, and then confirmed by other tests of the Second Campaign (see Appendix C for reference), Azimuths 1 and 7 often exhibit markedly higher wall heat flux than Azimuths 3 and 5. Across the broader dataset, azimuthal discrepancies generally range from 30% to 70% of the nominal heat flux, but in rare occasions (such as for test 1018_1, shown in Figure 6.1) up to 100%.

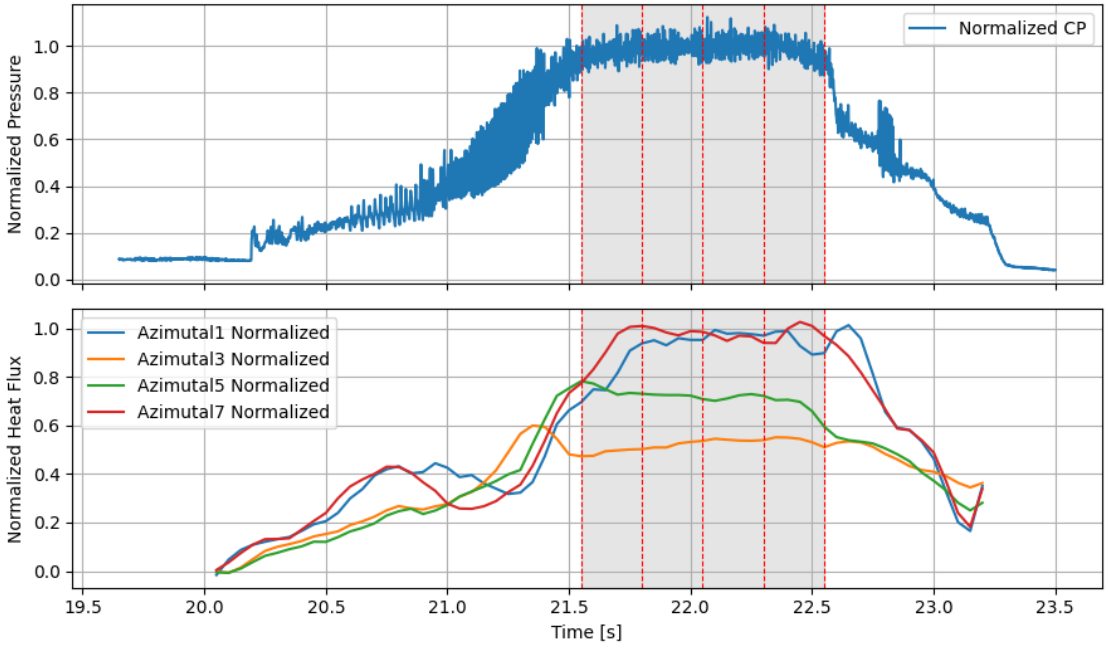

Figure 6.1: Heat flux evaluation at all 4 azimuthal locations for the reference test 1018_1

Such spatial variation cannot be attributed solely to sensor errors, since the error analysis presented in Chapter 5.7 estimated a total uncertainty on the heat flux measurement of approximately 6-7%. It is clear that this azimuthal discrepancy reflects underlying physical processes, rather than measurement errors.

A likely source lies in the asymmetry of the curtain film-hole pattern introduced in Chapter 4.2.2. The injector plate employs a reactive-film configuration, introducing oxygen and propane through two concentric rings of showerhead holes arranged asymmetrically around the chamber circumference. This uneven distribution of the oxidizer and fuel holes leads to varying local flow patterns, resulting in distinct combustion dynamics and cooling behavior at different azimuthal positions.

The Mach-scaled chamber configuration used in the early phase of the First Campaign, which displayed more uniform azimuthal heat flux values (visible in Figures C.1, C.2, C.3 and C.4 of Appendix C) might have had a slightly different alignment of the injector head with respect to thermocouple azimuthal orientation, which changed how the film-hole array intersected each measurement plane. In addition, the larger throat diameter, which results in a gentler curvature and better film attachment, might have reduced this azimuthal discrepancy for the Mach-scaled configuration.

In general, similar findings of different heat flux results per azimuthal locations have been documented in past literature. Arnold et al. [72] evaluated circumferential heat-flux variations in a LOx/H_2 chamber with inert film cooling and observed deviations up to 25%, driven by swirl and vortex-induced film displacement. Suslov et al. [41] rotated the test hardware to reveal film-induced thermal asymmetries caused by the injector geometry and the distribution of the curtain holes. These studies, while based on

inert film designs, underscore how injector-driven dynamics can lead to azimuthal flux variation, an effect which can be even more amplified when the film is reactive.

In reactive-film configurations, the curtain propellants burn near the wall, creating secondary flame zones and chemically active boundary layers. These reactive regions amplify local heat release and modulate shielding non-uniformly, especially when swirl components or instabilities are present. Consequently, even two azimuthal planes with seemingly similar hole patterns can exhibit different thermal behavior. This is exemplified by the comparable film-hole layout located in the radial orientation of Azimuths 1 and 5, (as shown in Figure 4.7), which yielded distinct heat flux results (as illustrated in Figure 6.1).

Despite having performed attempts to correlate specific azimuths with geometric features, the dynamic behavior of the reactive film and its interaction with internal recirculation and core element swirl make it difficult to conclusively identify which hole pattern yields the highest thermal loading. In support of this, while Azimuths 1 & 7 generally register higher heat flux than Azimuths 3 & 5, there are notable exceptions where Azimuths 3 & 5 record comparable or even greater thermal loads. These occurrences further highlight the influence of transient flow behavior in shaping local heat-transfer conditions, making it difficult to definitively associate any specific film-hole layout with superior or inferior thermal shielding performance. For these reasons, in the upcoming analysis, comparisons between heat flux and key operating parameters are grouped by azimuthal locations. By doing so, both heat flux variations due to non-uniform film holes arrangement, as well as systematic errors, remain isolated within that azimuth and do not propagate across the dataset.

In summary, the observed azimuthal discrepancies in wall heat flux are substantial and their scale exceeds what is typically reported in inert cooling systems, likely due to the reactive nature of the curtain flow and its sensitivity to injector alignment and combustion stability. These findings highlight the importance of azimuthal resolution in thermal diagnostics and carry direct implications for future multi-element designs and film optimization strategies.

6.1.2. Chamber Instabilities versus Heat Flux

Figures 6.2 and 6.3 explore the relationship between pressure fluctuations (p') and throat heat flux at a selected azimuthal position, for all tests performed in First and Second Campaigns, respectively. In both figures, each marker represents the mean heat flux value (on y-axis) and the chamber pressure standard deviation p' (on x-axis), computed in one of the four sub-intervals of a test and normalized to a reference value, with different label ID for different tests. For Figure 6.2, the marker shape defines the injector design.

Despite variations across injectors and operating points, the scatter plots reveal a general trend, where tests associated with larger pressure oscillations tend to exhibit higher heat flux values at the throat location. Although this observation is consistent across injector families (Figure 6.2), and on tests of the selected injector P1I (Figure 6.3), some points deviate from the monotonic behavior, such as tests 0930_0 and 0618_0 in Figure 6.2, suggesting that pressure fluctuations are not the sole determinant of heat transfer, and that local variations in combustion dynamics may affect the heat flux results.

Another important observation from Figure 6.2 is the absence of a clear color gradient along the vertical axis. Intuitively, one would expect higher chamber pressures (red markers) to correspond with increased heat flux, appearing predominantly in the upper part of the plot, and vice-versa in the lower side. However, this is not consistently observed. This discrepancy reinforces the idea that injector geometry plays a significant role in shaping internal flow structures, with some configurations likely disrupting the curtain film. As a result, certain injectors may yield elevated wall heat flux even at relatively low chamber pressures, while others may maintain film integrity and limit the heat transfer, despite operating at higher pressures.

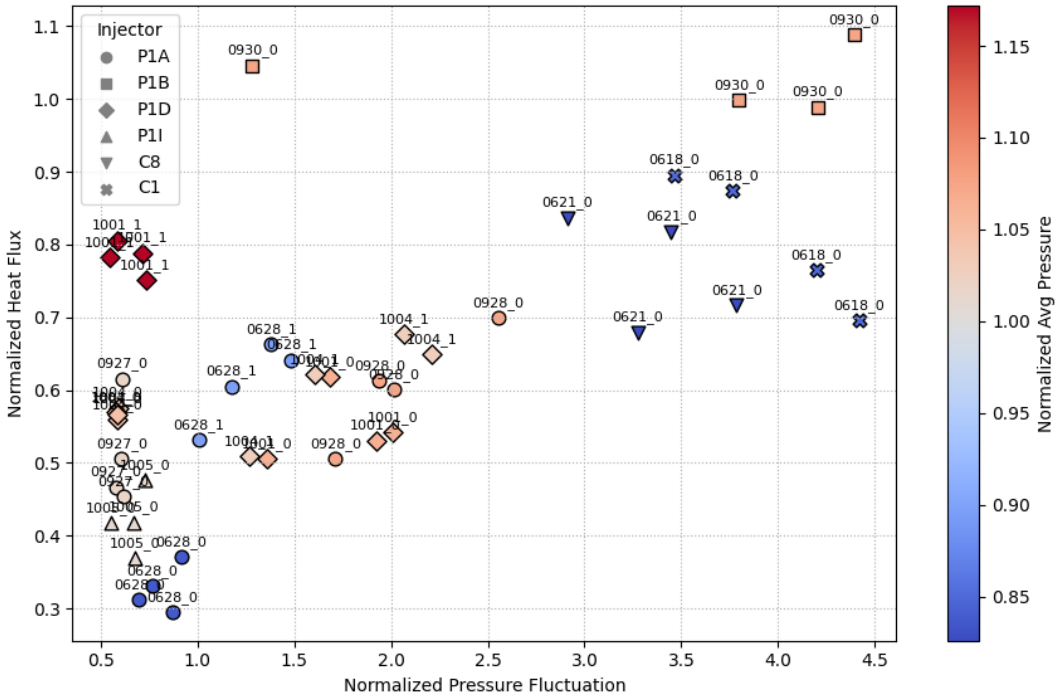

Figure 6.2: Pressure fluctuation vs heat flux at azimuthal 7 in 1st Campaign, with chamber pressure color-mapped and injector designs distinguished by marker shape

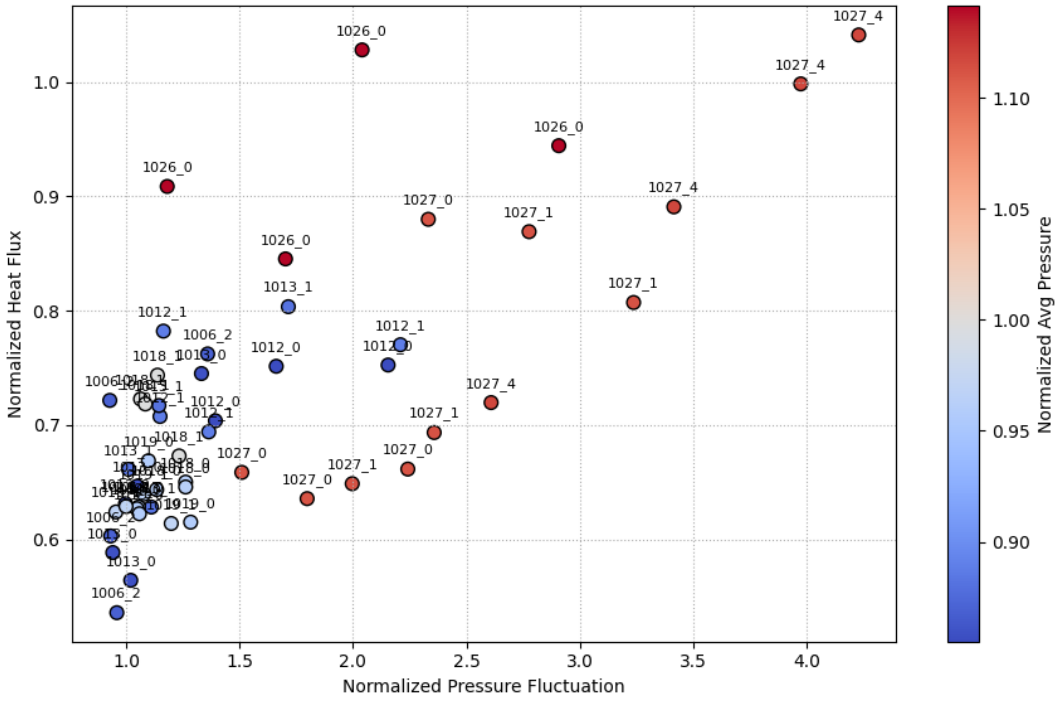

Figure 6.3: Pressure fluctuation vs heat flux at azimuthal 5 in 2nd Campaign, with chamber pressure color-mapped

The positive correlation between chamber pressure fluctuations and increased heat flux is aligned with the early work of Harrje et al. [61], who reported transient heating amplification up to 25% in unstable chambers. Instabilities can directly disrupt the protective curtain film or locally separate the film layer, exposing the copper wall to hot core gases or the secondary film flame. In addition, periodic fluctuations

in pressure may destabilize the boundary layer by modulating its thickness, and therefore increasing the convective heat transfer near the wall. As pressure waves are coupled with the release of oscillatory heat, the flame itself can pulsate or shift spatially within the chamber, intermittently approaching the wall, thus enhancing heat fluxes at the surface, as already experimentally observed by Ueta et al. [62].

It should be emphasized that the p' values shown were calculated from low-frequency pressure sensors, and although a high-frequency transducer was installed in the chamber, its signals were not analyzed in this thesis. No Fast Fourier Transformation or modal decomposition was performed, and so the nature of the instabilities was not investigated, as considered beyond the defined heat transfer-focused scope of this thesis. The complementary plots corresponding to the calculated heat flux at other azimuthal positions can be found in the Appendix D.

6.1.3. Curtain Ratio versus Heat Flux

Figure 6.4 presents the relationship between curtain ratio and heat flux, based on the tests performed during the Second Campaign. Each marker in the plot corresponds to the average heat flux value on sub-intervals 2-3, distinguished by azimuthal position through marker shape.

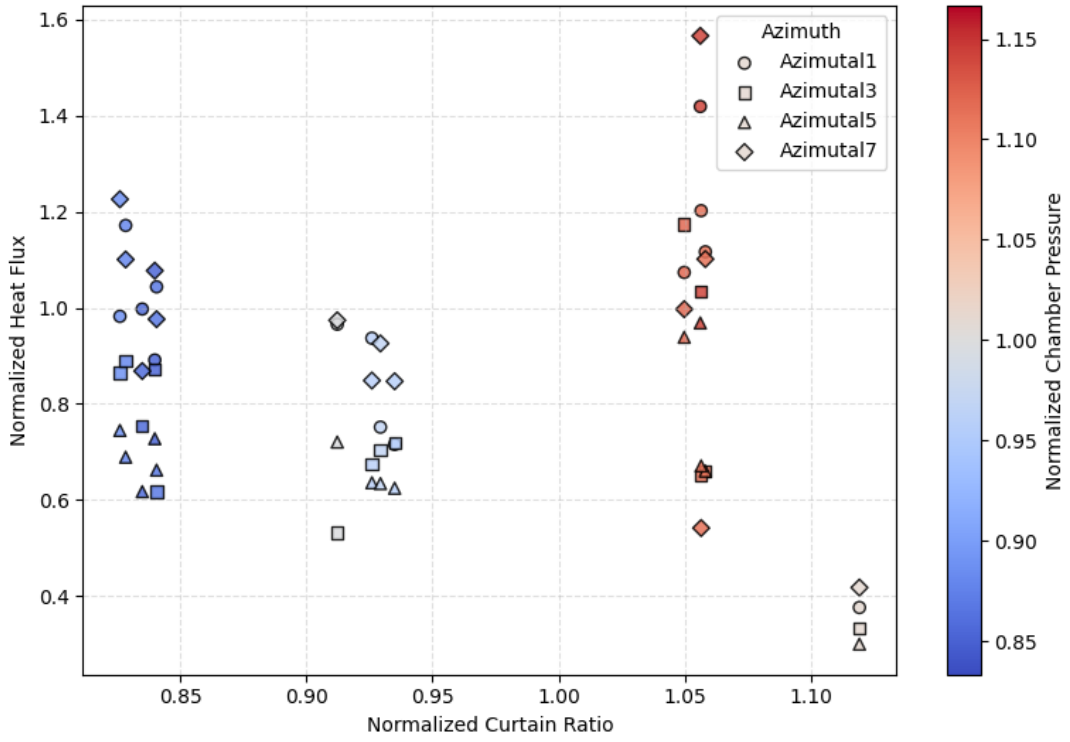

Figure 6.4: Curtain ratio vs heat flux in 2nd Campaign, with chamber pressure color-mapped and azimuthal distinguished by marker shape

A clear relation between curtain ratio and chamber pressure can be observed: tests conducted at lower curtain ratios correspond to lower chamber pressures, whereas high curtain ratio coincides with high chamber pressure. This connection has a causal nature because is a consequence of the methodology adopted during the test campaign, where only the curtain mass flow was progressively increased while the core mass flow loading was held constant; as a result, increasing the curtain ratio inherently led to a rise in total mass flow, therefore increasing the chamber pressure.

A distinct exception is observed for the data points in the bottom-right region of the plot, corresponding to the very first test conducted with the P1I injector. This test, carried out at the end of the First Campaign and included in the scatter plot solely for reference, featured a significantly lower curtain $^{O}/_{F}$ ratio compared to the other subsequent tests, where this parameter was held instead nearly constant. It should be noted that this test also exhibited lower heat flux values, which supports the notion that a more fuel-rich curtain, being less reactive, provides improved thermal shielding.

Focusing on the relation of curtain ratio with heat flux results, the data show a non-linear convex trend, characterized by a minimum. Although affected by the strong collinearity with chamber pressure, these results suggests that the film cooling effectiveness peaks at intermediate film ratios. At low curtain ratios, insufficient film mass flux results in partial wall shielding, while at higher ratios, excessive film promotes entrainment into the core flow, leading combustion gases closer to the wall.

This non-monotonic trend mirrors the entrainment-driven degradation of film effectiveness described in NASA SP-8124 [22]. Arnold [21] also validated this concept experimentally, using a showerhead curtain injection configuration with reactive-film (LOx/H2), which non-monotonic results were attributed to film detachment and entrainment in the core flow at high film ratios. This observation carries significant design implications, especially when trying to balance the conflicting requirements of low thermal loads and high combustion efficiency.

6.1.4. Other Notable Trends

In addition to the curtain ratio analysis, the influence on the wall heat flux of total propellant mass flow rate, core oxidizer-to-fuel ratio and combustion efficiency η_{c^*} was also investigated.

The comparison between the total mass flow rate and the heat flux (Figure 6.5) reveals a trend very similar to that observed for the curtain ratio, reinforcing the strong relationship between these two parameters discussed previously.

The plot of the core $^{O}/_{F}$ ratio versus heat flux (Figure 6.6) instead shows a scattered distribution with no clear correlation, suggesting little to no direct influence of the core mixture ratio on wall thermal loads. This lack of sensitivity is indicative of the effective shielding provided by the curtain film, which insulates the chamber walls from fluctuations in core mixture ratio. In fact, as reported by Suslov et al. [41] and Locke et al. [58], the presence of a well-formed film layer effectively buffers the wall from variations in core combustion intensity, even as the flame temperature changes with $^{O}/_{F}$. The reactive curtain, acting as a barrier zone, absorbs temperature variations of the core flame, while maintaining relatively constant wall heat flux, hence decoupling core mixture ratio from wall heat transfer.

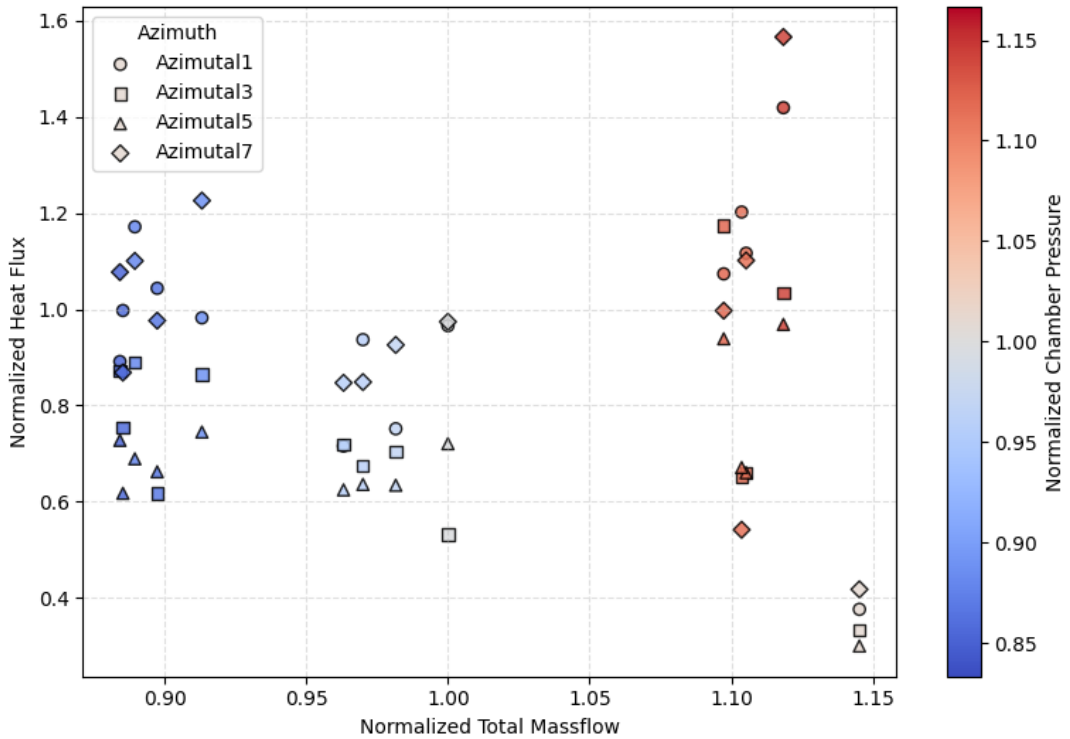

Figure 6.5: Total mass flow vs heat flux in 2nd Campaign, with chamber pressure colour-mapped and azimuthal distinguished by marker shape

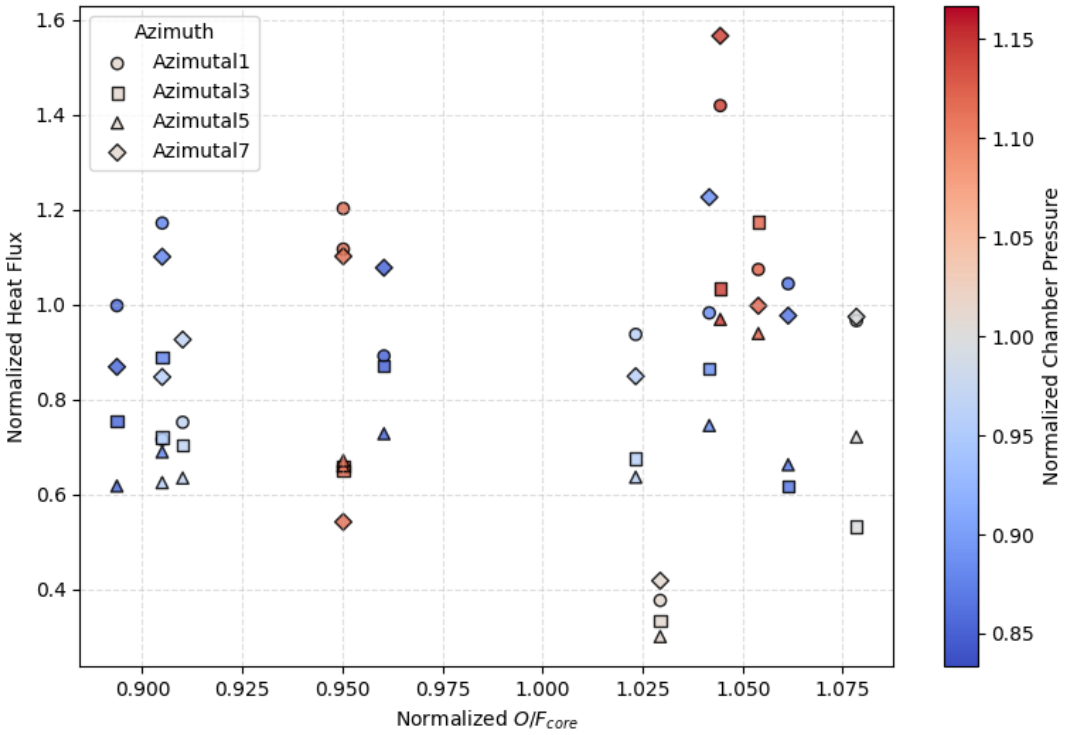

Figure 6.6: $^{O}/_{F}$ core vs heat flux in 2nd Campaign, with chamber pressure colour-mapped and azimuthal distinguished by marker shape

Lastly, in the comparison between heat flux and combustion efficiency shown in Figure 6.7, a trend emerges, suggesting a correlation between the latter and chamber pressure. This is visually indicated by the gradual shift in marker color (from blue to red) toward the right side of the plot, corresponding to higher combustion efficiencies. This relation is physically plausible, as elevated chamber pressures typically enhance propellant mixing and reaction rates, leading to more complete combustion. In fact, a higher combustion efficiency means that more chemical energy is converted to thermal energy, therefore leading to a rise in combustion temperature in the chamber core. Although film shielding may buffer some of this energy, studies by Silvestri et al. [52] showed that peak combustion efficiency values also correlated with higher local thermal load, particularly near recirculation zones or imperfect film coverage.

The scatter plots of the other variables versus heat flux results (which did not lead to any other meaningful correlation) can be found in the Appendix D.

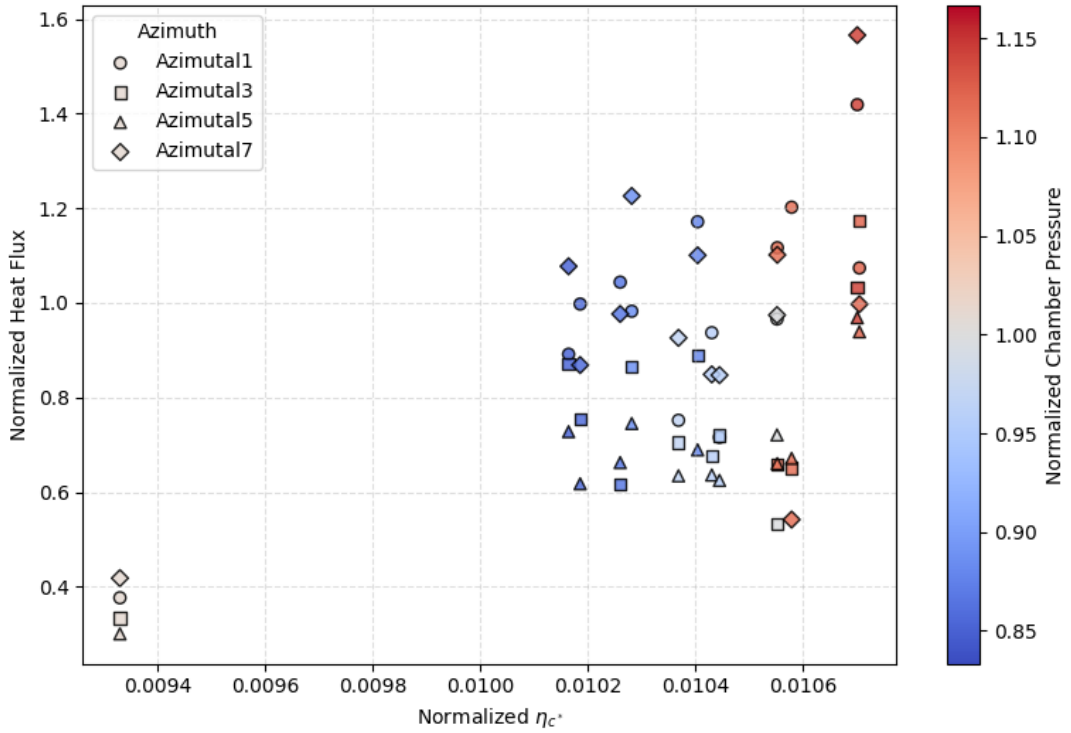

Figure 6.7: Combustion efficiency vs heat flux in 2nd Campaign, with chamber pressure colour-mapped and azimuthal distinguished by marker shape

6.2. Statistical Analysis & Modelling

Following the visual analysis, key trends and parameter correlations have emerged, providing an intuitive understanding of how parameters influence the resulting heat flux. However, to rigorously quantify the relative importance and interdependence of these variables, a more systematic approach is required. The following section continues the analysis within a statistical modeling framework designed to capture multivariate interactions and assess the significance of the variables to the heat transfer phenomenon.

6.2.1. Correlation Framework

To assess the strength and nature of relationships between parameters and wall heat flux, Pearson and partial correlation analyzes were performed. Pearson correlation was used to quantify direct linear associations between variables, while Partial correlation to account for hidden dependencies among variables and to better isolate their individual relationships.

Pearson Correlation

The Pearson correlation matrix is shown in Figure 6.8. Among the variables with a linear relationship to heat flux, combustion efficiency shows the strongest positive correlation. This trend is supported by the analysis made in Chapter 6.1.4, which shows that η_{c^*} is related to the chamber pressure and the release of combustion heat.

With a less strong linear dependency, chamber pressure and combustion instabilities are shown to positively affect heat flux, as seen already in Chapter 6.1. What seems new in this analysis is the strong positive correlation of the curtain $^O/_F$ ratio with heat flux. However, this trend lacks a clear physical basis: an increase in curtain $^O/_F$ implies a shift from a fuel-rich towards a more stoichiometric mixture in the film, which would typically enhance combustion intensity and potentially increase thermal loads. Since the curtain $^O/_F$ in the Second Campaign was not intentionally varied between tests (but rather kept at a fixed target value), the linear relation seen here is most likely an artifact due to the normalization process used, which inflated the Pearson coefficient.

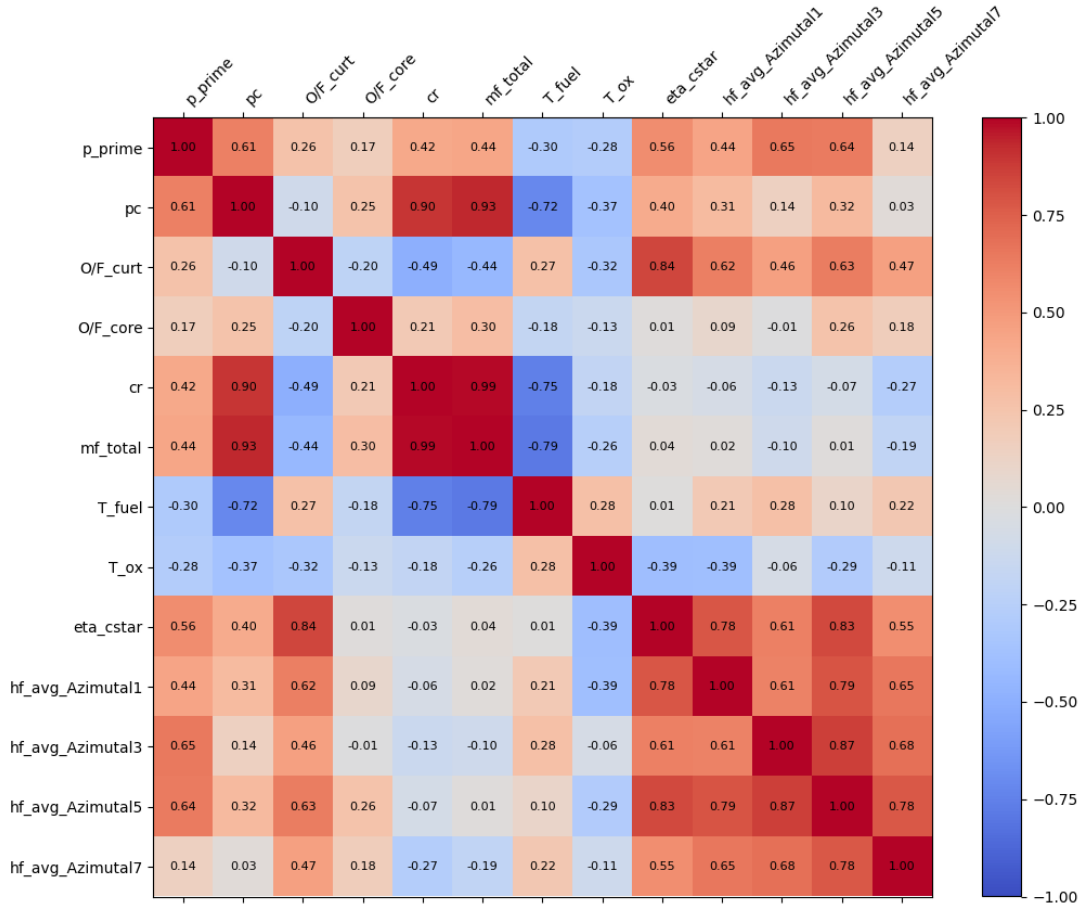

Figure 6.8: Pearson correlation matrix

With opposite relation trends, injection fuel and oxygen temperatures positively and negatively affect the wall heat flux, respectively. Although warmer propane is known to promote combustion near the chamber wall, the apparent negative correlation of heat flux with oxygen is less intuitive and could be influenced by multivariate interactions, which may mask its actual contribution. Another theory could be that hotter oxygen might be shifting the core flame inwards due to altered jet momentum and mixing profiles, leading to a reduction in localized thermal loading.

Among the most notable relations between other variables, there is a near-perfect correlation between the total mass flow rate and the curtain ratio. Both variables also exhibit a strong positive correlation with chamber pressure, which is consistent with the linear relationship described in Equation 2.6 and the visual findings observed in Chapters 6.1.2 and 6.1.3.

In addition, the fuel injection temperature appears to be strongly negatively correlated with chamber pressure (as well as with total mass flow and curtain ratio, as a result of their interdependence). However, this linearity is not physically meaningful because it arises from the structure of the test campaign. Specifically, as the tests advanced toward higher chamber pressure load-points, the fuel injection temperature was intentionally lowered, introducing therefore an artificial correlation rather than any underlying causal mechanism.

Partial Correlation

Based on insights from the Pearson correlation matrix, two variables were excluded for the Partial correlation analysis. The total mass flow rate was removed because of its strong linear dependency with the curtain ratio, which introduced redundancy and reduced variable independence. Similarly, curtain $^{O}/_{F}$ was excluded as it did not contribute to any meaningful or physically interpretable information.

The Partial correlation matrix is shown in Figure 6.9. A perfect linear correlation is observed among core O/F, curtain ratio, and η_{c^*} resulting from the fact that all three variables are inherently defined based on the total mass flow rate formula. Since they share this common dependency, their inter-relationship becomes especially apparent when the influence of other variables is statistically controlled (such as through Partial correlation).

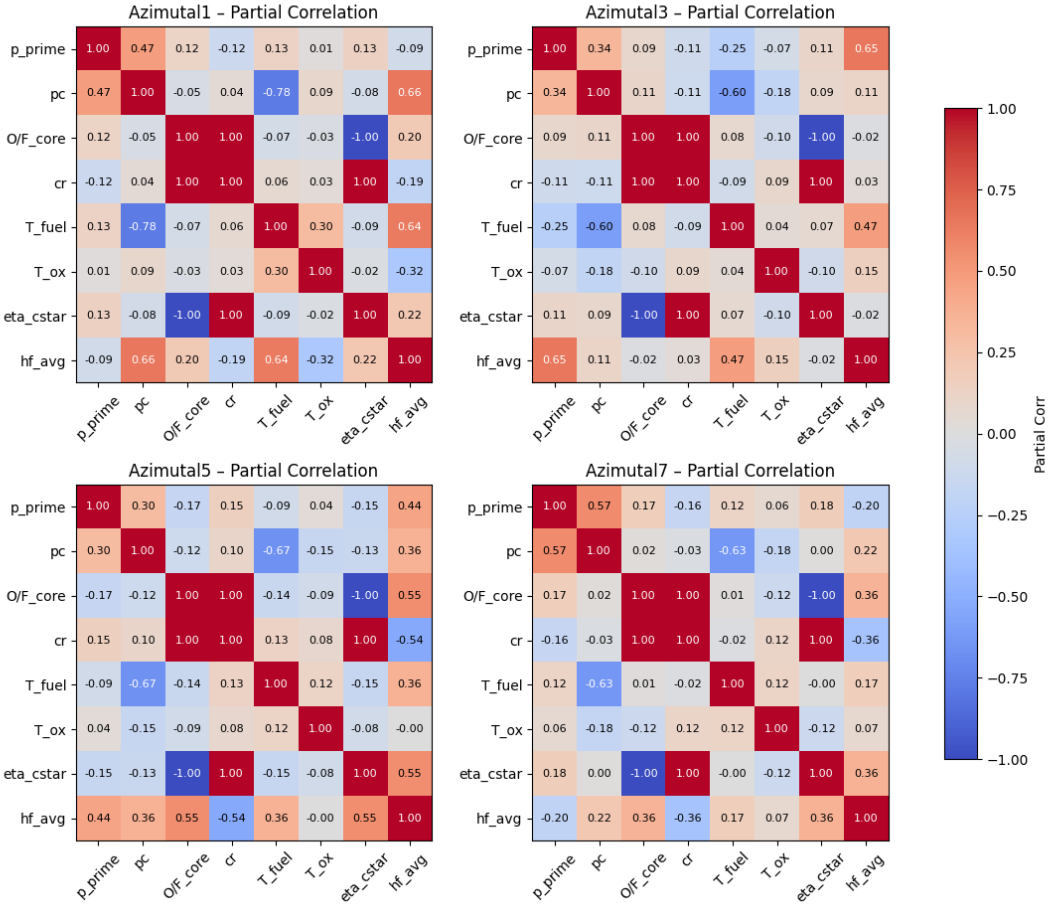

Figure 6.9: Partial correlation matrix

The partial correlation matrix indicates that the curtain ratio has a negative influence on heat flux, although we know from literature and previous results in the Chapter 6.1, that this relation is not strictly monotonic but rather convex. The positive influence of chamber pressure with heat flux, although visible at different magnitudes for the four azimuthal locations, is well supported by the Bartz correlation [15], which links convective coefficients to chamber pressure scaling.

Fuel injection temperature, which also shows a positive correlation with heat flux, does not show a clear visual trend in the corresponding 2D scatter plot (Figure D.8 in the Appendix D), but finds confirmation through a similarly positive Pearson coefficient and the underlying physics supporting this correlation. Elevated fuel injection temperatures improve the quality of vaporization and atomization, leading to more efficient mixing and combustion near the chamber wall, promoting a higher convective heat transfer near the chamber wall. Studies by Urbano and Nasuti [9], as well as Liang et al. [8], have highlighted how the thermal properties of hydrocarbons impact droplet breakdown and heat release dynamics under high-pressure conditions, validating the thermal sensitivity observed in the correlation matrices.

On the other hand, oxygen injection temperature does not seem to linearly affect much the wall heat flux in the Partial correlation, with coefficients of different sign at different azimuthal locations, and going in

contrast with what was observed with the Pearson correlation matrix. This supports the theory that the linear relation found earlier between oxygen injection temperature and heat flux might be an artifact correlations between multiple variables.

6.2.2. Variance Inflation Factor (VIF)

To further evaluate the presence of multicollinearity among the remaining parameters, a Variance Inflation Factor (VIF) analysis was conducted. While the Pearson and Partial correlation matrices show how strongly two variables are related to each other, the VIF tells how much a variable is influenced by a combination of all the other variables. If a variable can be well predicted using the others, its factor will be high, which means that it could cause problems in a regression model by making the results less stable. The common threshold for identifying moderate to high collinearity is when $VIF \geq 5$, which means that the variance of a coefficient is 5 times (or more) higher than it would be if the predictor was completely uncorrelated with others.

The resulting VIF values of the analyzed variables are presented in Figure 6.10.

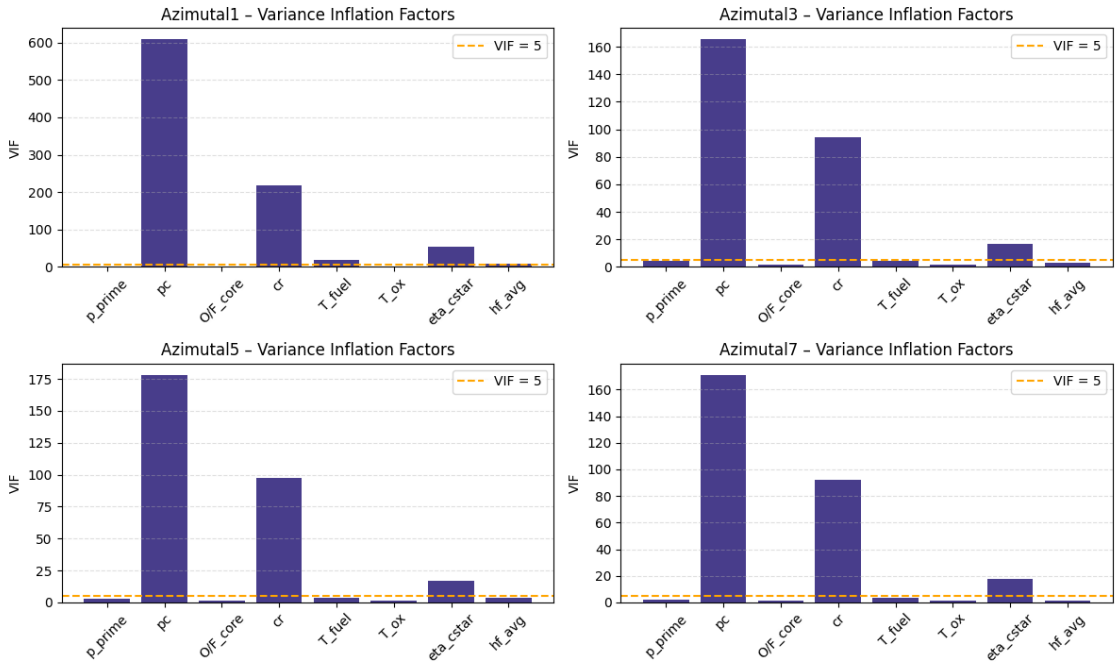

Figure 6.10: Variance inflation factor

The VIF plot shows a consistent similar trend at all four azimuthal locations. Among the variables examined, the chamber pressure consistently shows the highest VIF values, indicating that it is highly correlated with other predictors in the model.

As seen in previous test campaigns by Arnold [21] and Locke [58], chamber pressure responds sensitively to load-point configuration, often masking the individual influence of upstream variables when the test matrix is constrained.

The curtain ratio also emerges as a recurring contributor to multicollinearity, although not as extreme as the chamber pressure. This reinforces what previously found that curtain ratio is entangled with other parameters (such as chamber pressure and total mass flow rate). Lastly, combustion efficiency also manifests a relatively high VIF, probably due to its already observed relation with chamber pressure, shown in Chapter 6.1.4.

After recalculating the VIF by excluding curtain ratio and combustion efficiency, the remaining variables exhibit values well below the common threshold of VIF = 5 (apart from the chamber pressure outlier

in Azimuthal 1), as shown in Figure 6.11. This indicates that multicollinearity has been effectively mitigated, upon excluding curtain ratio and combustion efficiency, and that the selected variables are largely independent from one another, technically ready for the regression analysis.

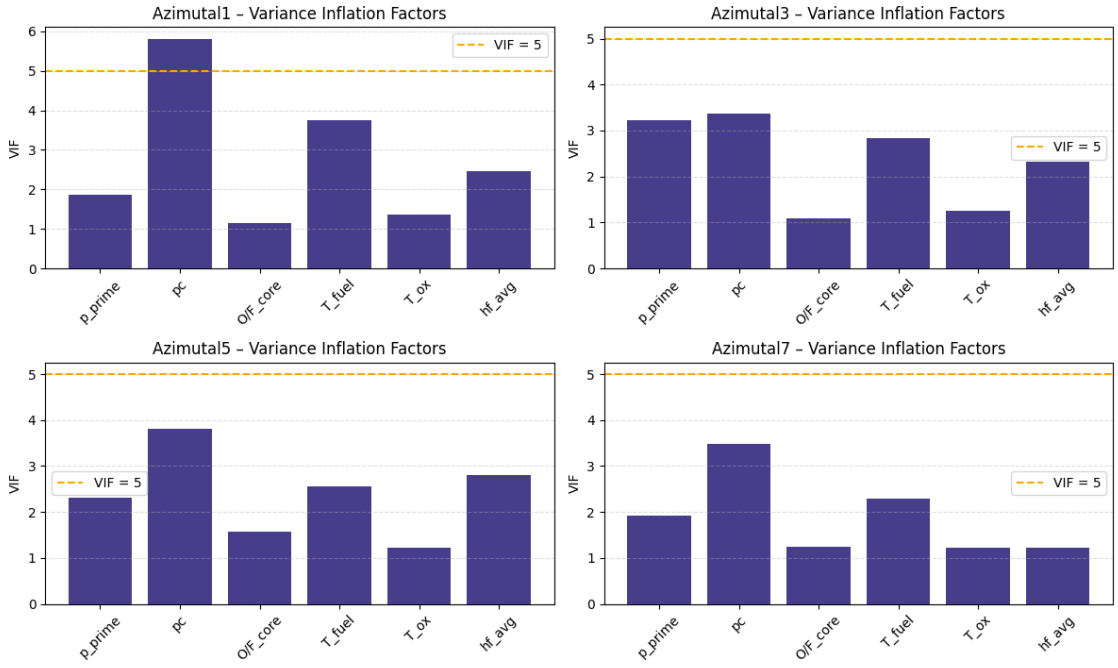

Figure 6.11: Variance inflation factor, excluding curtain ratio and η_{c^*}

6.2.3. Multiple Linear Regression (MLR)

Following the preliminary exploration of variable linear correlation through the Pearson correlation matrix and the assessment of multicollinearity through the Variance Inflation Factor (VIF), a refined set of predictors was identified for use in the MLR framework. These preliminary diagnostics highlighted strong dependencies among certain variables, resulting in the exclusion of total mass flow rate and curtain O/F due to their linear redundancy and lack of meaningful variance. Furthermore, combustion efficiency was set aside during the VIF analysis because it had shown elevated VIF values.

The curtain ratio, despite its statistical collinearity, was kept in the MLR formulation due to its obvious physical relevance. As analyzed in Chapter 6.1.3, the heat flux profiles at all azimuthal locations showed a marked sensitivity to variations in the curtain ratio, with a distinct local minimum. This behavior, although entangled with the chamber pressure, carries a meaningful interpretability that justifies the decision to include it in the prediction model. This approach compromises the statistical robustness of the model, but offers greater physical foundation. The regression coefficients for the selected variables, at all four azimuthal positions, are shown in Figure 6.12.

As expected, chamber pressure and curtain ratio emerge as the dominant drivers in the heat flux prediction model. Their respective positive and negative influences are only partially physically consistent, because the linear model fails to capture the non-linear behavior of the curtain ratio effect on heat flux, as previously observed in the literature of Chapter 3.2 and in the visual trend results of Chapter 6.1.3. The strong collinearity between chamber pressure and curtain ratio poses an additional limitation for the regression model, which can incur potential prediction instabilities, particularly when outside the tested range. The statistical weights assigned to these parameters must therefore be interpreted with care.

The core O/F and oxygen injection temperature exhibit a limited impact on the heat flux prediction model. In the case of the core mixture ratio, this is primarily due to the effective thermal shielding provided by the curtain film, which minimizes the direct influence of core combustion heat loads on wall heating.

Oxygen injection temperature, on the other hand, probably contributes less significantly because the oxidizer is injected through the inner curtain ring, placing it farther away in the film from the chamber wall, in comparison to propane. The latter, in fact, being injected through the outer film ring, is closer to the wall and has a more direct effect on the boundary layer cooling, thus playing a more prominent role in modulating local heat transfer, as shown by its moderate positive coefficient in the regression model.

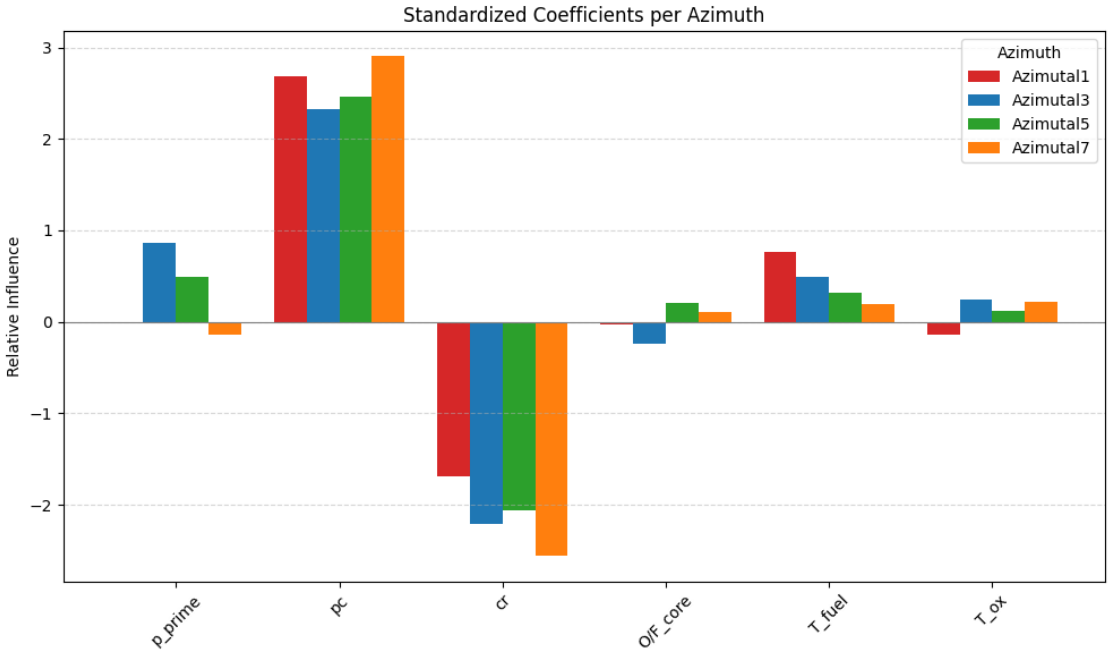

Figure 6.12: Multiple linear regression

Chamber pressure fluctuations exhibit inconsistent effects across azimuthal locations. The negative influence on heat flux observed in Azimuthal 7 (or the lack of contribution in Azimuthal 1) may be driven by a residual artifact from the model limitation, which aims to "balance out" residuals in the regression equation and non-linear behaviors.

Together, these results reaffirm the dominant role of chamber pressure and curtain ratio in driving wall heat flux, while suggesting a secondary influence of fuel injection temperature and pressure instabilities. It is important to note that this regression model was not developed with the goal of producing accurate heat flux predictions. Rather, it was used as a diagnostic tool to quantify the importance of key variables and to support the physical interpretation of their effects.

6.3. Key Findings Summary

The analyses conducted revealed several insights regarding the drivers of wall heat flux in the tested LOx/Propane single-element subscale combustor with reactive-film cooling:

1. Azimuthal Differences Confirm Local Film and Flow Asymmetries. The measured heat flux varied significantly across azimuthal planes, with consistent trends and up to 100% differences in extreme cases. These cannot be explained by measurement error alone (~6-7%), confirming physical causes. The asymmetry that results from the uneven film hole layout, in combination with a reactive curtain, affects heavily the local thermal shielding.
2. Chamber Pressure Instabilities Showed a Positive Trend. When plotting pressure fluctuations (p') against wall heat flux, higher levels of chamber instability tended to correspond to increased heat loads on the wall. This was most apparent during the visual analysis phase, particularly in Figures 6.2 and 6.3, while the regression model did not assign a consistent weight to (p') across azimuthals, possibly due to residual artifacts.

3. Chamber Pressure and Curtain Ratio as Dominant Drivers. Multiple linear regression highlighted the dominant roles of chamber pressure and curtain ratio in determining heat flux. This trend, which aligns with physical reasoning, was consistent across all azimuthal locations, with chamber pressure having the highest standardized coefficient in the linear model, as visible in Figure 6.12.
4. Curtain $^{O}/_{F}$ Ratio Exhibits Non-Linear Behavior with a Minimum. Despite its negative linear influence on the regression results, a more detailed visual inspection (Figure 6.4) revealed that the relationship between curtain ratio and heat flux was non-linear, showing a minimum at intermediate values. This suggests that while the film provides shielding, excessive curtain mass flow rate may lead to film entrainment with the core or film detachment, reducing its effectiveness.
5. Fuel Injection Temperature Has a Secondary Impact. The effect of fuel injection temperature emerged subtly but consistently throughout the statistical analysis. The Partial correlation results and the MLR model indicated a positive secondary influence of fuel temperature on heat flux. Although no clear trend was visible in the scatter plots, probably due to the underlying coupling between test logic and chamber pressure, this observation remains consistent with physical intuition.
6. Core $^{O}/_{F}$ Ratio and Oxygen Injection Temperature Have Minimal to No Influence. No meaningful correlation was found between core mixture ratio / oxygen injection temperature and heat flux results, either visually or statistically. This lack of sensitivity can be physically interpreted as a testament to the effectiveness of the curtain film, which acts as a thermal barrier between the hot core combustion and the chamber wall.
7. Collinearity Among Variables Limits. The statistical analysis highlighted several cases of multicollinearity, most notably between total mass flow, curtain ratio, and chamber pressure, as reflected in the Pearson matrix (Figure 6.8) and by high Variance Inflation Factors (Figure 6.10). These structural dependencies, which are the result of typical constraints in experimental setups, limited the ability of the regression model to assign independent physical meaning to the effect of each variable.

7

Conclusion

This master thesis aimed to answer the following research question:

"What are the dominant drivers of the wall heat flux in a single-element LOx/Propane subscale combustor with a hybrid capacitive and film-cooling system?"

By combining hot-fire experiments in a copper subscale chamber with inverse heat transfer reconstructions (RoqFITT) and a sensitivity analysis grounded in both visual interpretation and statistical modeling, the question has been fully addressed.

Two testing campaigns were conducted: the first to screen multiple coaxial injector designs and the second to systematically map operating parameters with a selected injector candidate. Temperature measurements obtained from 42 thermocouples embedded across four azimuthal planes allowed for high-resolution spatial and temporal heat-flux reconstructions. Using the RoqFITT solver, the transient conduction problem was solved for each test, yielding space-resolved profiles focused particularly on the throat region, where thermal loads are most critical. Thorough visual and sensitivity studies, focused on averaged intervals during steady chamber pressure, enabled quantification of how chamber pressure, film loading, mixture ratio, fuel and oxidizer injection temperatures and combustion instabilities affected the wall heat transfer.

The findings show that chamber pressure and film oxidizer-to-fuel ratio are the primary drivers of throat heat flux, exhibiting the strongest correlations and regression weights. Chamber pressure oscillations and fuel injection temperature play a secondary role, modulating local thermal loads through transient flow structures and combustion dynamics. In contrast, core mixture ratio and oxidizer injection temperature appear to have minimal influence on heat flux, supporting the notion that the curtain film layer effectively insulates the wall. Notably, the effect of curtain ratio revealed a non-linear trend, with a minimum in wall heat flux occurring at intermediate curtain ratios. In addition, the analysis revealed consistent azimuthal differences in wall heat flux, with variations ranging from 30% to 70% and in some cases reaching up to 100%, attributed to the asymmetric reactive-film hole layout.

This work addresses a critical gap in LOx/Propane heat transfer data, by offering insight into optimal film injection strategies, sensitivity scaling for regenerative cooling systems, and preliminary mapping for multi-element injector configurations. These trends provide a base for future design efforts towards the development of full-scale LOx/Propane rocket engines.

8

Outlook

Building on the insights gained from the single-element, capacitively and film cooled, subscale chamber used in this research, three principal development paths emerge:

1. **Regeneratively Cooled Subscale Chamber:** Proceed in the combustor design by designing a chamber with cooling channels, sized accordingly to the computed heat flux profiles. Then perform inverse and calorimetric heat transfer methods under new boundary conditions (of steady state), validating both the channel layout and the heat flux predictions obtained from the capacitive tests.
2. **Multi-Element Injector Scaling:** Continue in the combustor design by increasing the number of coaxial injectors and chamber size. This would enable the investigation of injector–injector interactions and their influence on combustion stability, flame anchoring, and local heat flux. It would also facilitate a comparison between single-element and multi-element configurations, allowing for an assessment of whether stability and thermal load trends can be extrapolated in both directions.
3. **Regeneratively Cooled Subscale Chamber + Multi-Element Injector Scaling:** A combination of options 1 and 2, which could lead to a faster iteration towards the full-scale chamber, but also enormously increase the uncertainties of proceeding towards the right direction.

Beyond these two main topics, other complementary studies are proposed to further optimize combustion performance:

- **Film-Injection Pattern Optimization:** Explore alternative film showerhead layouts (such as more distributed or staggered hole patterns) to homogenize the curtain layer and reduce heat flux hot spots.
- **Combustion Instabilities Mitigation:** Implement passive damping features, such as acoustic baffles or Helmholtz resonators, to suppress pressure oscillations and relative transient heat flux spikes.

Together, these next steps would help to close the loop between the single-element subscale design and a flight-ready, regeneratively cooled multi-element combustor, paving the way for robust, high-performance LOx/Propane propulsion systems.

References

[1] Gary Martin. *NewSpace: The Emerging Commercial Space Industry (NASA)*. https://ntrs.nasa.gov/api/citations/20170001766/downloads/20170001766.pdf. 2017.

[2] Yves Maisonneuve et al. "Green propellants perspectives for future missions". In: *44th AIAA/ASME/SAE/ASEE Joint Propulsion Conference & Exhibit*. 2008, p. 5028. DOI: 10.2514/6.2008-5028.

[3] Space News. *Isar Aerospace Spectrum rocket*. https://spacenews.com/wp-content/uploads/2019/12/hero-1.jpg. 2019.

[4] V. N. Dvornychenko. *The generalized Tsiolkovsky equation (NASA)*. https://ntrs.nasa.gov/api/citations/19910007786/downloads/19910007786.pdf. 1990.

[5] George P Sutton and Oscar Biblarz. *Rocket propulsion elements*. John Wiley & Sons, 2010.

[6] James A Martin. "Comparison of methane and propane rockets". In: *Journal of Spacecraft and Rockets* 23.6 (1986), pp. 658–658.

[7] Nikolaos Perakis. "Wall Heat Transfer Measurement and Prediction in Methane/Oxygen Rocket Engines". PhD thesis. Technische Universität München, 2021.

[8] Keming Liang, Baoe Yang, and Zhongli Zhang. "Investigation of heat transfer and coking characteristics of hydrocarbon fuels". In: *Journal of Propulsion and Power* 14.5 (1998), pp. 789–796. DOI: 10.2514/2.5342.

[9] Annafederica Urbano and Francesco Nasuti. "Parametric analysis of cooling properties of candidate expander-cycle fuels". In: *Journal of Propulsion and Power* 30.1 (2014), pp. 153–163. DOI: 10.2514/1.B34852.

[10] BA Younglove and James F Ely. "Thermophysical properties of fluids. II. Methane, ethane, propane, isobutane, and normal butane". In: *Journal of Physical and Chemical Reference Data* 16.4 (1987), pp. 577–798. DOI: 10.1063/1.555785.

[11] RS Gross. *Combustion performance and heat transfer characterization of LOX/hydrocarbon type propellants*. Tech. rep. 1980.

[12] Annafederica Urbano and Francesco Nasuti. "Conditions for the occurrence of heat transfer deterioration in light hydrocarbons flows". In: *International Journal of Heat and Mass Transfer* 65 (2013), pp. 599–609. DOI: 10.1016/j.ijheatmasstransfer.2013.06.038.

[13] Yigithan Mehmet Kose and Murat Celik. "Regenerative cooling comparison of lox/lch4 and lox/lc3h8 rocket engines using the one-dimensional regenerative cooling modelling tool odrec". In: *Applied Sciences* 14.1 (2023), p. 71. DOI: 10.3390/app14010071.

[14] Christoph Ulrich Kirchberger. "Investigation on heat transfer in small hydrocarbon rocket combustion chambers". PhD thesis. Technische Universität München, 2014.

[15] Donald R Bartz. "A simple equation for rapid estimation of rocket nozzle convective heat transfer coefficients". In: *Jet Propul.* 27 (1957), pp. 49–51. DOI: 10.2514/8.12572.

[16] DR Bartz. "Survey of the relationship between theory and experiment for convective heat transfer from rocket combustion gases". In: *Advances in Tactical Rocket Propulsion Conference Proceedings*. AGARD-CP-1. Advisory Group for Aerospace Research and Development (AGARD). 1968.

[17] M. Barrère et al. *Raketenantriebe*. Elsevier Publishing Company, 1961.

[18] A Schack. *Der industrielle Wärmeübergang,[Industrial heat transfer]*. Verlag Stahleisen, 1969.

[19] Ten-See Wang. "Multidimensional unstructured-grid liquid rocket-engine nozzle performance and heat transfer analysis". In: *Journal of Propulsion and Power* 22.1 (2006), pp. 78–84. DOI: 10.2514/1.14699.

[20] Florian Goebel et al. “Radiative heat transfer analysis in modern rocket combustion chambers”. In: *CEAS Space Journal* 6.2 (2014), pp. 79–98. DOI: 10.1007/s12567-014-0060-2.

[21] Richard Arnold. *Experimentelle Untersuchungen zur Filmkühlung in Raketenbrennkammern*. Cuvillier Verlag, 2008.

[22] RL Ewen and HM Evensen. *Liquid rocket engine self-cooled combustion chambers: NASA space vehicle design criteria (chemical propulsion)*. National Aeronautics and Space Administration, 1977.

[23] Volker Gnielinski. “New equations for heat and mass transfer in turbulent pipe and channel flow”. In: *International chemical engineering* 16.2 (1976), pp. 359–367.

[24] H Kraussold. “Die Wärmeübertragung an Flüssigkeiten in Rohren bei turbulenter Strömung”. In: *Forschung auf dem Gebiet des Ingenieurwesens A* 4.1 (1933), pp. 39–44.

[25] Richard Roback, EJ Szetela, and Louis J Spadaccini. *Deposit formation in hydrocarbon rocket fuels*. Tech. rep. 1981.

[26] R Wo Michel. *Combustion performance and heat transfer characterization of LOX/hydrocarbon type propellants*. Tech. rep. 1983.

[27] Marco Pizzarelli, Francesco Nasuti, and Marcello Onofri. “Analysis of curved-cooling-channel flow and heat transfer in rocket engines”. In: *Journal of Propulsion and Power* 27.5 (2011), pp. 1045–1053. DOI: 10.2514/1.B34163.

[28] Marco Pizzarelli et al. “Numerical analysis of three-dimensional flow of supercritical fluid in cooling channels”. In: *AIAA journal* 47.11 (2009), pp. 2534–2543. DOI: 10.2514/1.38542.

[29] Marco Pizzarelli, Francesco Nasuti, and Marcello Onofri. “Effect of cooling channel aspect ratio on rocket thermal behavior”. In: *Journal of Thermophysics and Heat Transfer* 28.3 (2014), pp. 410–416. DOI: 10.2514/1.T4299.

[30] Marco Pizzarelli. “The status of the research on the heat transfer deterioration in supercritical fluids: A review”. In: *International Communications in Heat and Mass Transfer* 95 (2018), pp. 132–138. DOI: 10.1016/j.icheatmasstransfer.2018.04.006.

[31] Marco Pizzarelli, Annafederica Urbano, and Francesco Nasuti. “Numerical analysis of deterioration in heat transfer to near-critical rocket propellants”. In: *Numerical Heat Transfer, Part A: Applications* 57.5 (2010), pp. 297–314. DOI: 10.1080/10407780903583016.

[32] Linda Hernandez et al. “The Effect of Surface Roughness on LCH4 Boiling Heat Transfer Performance of Conventionally and Additively Manufactured Rocket Engine Regenerative Cooling Channels”. In: *AIAA Propulsion and Energy 2019 Forum*. 2019, p. 4363. DOI: 10.2514/6.2019-4363.

[33] Thomas Fiala and Thomas Sattelmayer. “On the use of OH* radiation as a marker for the heat release rate in high-pressure hydrogen liquid rocket combustion”. In: *49th AIAA/ASME/SAE/ASEE Joint PropulsionConference*. 2013, p. 3780. DOI: 10.2514/6.2013-3780.

[34] Go Eun Choi, Young Joo Moon, and Changjin Lee. “Combustion dynamics in postchamber of hybrid rocket using CH* radical chemiluminescence images”. In: *Journal of Propulsion and Power* 33.1 (2017), pp. 176–186. DOI: 10.2514/1.B35999.

[35] Michael J Bedard et al. “Chemiluminescence as a diagnostic in studying combustion instability in a practical combustor”. In: *Combustion and Flame* 213 (2020), pp. 211–225. DOI: 10.1016/j.combustflame.2019.11.039.

[36] Frédéric Grisch, Paul Bouchardy, and Walter Clauss. “CARS thermometry in high pressure rocket combustors”. In: *Aerospace science and technology* 7.4 (2003), pp. 317–330. DOI: 10.1016/S1270-9638(03)00017-8.

[37] F Grisch et al. “CARS spectroscopy of CH4 for implication of temperature measurements in supercritical LOX/CH4 combustion”. In: *Aerospace science and technology* 11.1 (2007), pp. 48–54.

[38] M Necat Ozisik. *Inverse heat transfer: fundamentals and applications*. Routledge, 2018.

[39] Ralph L Schacht and Richard J Quentmeyer. *Axial and Circumferential Variations of Hot-gas-side Heat-transfer Rates in a Hydrogen-oxygen Rocket*. Vol. 6396. National Aeronautics and Space Administration, 1971.

[40] Detlef Kuhl, Oskar Haidn, and Andrea Holzer. "Computational solution of the inverse heat conduction problem of rocket combustion chambers". In: *35th Joint Propulsion Conference and Exhibit*. 1999, p. 2913. DOI: 10.2514/6.1999-2913.

[41] Dmitry Suslov, R Arnold, and O Haidn. "Investigation of film cooling efficiency in a high pressure subscale lox/h2 combustion chamber". In: *47th AIAA/ASME/SAE/ASEE Joint Propulsion Conference & Exhibit*. 2011, p. 5778. DOI: 10.2514/6.2011-5778.

[42] Maria P Celano et al. "Heat flux evaluation methods for a single element heat-sink chamber". In: *6th European Conference of Aeronautics and Space Science, Krakow, Poland*. 2015.

[43] Maria Palma Celano et al. "Comparison of single and multi-injector GOC/CH4 combustion chambers". In: *52nd AIAA/SAE/ASEE Joint Propulsion Conference*. 2016, p. 4990. DOI: 10.2514/6.2016-4990.

[44] Nikolaos Perakis, Maria Palma Celano, and Oskar J Haidn. "Heat flux and temperature evaluation in a rectangular multi-element GOX/GCH4 combustion chamber using an inverse heat conduction method". In: *7th European Conference for Aerospace Sciences*. 2017. DOI: 10.13009/EUCASS2017-366.

[45] Nikolaos Perakis and Oskar J Haidn. "Inverse heat transfer method applied to capacitively cooled rocket thrust chambers". In: *International Journal of Heat and Mass Transfer* 131 (2019), pp. 150–166. DOI: 10.1016/j.ijheatmasstransfer.2018.11.048.

[46] J. Strauß. *Heat Flux Calculation in Actively Cooled Rocket Thrust Chambers Using an Inverse Method*. Bachelor's Thesis. 2018.

[47] Nikolaos Perakis, Lukas Preis, and Oskar J Haidn. "Wall heat flux evaluation in regeneratively cooled rocket thrust chambers". In: *Journal of Thermophysics and Heat Transfer* 35.1 (2021), pp. 127–141. DOI: 10.2514/1.T6056.

[48] F. Longhetti. "Design and Experimental Evaluation of an Unlike Triplet Impinging Injector for a Sub-Scale Capacitive Combustion Chamber". WARR e.V. Semester Thesis. Technical University of Munich, 2022.

[49] William E Welsh Jr and Arvel B Witte. "A comparison of analytical and experimental local heat fluxes in liquid-propellant rocket thrust chambers". In: (1962). DOI: 10.1115/1.3684282.

[50] C Kirchberger, Gregor Schlieben, and Oskar J Haidn. "Investigation on Film Cooling in a GOX/Kerosene Rocket Combustion Chamber". In: *29th International Symposium on Space Technology and Science*. 2013.

[51] Gregor Schlieben et al. "Experimental and numerical film cooling investigations in a GOX/Kerosene rocket combustion chamber". In: *50th AIAA/ASME/SAE/ASEE Joint Propulsion Conference*. 2014, p. 4008. DOI: 10.1115/1.3684282.

[52] Simona Silvestri et al. "Characterization of a multi-injector gox/ch4 combustion chamber". In: *52nd AIAA/SAE/ASEE joint propulsion conference*. 2016, p. 4992. DOI: 10.1115/1.3684282.

[53] Simona Silvestri et al. "Experimental and numerical investigation of a multi-injector GOX-GCH4 combustion chamber". In: *Transactions of the Japan Society for Aeronautical and Space Sciences, Aerospace Technology Japan* 16.5 (2018), pp. 374–381. DOI: 10.1115/1.3684282.

[54] J. Conley, K. Tucker, and J. Schreiber. *Heat flux measurements in a LOx/CH_4 heat-sink combustion chamber using gradient-based techniques*. Technical Report. NASA Marshall Space Flight Center, 2007.

[55] Cosimo Ciraci. "Inverse heat conduction method and heat flux error estimation in rocket engines". PhD thesis. Politecnico di Torino, 2018.

[56] Dmitry Suslov et al. "Test specimen design and measurement technique for investigation of heat transfer processes in cooling channels of rocket engines under real thermal conditions". In: *39th AIAA/ASME/SAE/ASEE Joint Propulsion Conference and Exhibit*. 2003, p. 4613. DOI: 10.2514/6.2003-4613.

[57] Dmitry Suslov et al. "Measurement techniques for investigation of heat transfer processes at European Research and Technology Test Facility P8". In: (2005).

[58] Justin Locke, Sibtosh Pal, and Roger Woodward. "Chamber wall heat flux measurements for a LOX/CH4 propellant uni-element rocket". In: *43rd AIAA/ASME/SAE/ASEE Joint Propulsion Conference & Exhibit*. 2007, p. 5547. DOI: 10.2514/6.2007-5547.

[59] Lloyd Droppers, Reuben Schuff, and William Anderson. "Study of heat transfer in a gaseous hydrogen liquid oxygen multi-element combustor". In: *43rd AIAA/ASME/SAE/ASEE Joint Propulsion Conference & Exhibit*. 2007, p. 5550. DOI: 10.2514/6.2007-5550.

[60] GB Sinyarev and MV Dobrovol'skii. "Liquid Rocket Engines-Theory and Design". In: *Moscow, USSR* (1955).

[61] David T Harrje. *Liquid propellant rocket combustion instability*. Vol. 194. Scientific, Technical Information Office, National Aeronautics, and Space . . ., 1972.

[62] Riko Ueta et al. "Interaction of acoustic pressure and heat release rate fluctuations in a model rocket engine combustor". In: *Physical Review E* 110.1 (2024), p. 014202. DOI: 10.1103/PhysRevE.110.014202.

[63] Thomas Govaert et al. "Wall heat loads in a cryogenic rocket thrust chamber during thermoacoustic instabilities". In: *Journal of Propulsion and Power* 37.6 (2021), pp. 952–962. DOI: 10.2514/1.B38304.

[64] Richard Arnold, Dmitry I Suslov, and OJ Haidn. "Film cooling in a high-pressure subscale combustion chamber". In: *Journal of propulsion and power* 26.3 (2010), pp. 428–438. DOI: 10.2514/1.47148.

[65] RJ Burick. *Space storable propellant performance program coaxial injector characterization*. Tech. rep. 1972.

[66] HM Belal. "Numerical Simulation of Spray Combustion". PhD thesis. Military Technical College Cairo, Egypt, 2010.

[67] Nikolaos Perakis, Julian Strauß, and Oskar J Haidn. "Heat flux evaluation in a multi-element CH4/O2 rocket combustor using an inverse heat transfer method". In: *International Journal of Heat and Mass Transfer* 142 (2019), p. 118425. DOI: 10.1016/j.ijheatmasstransfer.2019.07.075.

[68] ANSYS Fluent et al. "Ansys fluent theory guide". In: *Ansys Inc., USA* 15317 (2011), pp. 724–746.

[69] Ning Guan et al. "Natural convection heat transfer on surfaces of copper micro-wires". In: *Heat and Mass Transfer* 50 (2014), pp. 275–284. DOI: 10.1007/s00231-013-1240-x. URL: https://link.springer.com/article/10.1007/s00231-013-1240-x.

[70] M. Giglmaier. *Vorlesung Angewandte CFD, Grundlagen der Gittergenerierung*. Lecture notes, Technical University of Munich. 2018.

[71] Roger Fletcher. *Practical methods of optimization*. John Wiley & Sons, 2013.

[72] Richard Arnold, Dmitry Suslov, and OJ Haidn. "Circumferential film cooling effectiveness in a LOX/H2 subscale combustion chamber". In: *Journal of propulsion and power* 25.3 (2009), pp. 760–770. DOI: 10.2514/1.40305.

A

Hot-fire Sequence

Here are listed the most important section of the hot-fire sequence, step by step:

Pre-ignition:

- ON GN2 igniter purge: the torch igniter is purged with GN2 on both GOX and GCH4 lines before ignition
- ON LN2 on fuel (core & curtain) side: LN2 is used to chill the fuel injector manifold and to purge the lines before ignition. The purging process on the fuel line is essential to avoid LOx back-flow into the fuel manifold, upon LOx injection
- LOx & PP tanks pressurization ramp: propellant tanks are pressurized in ramps to the desired set pressure
- ON LOx (core & curtain): LOx is injected in the chamber from both core and curtain sides, to chill the oxidizer injector manifold and to purge the run lines
- OFF LOx (core) & ON LN2 on oxidizer (core) side: the LOx flow through the core is replaced with a LN2 purge overlap, to maintain the curtain $^{O}/_{F}$ upon curtain ignition stage. The flow in the core section is kept (with LN2) to avoid re-circulation (and consequent disruption) of the curtain film with an "empty zone"

Ignition:

- OFF GN2 igniter purge & ON torch igniter: the purge through the igniter is stopped and the propellant mixture GOX/GCH4 is ignited through a spark
- ON PP drain valves (core & curtain): propane flows in the fuel core and curtain lines through the drain valves, to chill the lines until the run valves; it is then burnt into the burn-pit
- OFF PP drain valve (curtain), OFF LN2 on fuel (curtain), ON PP (curtain): the drain valve and the LN2 purge on the fuel curtain line are closed. The run valve of the fuel curtain is opened, and PP is injected from the fuel curtain manifold into the chamber → **curtain ignition**
- OFF PP drain valve (core), OFF LN2 on fuel (core) & on oxidizer (core), ON LOx (core) & ON PP (core): the drain valve on the fuel core is closed as well as the LN2 purge on the oxidizer and fuel core. LOx and PP run valves are opened and both propellants flow into the chamber from the core manifolds → **core + curtain ignition**

Hot-fire:

- OFF torch igniter & ON GN2 igniter purge: when the core is ignited, the torch igniter is switched off and the igniter propellant lines are purged with nitrogen (to both clean the lines and avoid back-flow)

Shutdown:

- OFF LOx (core & curtain) & ON GN2 on oxidizer (core & curtain) side: LOx core and curtain run valves are closed, to achieve a fuel-rich shutdown. GN2 is injected in the oxidizer manifolds with a purge overlap, to avoid backflow
- OFF PP (core & curtain): once the chamber pressure has decayed, PP run valves of core and curtain are closed. For safety reasons, the consequent step of GN2 fuel purge is kept on hold for a short time, to be sure that the propane combustion is completely over
- ON GN2 on fuel (core & curtain) side: the remaining PP in the fuel injector manifold is purged out with GN2
- LOx & PP tanks de-pressurization: both propellant tanks are de-pressurized
- ON (LOx & PP) drain valves & ON GN2 fuel and oxidizer (curtain & core) purge: the LOx and PP drain valves are opened and the propellants on the lines are dumped with GN2 (LOx into ambient, PP into the burn-pit)
- OFF GN2 on all lines: all GN2 purges are stopped, as the test is over and the TA / test-rig lines are cleaned

In addition, redlines were used in the sequence to stop the test in case some parameters were off nominal, with the aim of minimizing risks (or mitigate, if too late) dangerous scenarios. Among them:

- Run tanks pressure check → in case pressure is too low, tank pressurization failed
- Injector head temperatures → in case were too high, outside of load point boundaries
- Ignition pressure check → if chamber pressure too low (no ignition achieved), to avoid potential unburnt combustible mixture
- Curtain hot-fire pressure check → if chamber pressure was too low, to avoid potential unburnt combustible mixture.

B

Test Matrix

Test Matrix of both Test Campaigns, with normalized values, colour coded by column to highlight differences within the same variable of different tests.

Test	ID	mf_total	pc	p_prime	T_fuel	T_ox	cr	O/F_curt	O/F_core	d_th	eta_cstar
0618_0	C1	1,225	0,850	3,983	1,058	1,037	1,092	0,500	0,971	1,093	0,846
0621_0	C8	1,206	0,826	3,360	1,070	1,022	1,088	0,494	0,994	1,093	0,859
0628_0	P1A	1,213	0,837	0,733	1,085	1,028	1,104	0,502	0,969	1,093	0,882
0628_1	P1A	1,195	0,901	1,410	1,354	1,010	1,057	0,602	0,956	1,093	0,955
0927_0	P1A	1,216	1,017	0,593	1,215	1,059	1,097	0,480	0,980	1,000	0,893
0928_0	P1A	1,216	1,074	1,977	1,205	1,057	1,077	0,513	0,956	1,000	0,943
0930_0	P1B	1,200	1,075	4,097	1,006	1,074	1,082	0,485	0,980	1,000	0,955
1001_0	P1D	1,213	1,064	1,967	0,937	1,054	1,094	0,510	0,980	1,000	0,935
1001_1	P1D	1,242	1,172	0,567	1,046	0,980	1,055	0,582	1,057	1,000	0,992
1004_0	P1D	1,185	1,047	0,583	0,961	1,036	1,077	0,588	0,924	1,000	0,944
1004_1	P1D	1,189	1,028	2,140	0,933	1,029	1,082	0,585	0,924	1,000	0,924
1005_0	P1I	1,145	1,010	0,610	0,939	1,014	1,119	0,585	1,029	1,000	0,933
1006_2	P1I	0,897	0,869	0,930	1,034	0,964	0,841	1,020	1,061	1,000	1,026
1012_0	P1I	0,884	0,855	1,527	1,003	1,041	0,840	0,963	0,960	1,000	1,016
1012_1	P1I	0,913	0,888	1,157	0,996	1,006	0,826	0,988	1,042	1,000	1,028
1013_0	P1I	0,885	0,859	0,993	1,035	1,003	0,835	1,001	0,894	1,000	1,019
1013_1	P1I	0,889	0,881	1,077	1,059	0,990	0,828	0,995	0,905	1,000	1,040
1018_0	P1I	0,970	0,962	1,093	1,024	1,046	0,926	0,975	1,023	1,000	1,043
1018_1	P1I	1,000	0,998	1,073	0,951	0,974	0,912	1,028	1,078	1,000	1,055
1019_0	P1I	0,963	0,959	1,053	0,999	1,007	0,935	1,006	0,905	1,000	1,044
1019_1	P1I	0,982	0,970	1,040	0,944	0,979	0,929	1,028	0,910	1,000	1,037
1026_0	P1I	1,118	1,141	1,610	0,981	0,986	1,056	0,953	1,044	1,000	1,070
1027_0	P1I	1,105	1,112	1,877	0,921	0,986	1,058	0,998	0,950	1,000	1,055
1027_1	P1I	1,104	1,113	2,177	0,950	0,975	1,057	1,006	0,950	1,000	1,058
1027_4	P1I	1,097	1,119	3,693	0,965	0,977	1,050	0,995	1,054	1,000	1,070

C

Heat Flux Evaluations

C.1. First Test Campaign

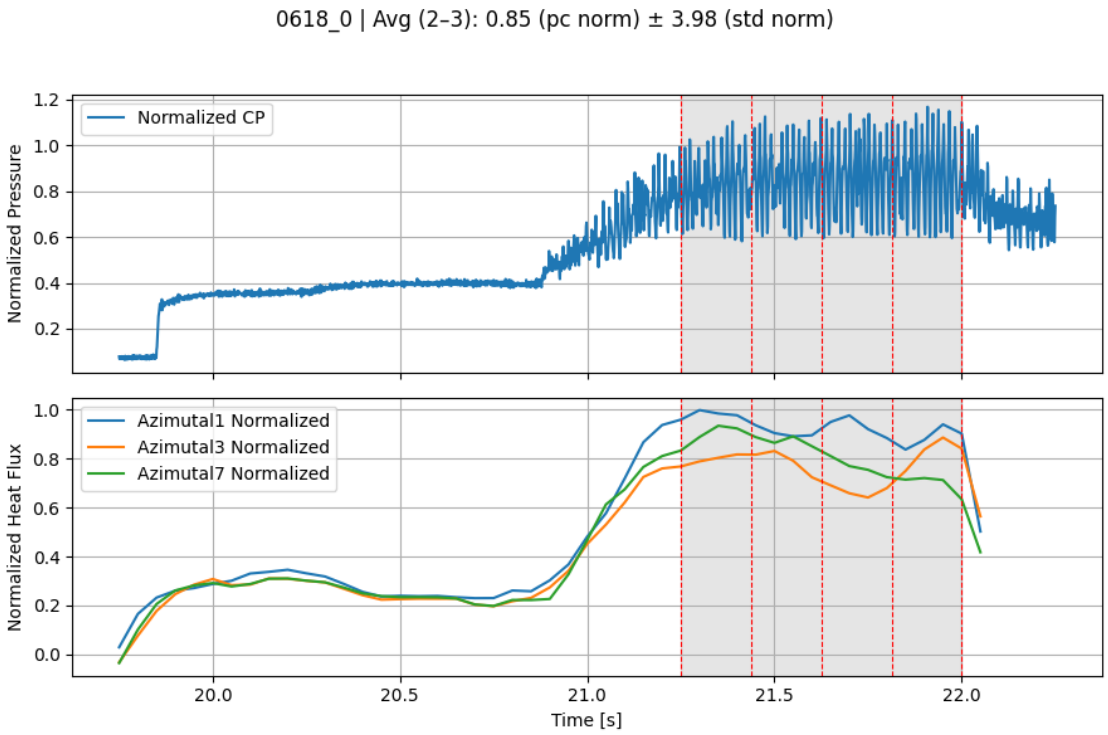

Figure C.1: Test 0618_0

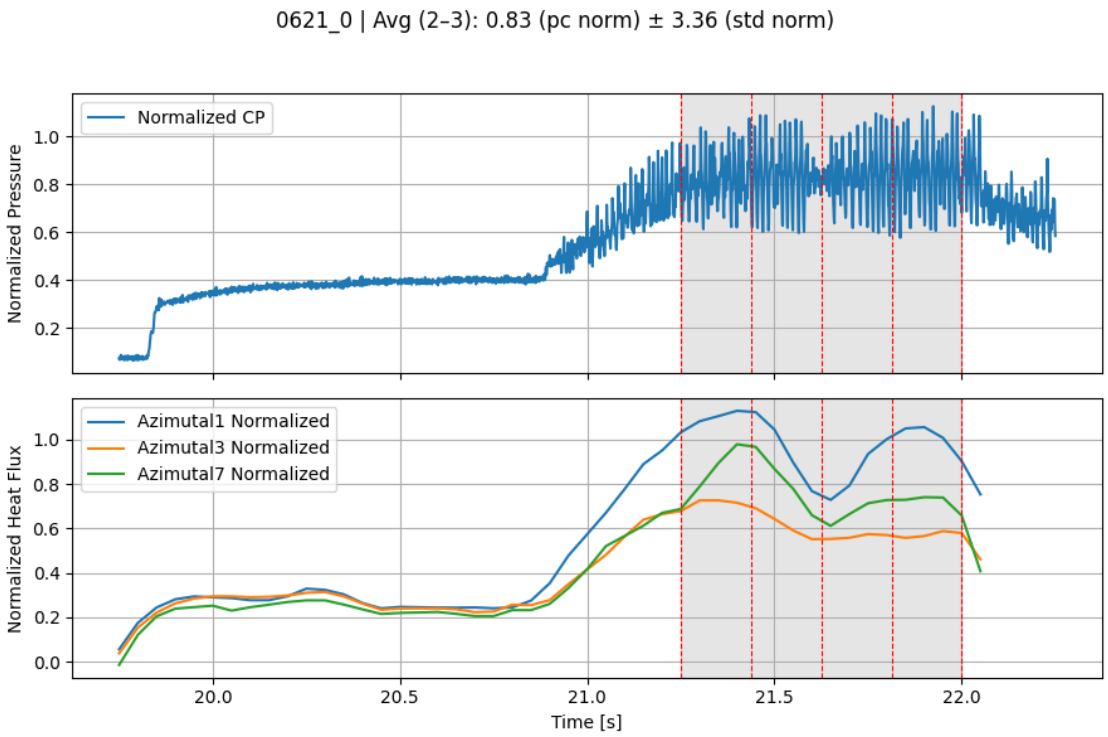

Figure C.2: Test 0621_0

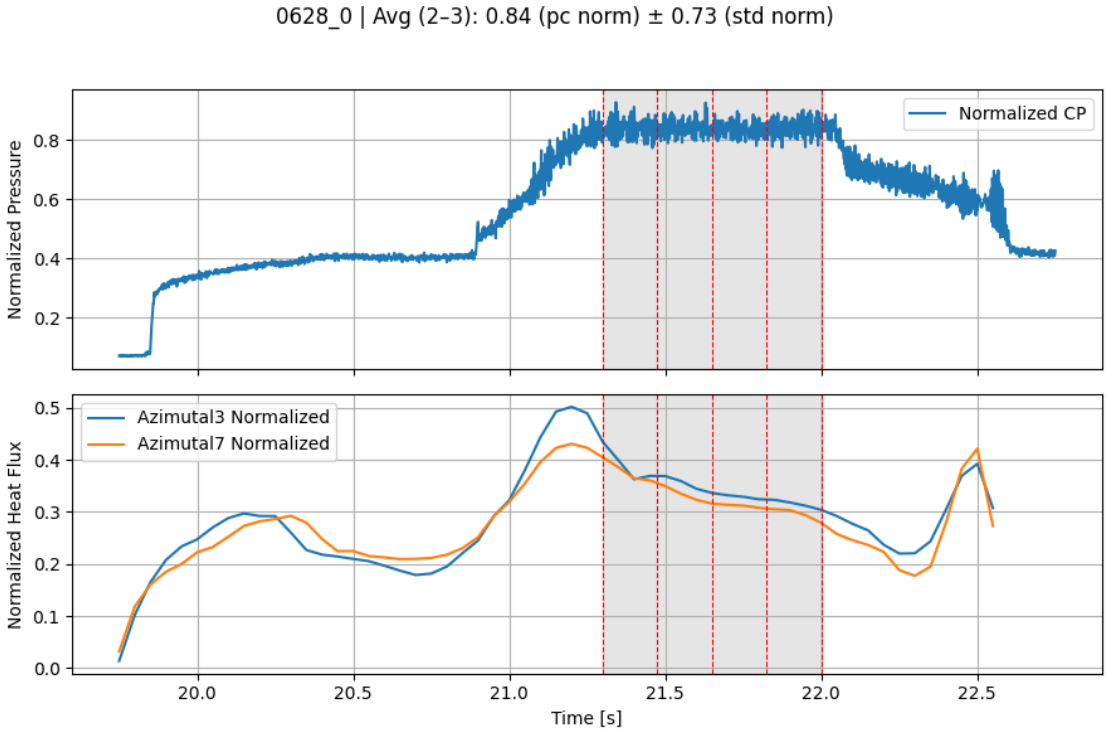

Figure C.3: Test 0628_0

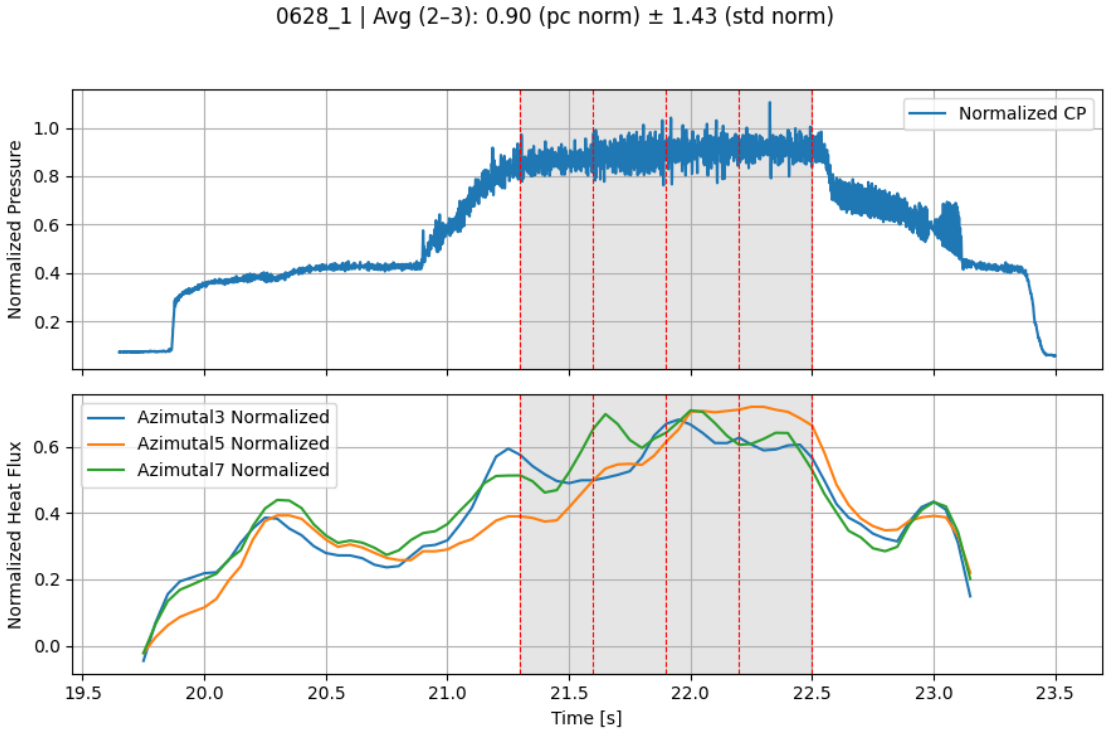

Figure C.4: Test Test 0628_0

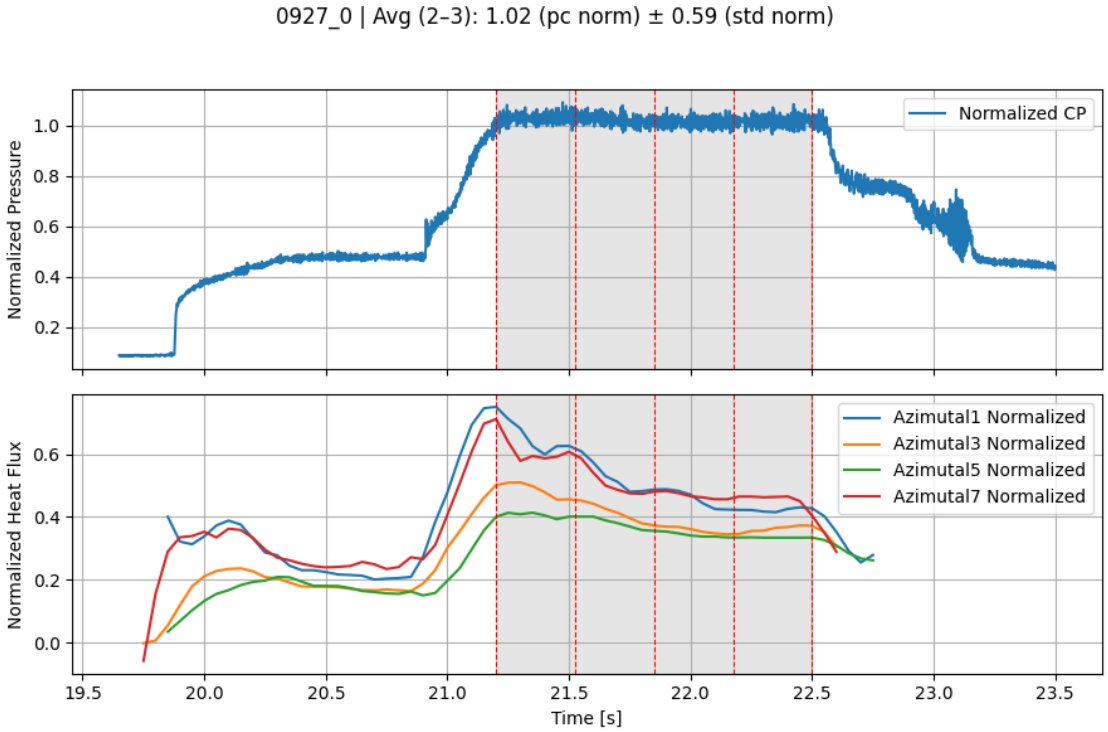

Figure C.5: Test 0927_0

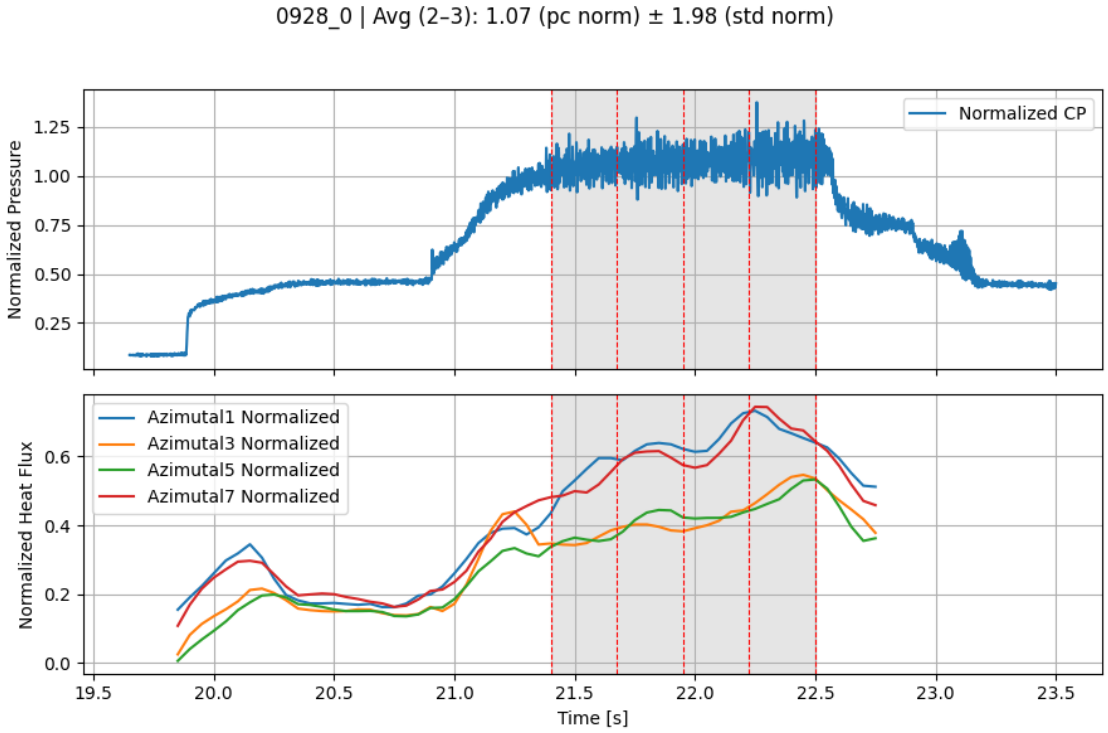

Figure C.6: Test 0928_0

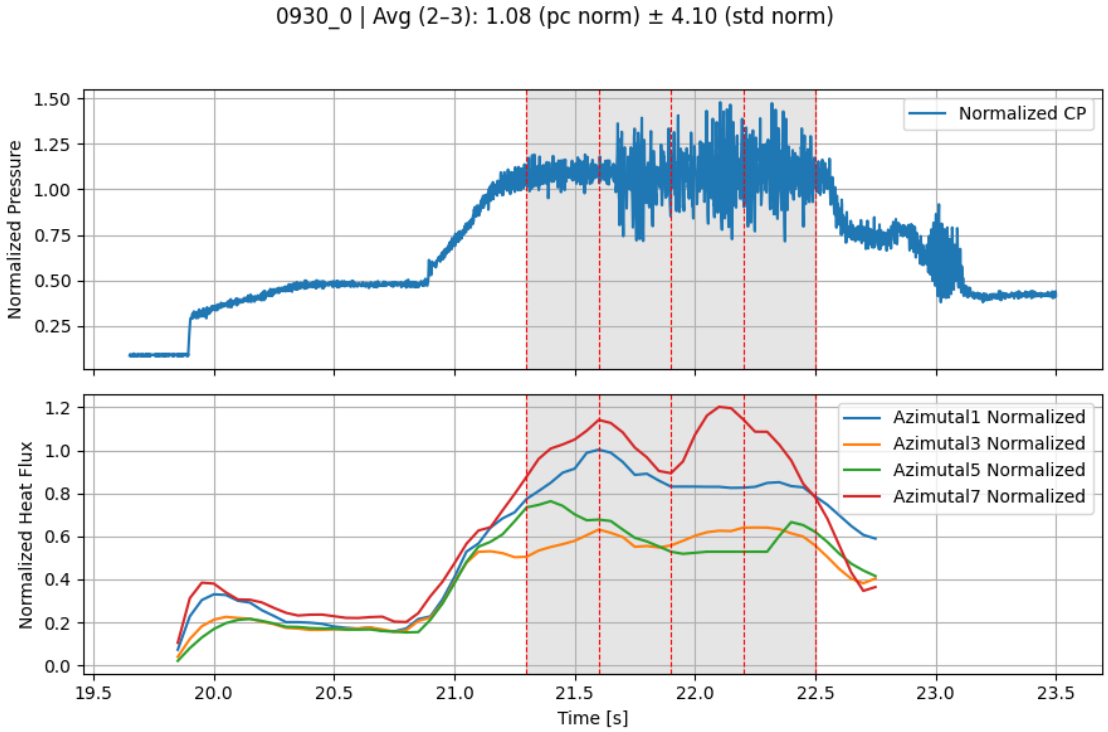

Figure C.7: Test 0930_0

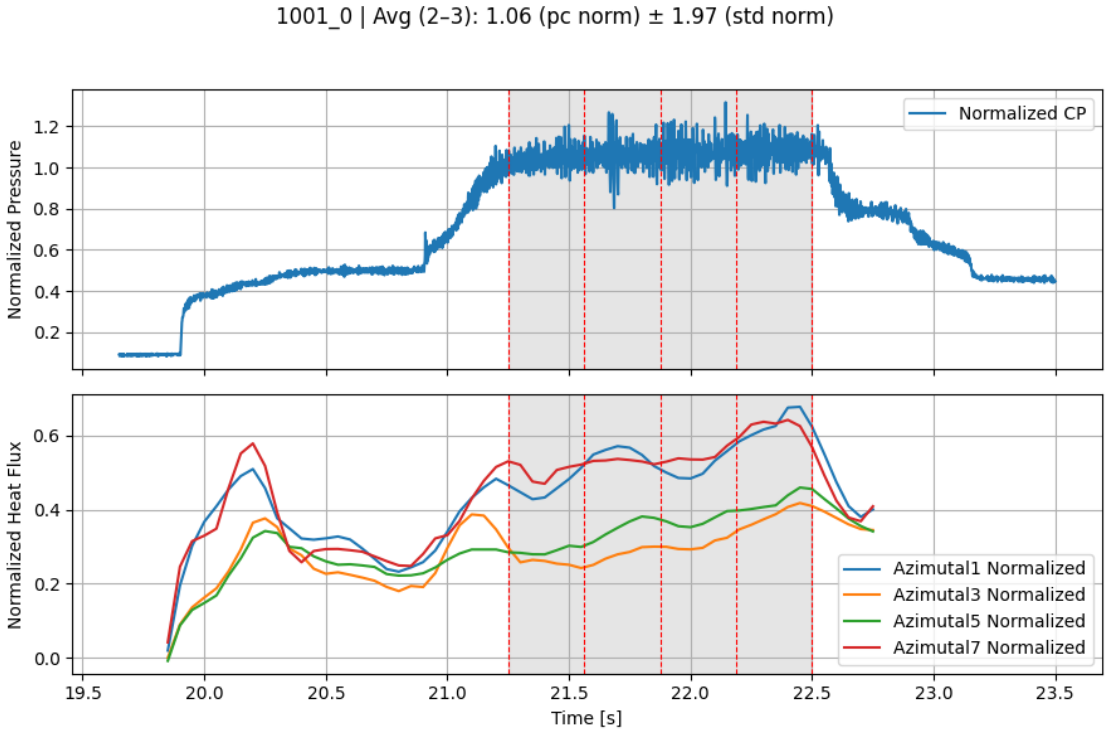

Figure C.8: Test 1001_0

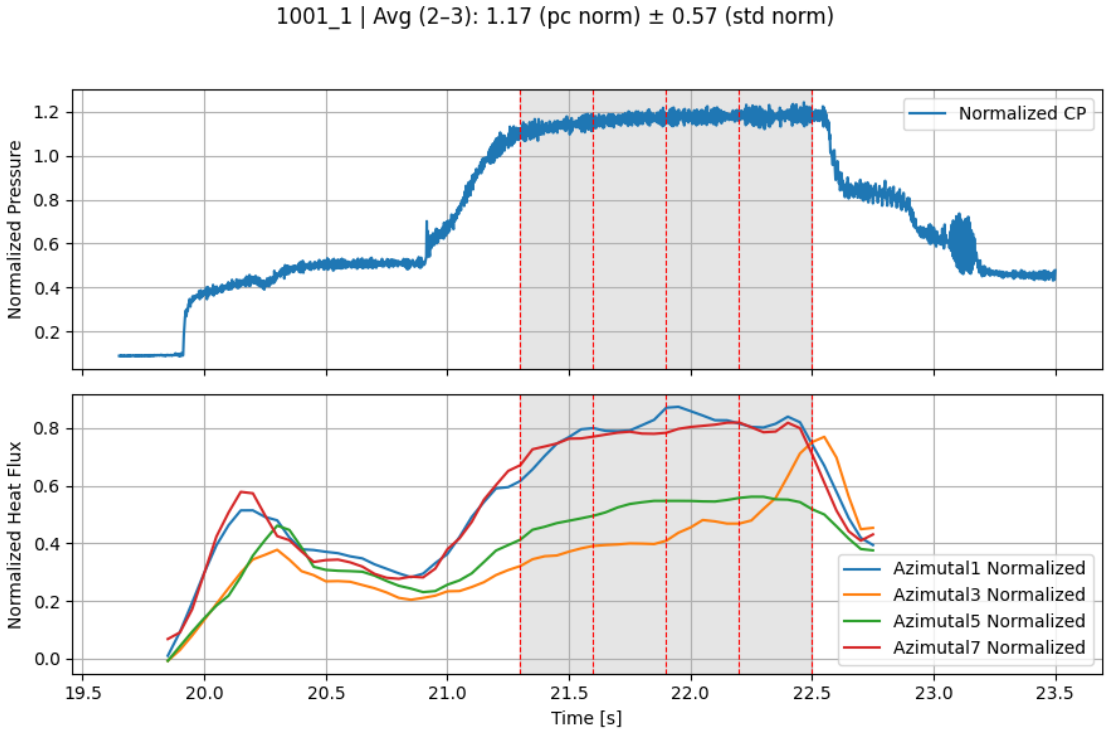

Figure C.9: Test 1001_0

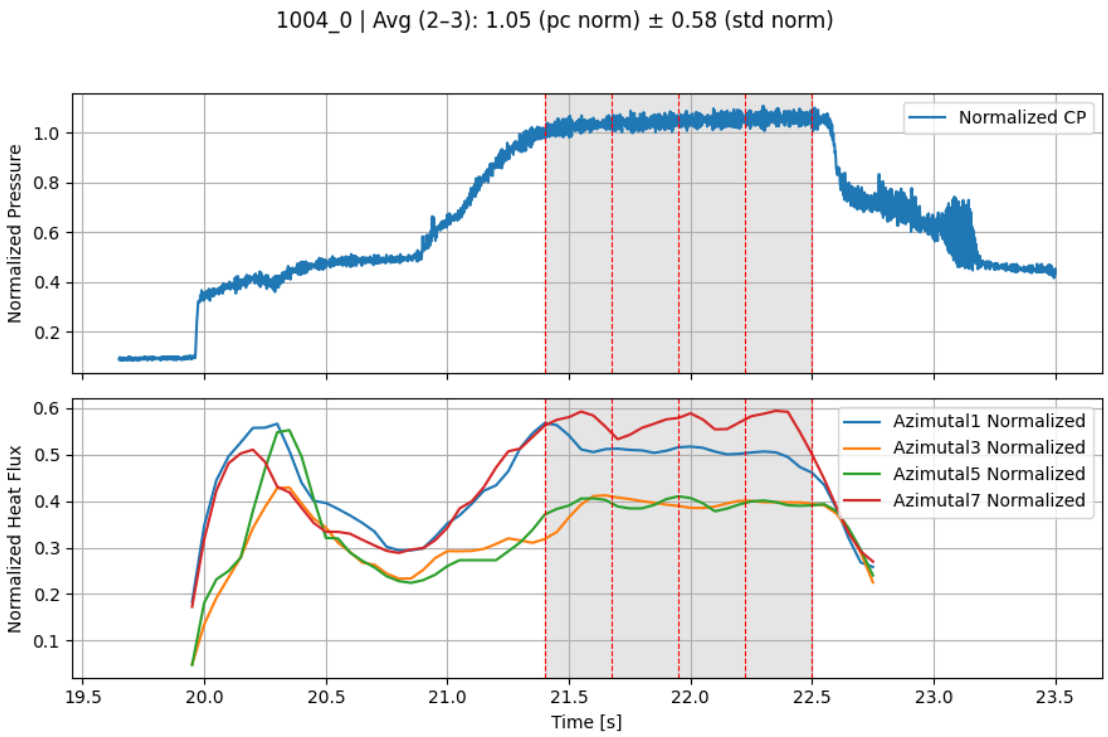

Figure C.10: Test 1004_0

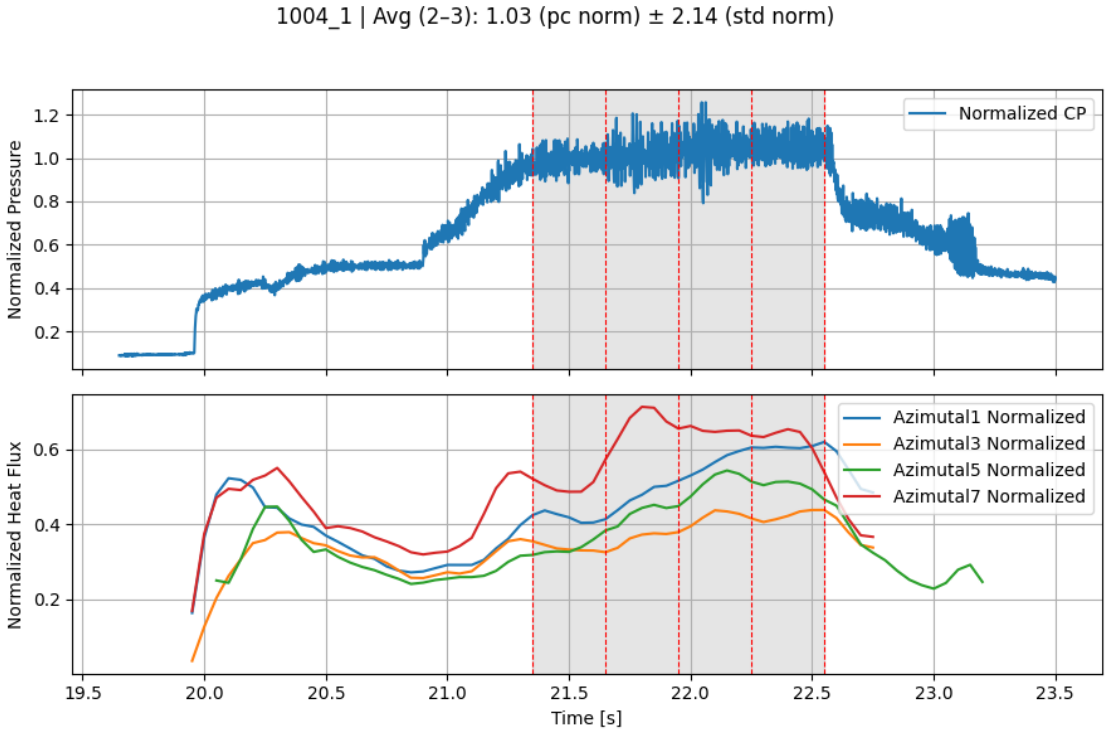

Figure C.11: Test 1004_0

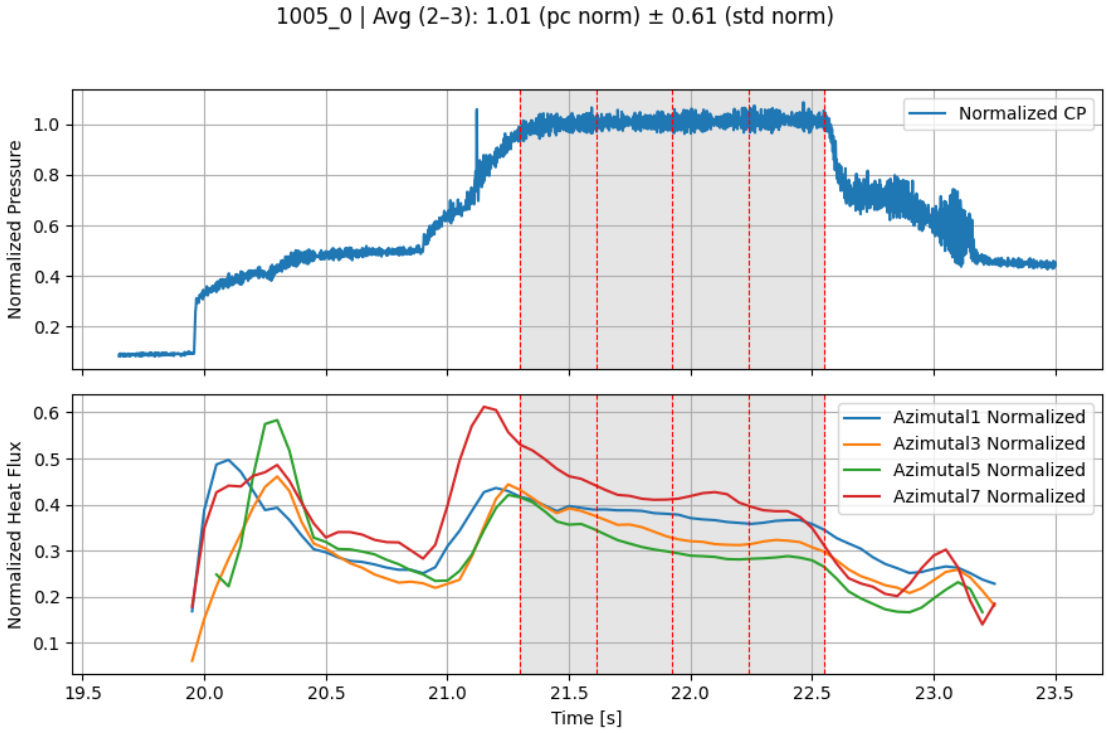

Figure C.12: Test 1005_0

C.2. Second Test Campaign:

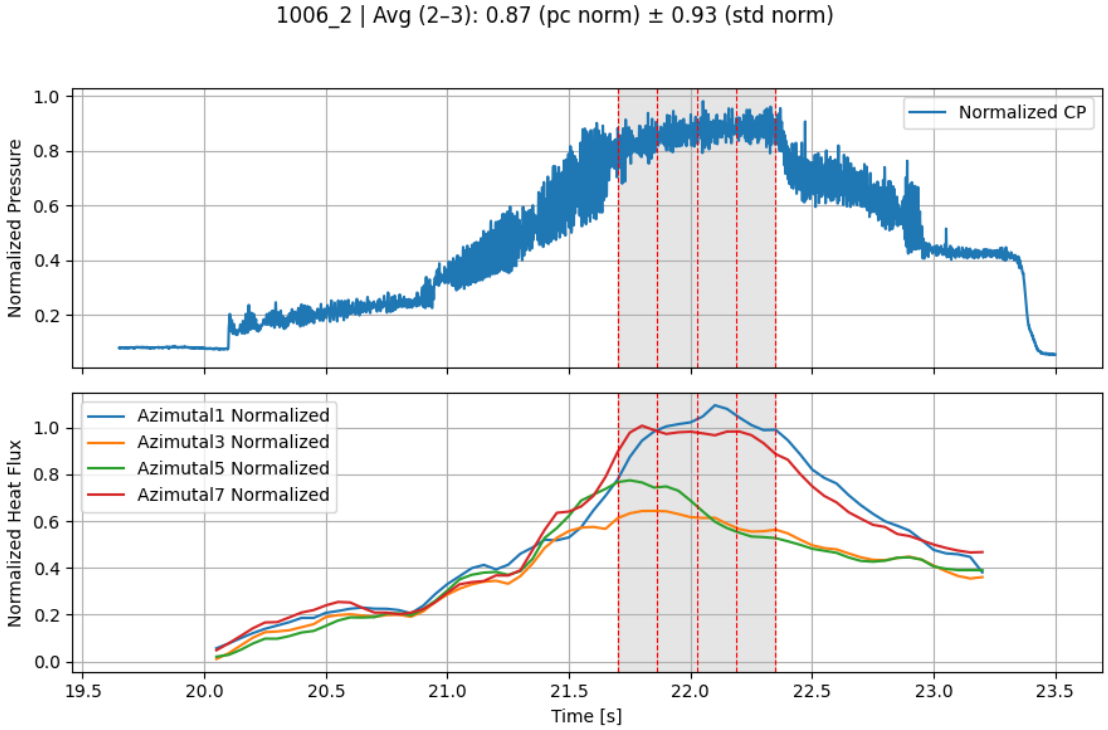

Figure C.13: Test 1006_2

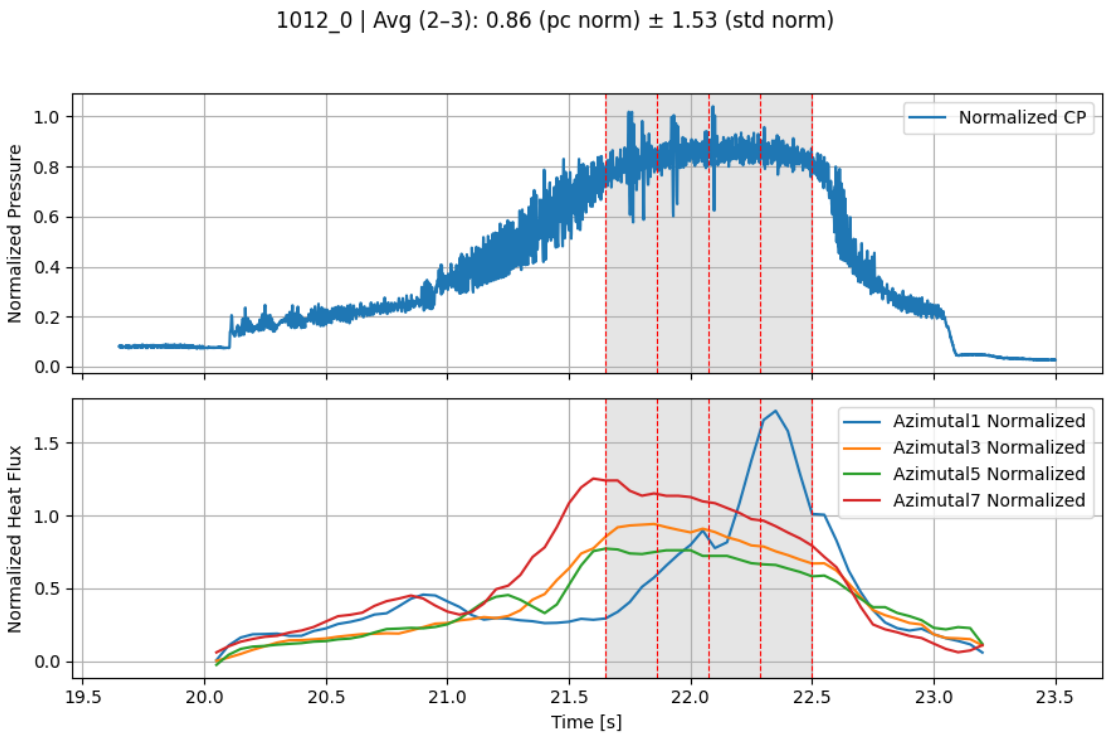

Figure C.14: Test 1012_0

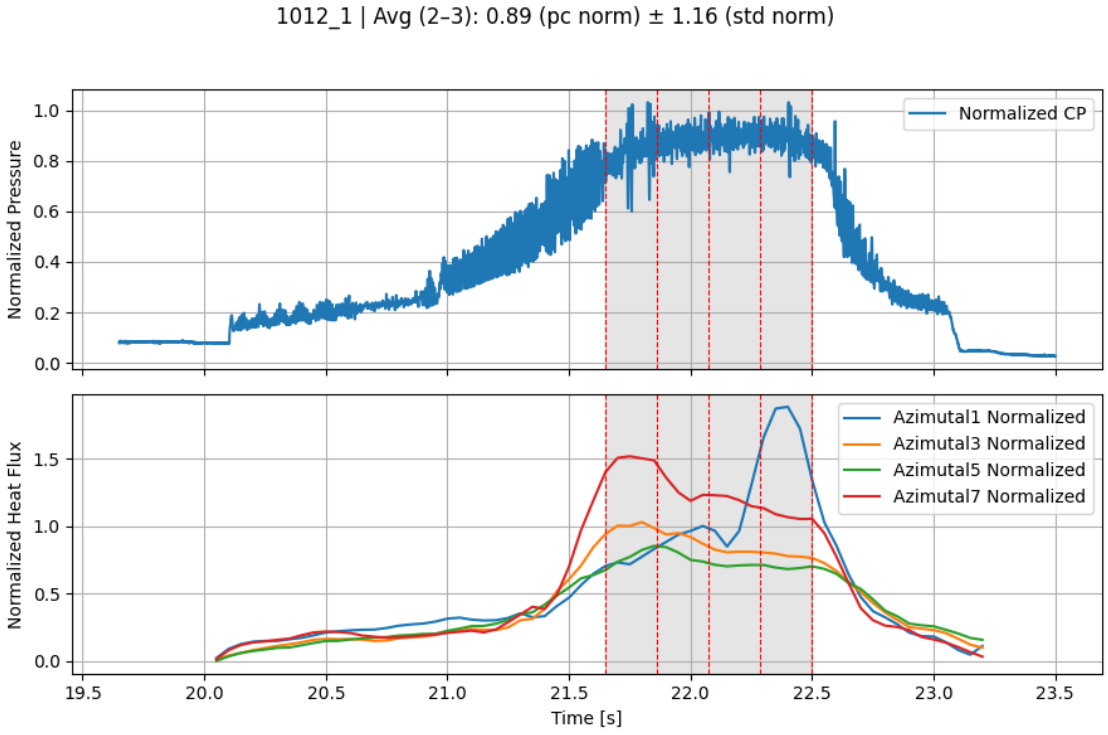

Figure C.15: Test 1012_1

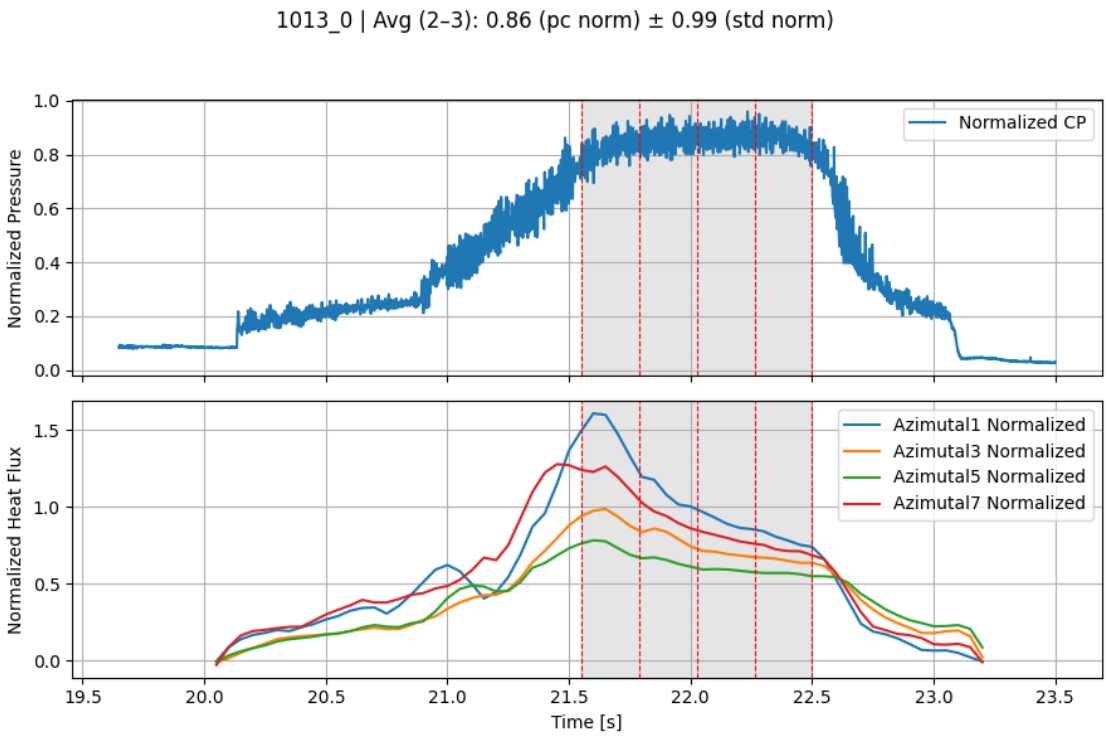

Figure C.16: Test 1013_0

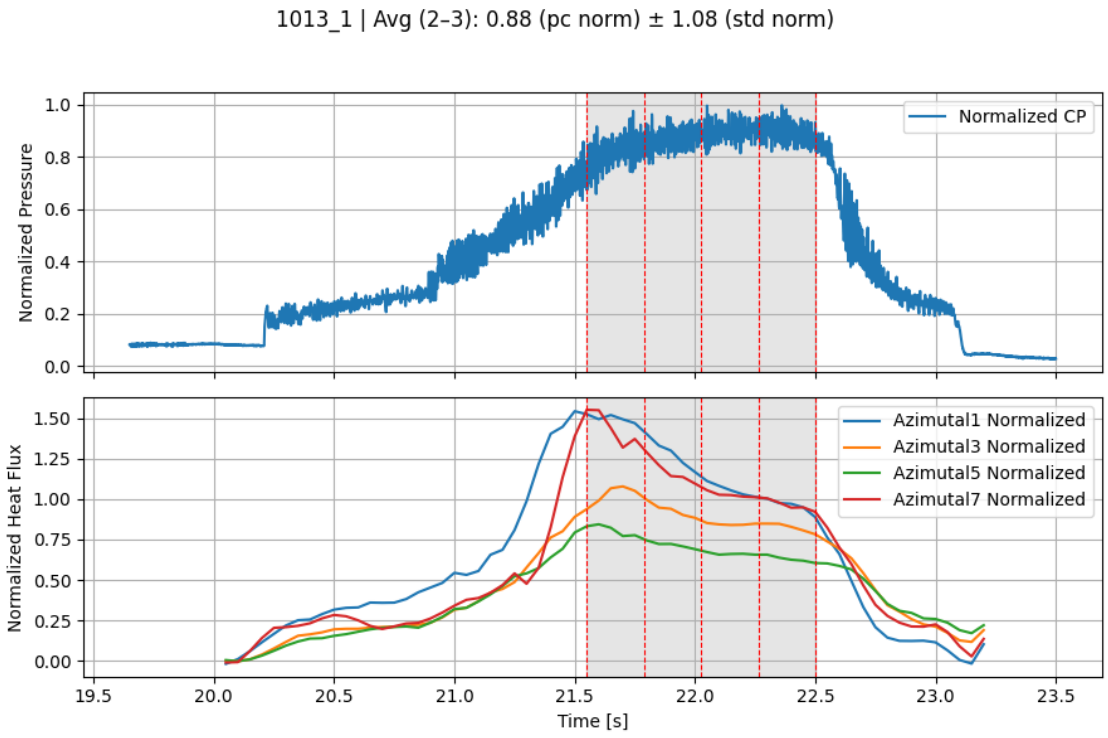

Figure C.17: Test 1013_1

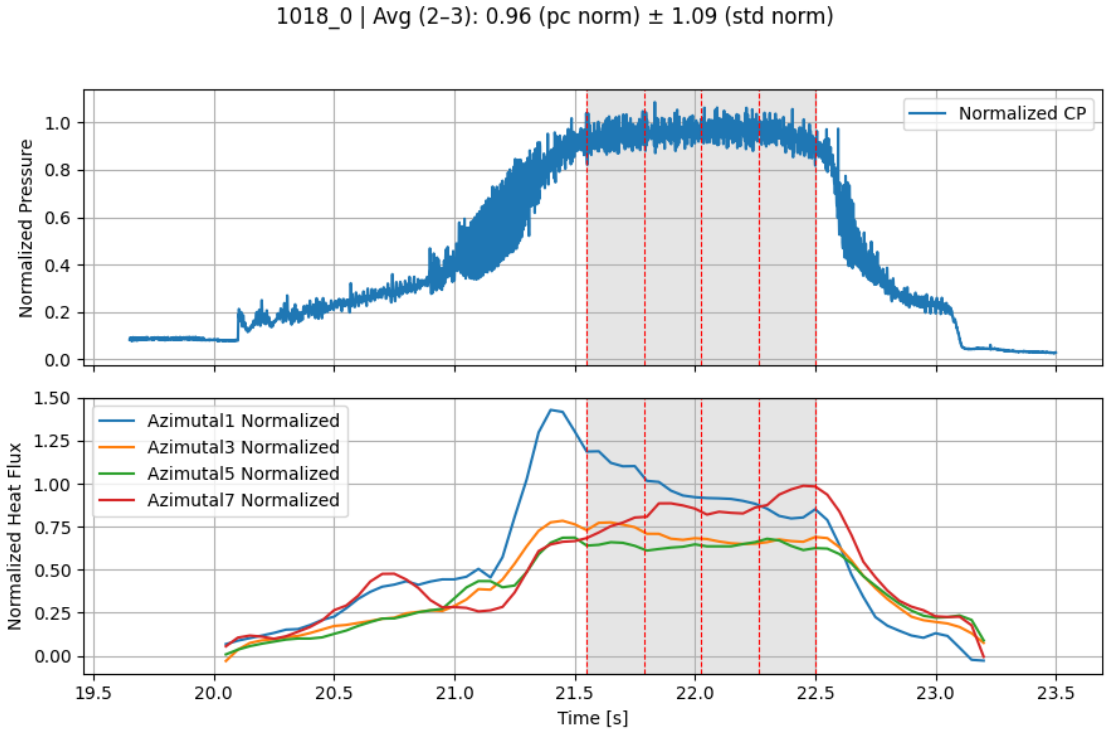

Figure C.18: Test 1018_0

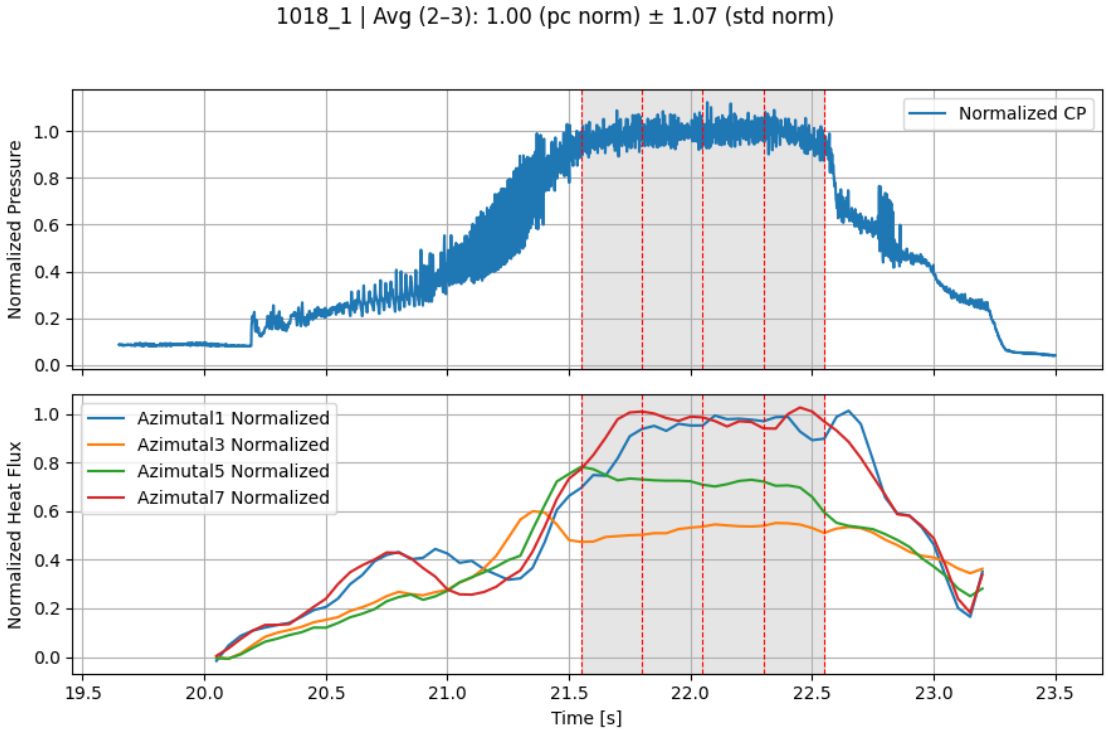

Figure C.19: Test 1018_1

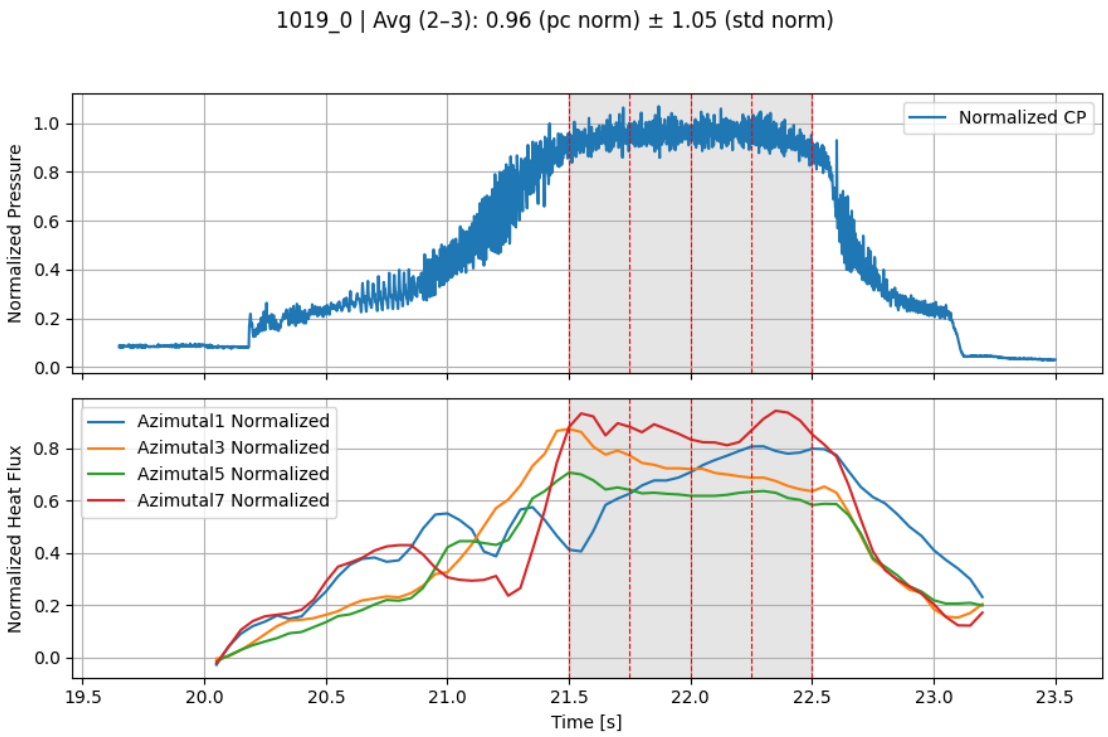

Figure C.20: Test 1019_0

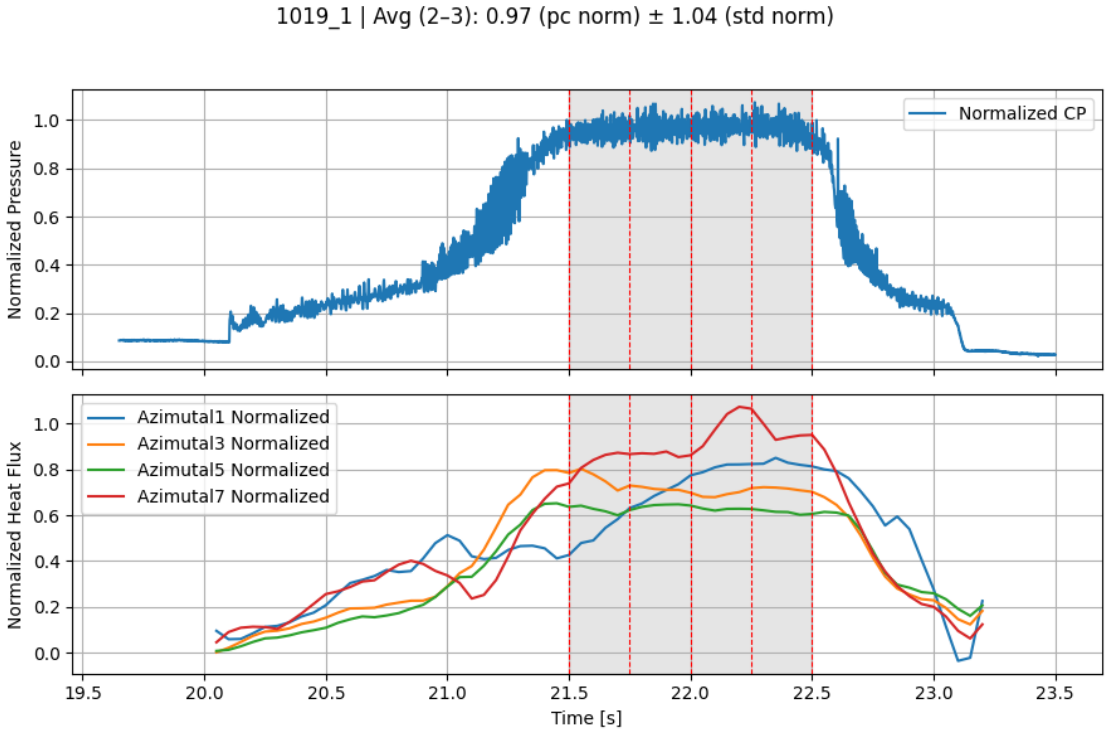

Figure C.21: Test 1019_1

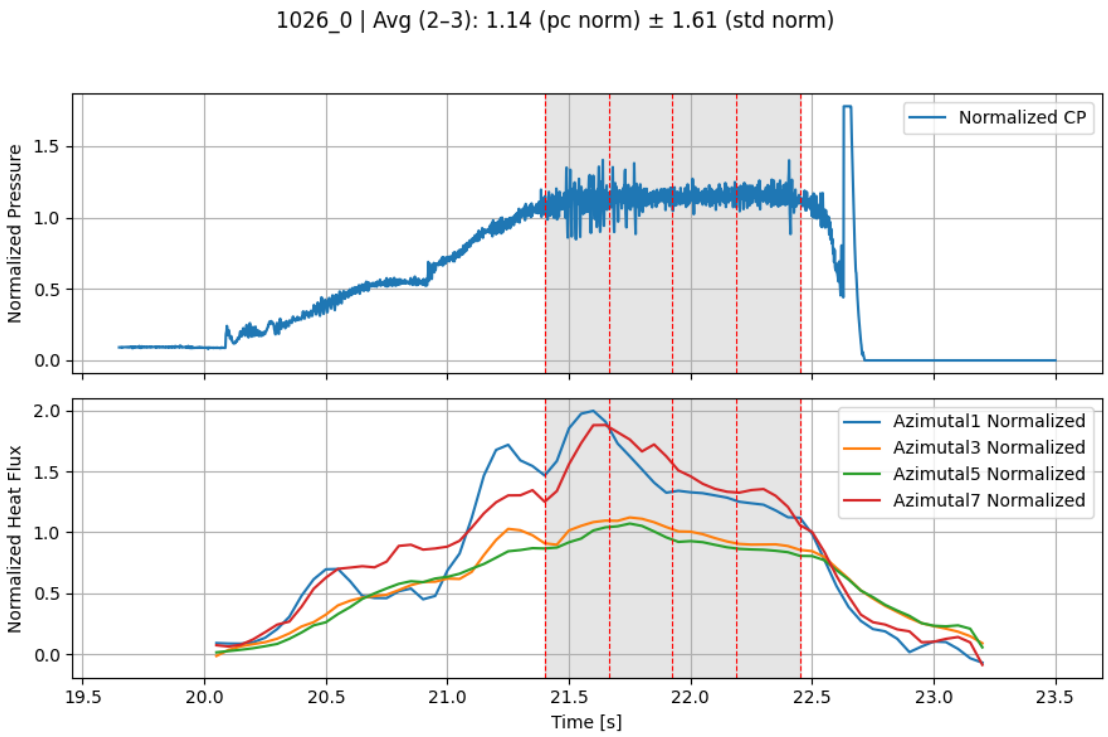

Figure C.22: Test 1026_0

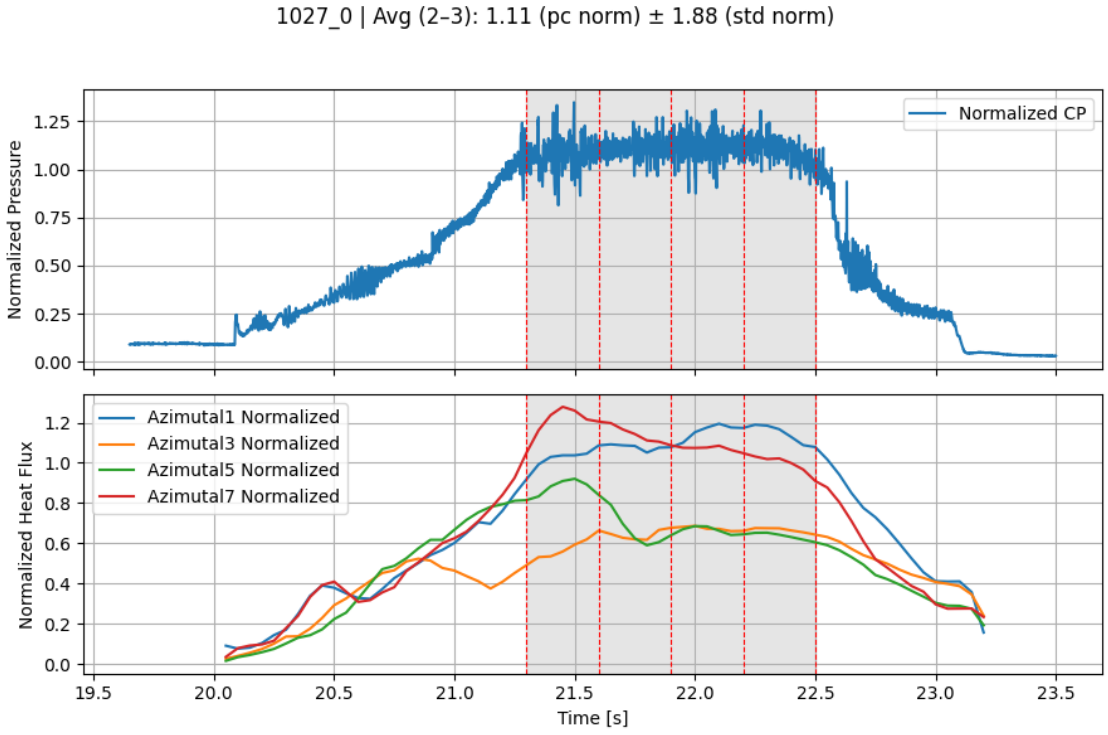

Figure C.23: Test 1027_0

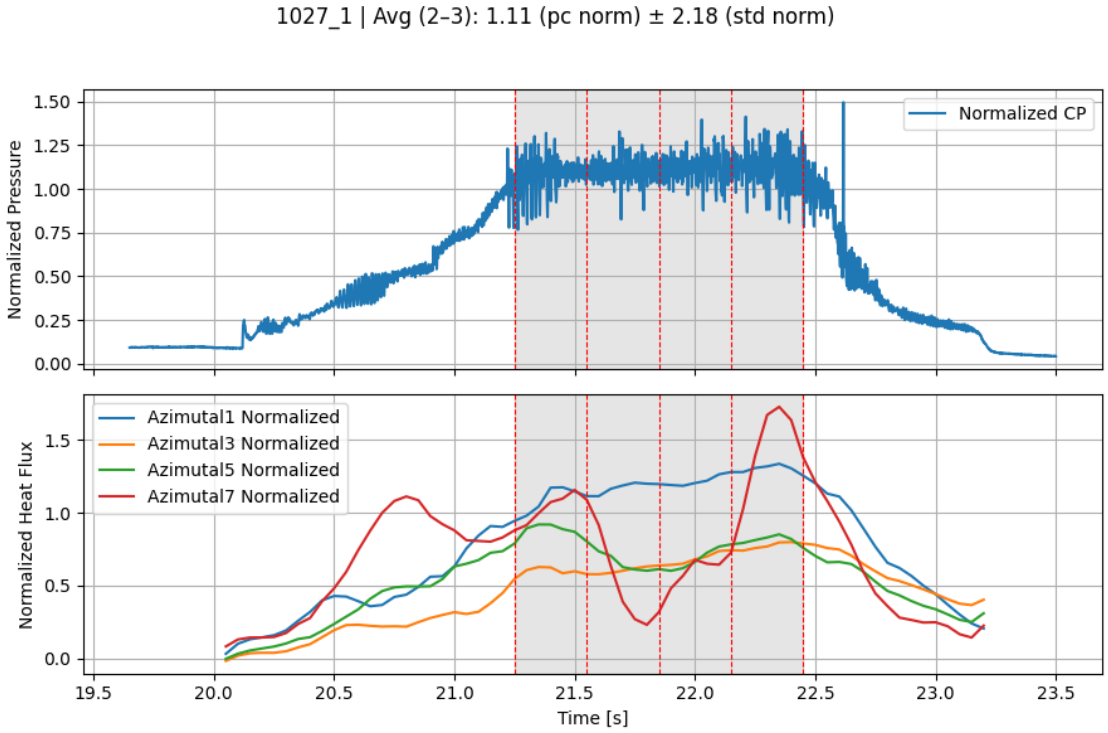

Figure C.24: Test 1027_1

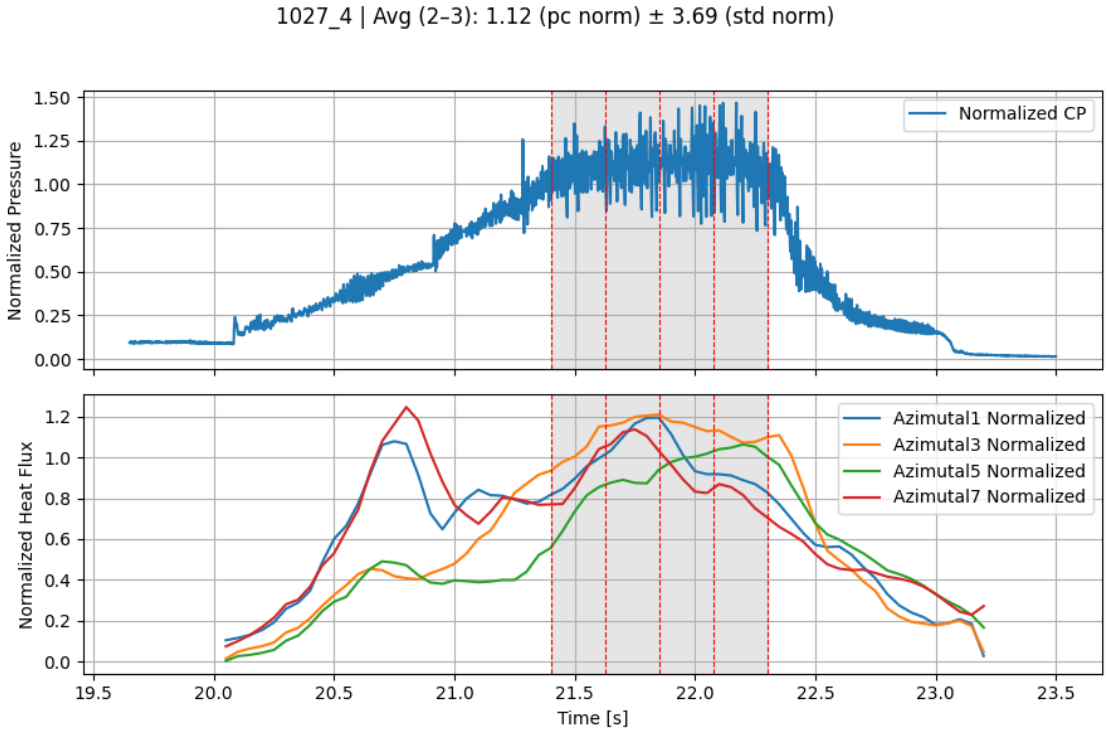

Figure C.25: Test 1027_4

D

Visual analysis by variable

D.1. Chamber fluctuations vs heat flux, First Campaign

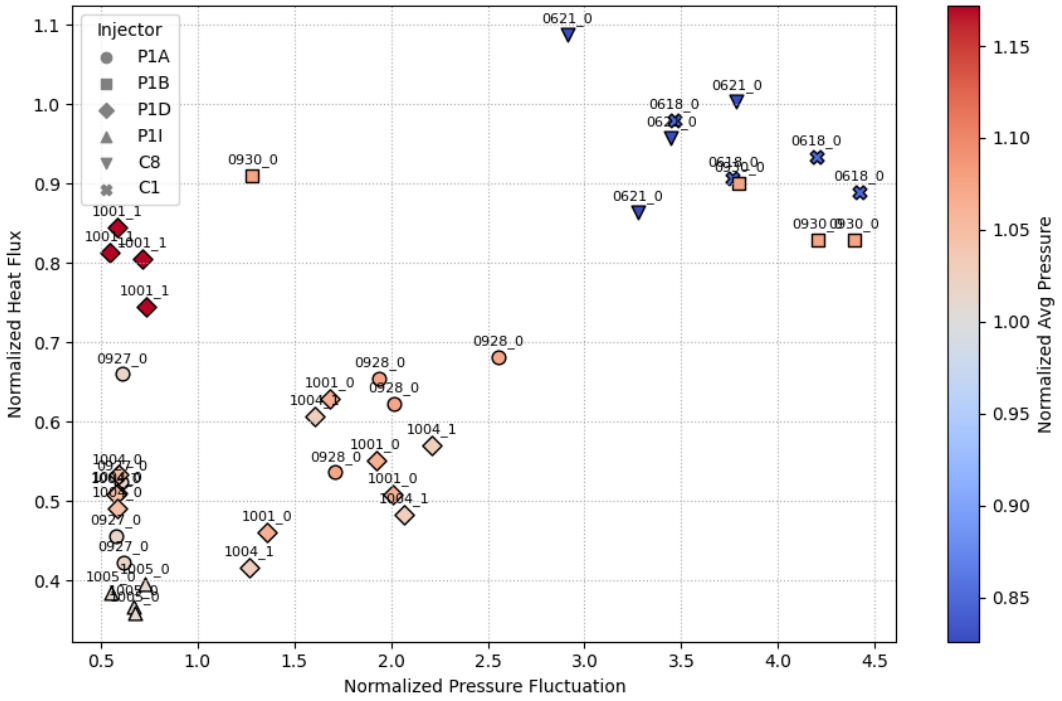

Figure D.1: Pressure fluctuation vs heat flux at azimuthal 1 in 1st Campaign, with chamber pressure colour-mapped

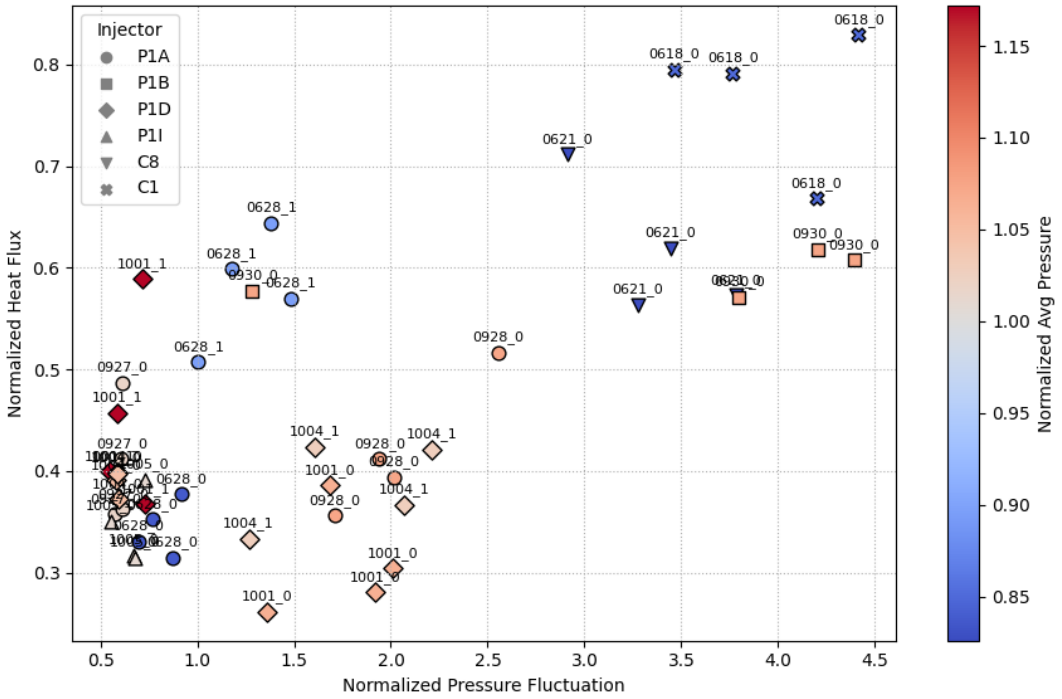

Figure D.2: Pressure fluctuation vs heat flux at azimuthal 3 in 1st Campaign, with chamber pressure colour-mapped

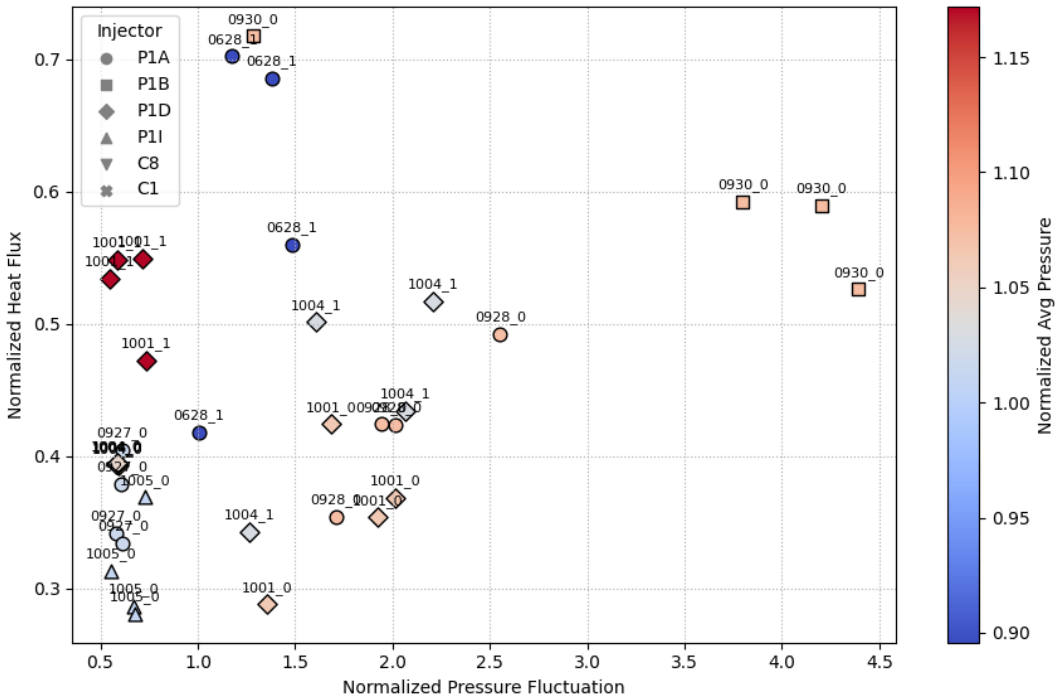

Figure D.3: Pressure fluctuation vs heat flux at azimuthal 5 in 1st Campaign, with chamber pressure colour-mapped

D.2. Chamber fluctuations vs heat flux, Second Campaign

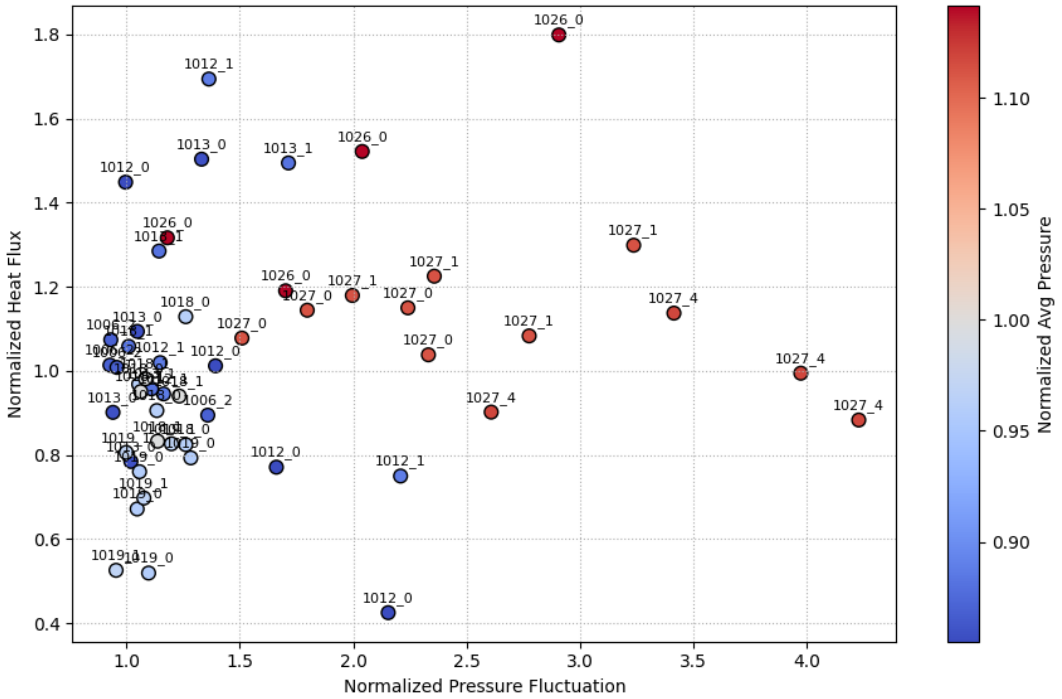

Figure D.4: Pressure fluctuation vs heat flux at azimuthal 1 in 2nd Campaign, with chamber pressure colour-mapped

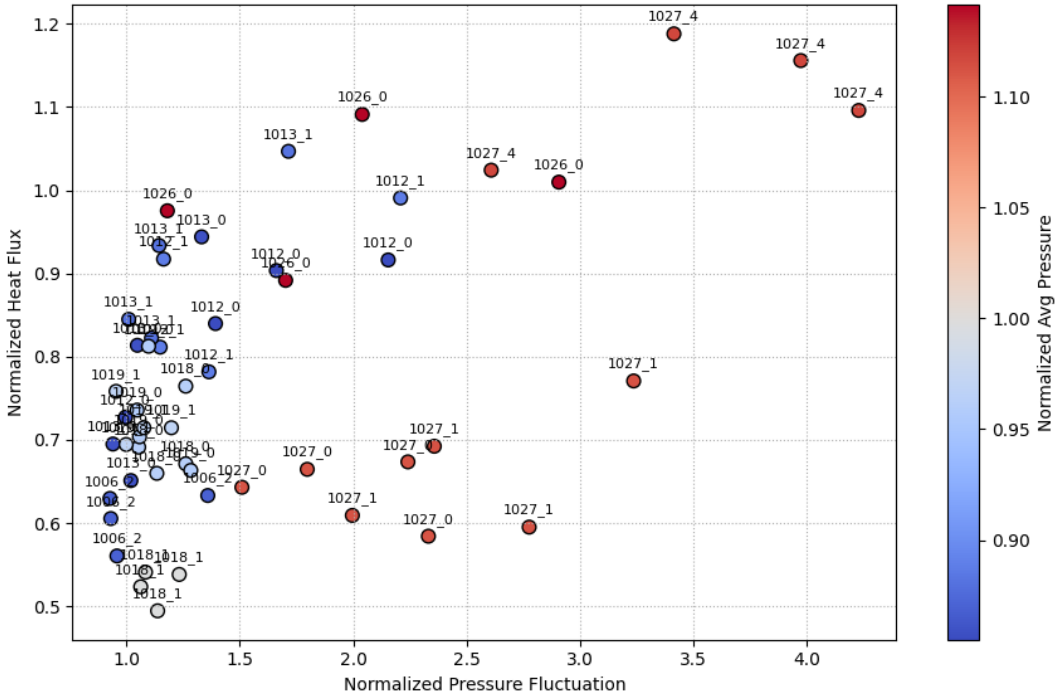

Figure D.5: Pressure fluctuation vs heat flux at azimuthal 3 in 2nd Campaign, with chamber pressure colour-mapped

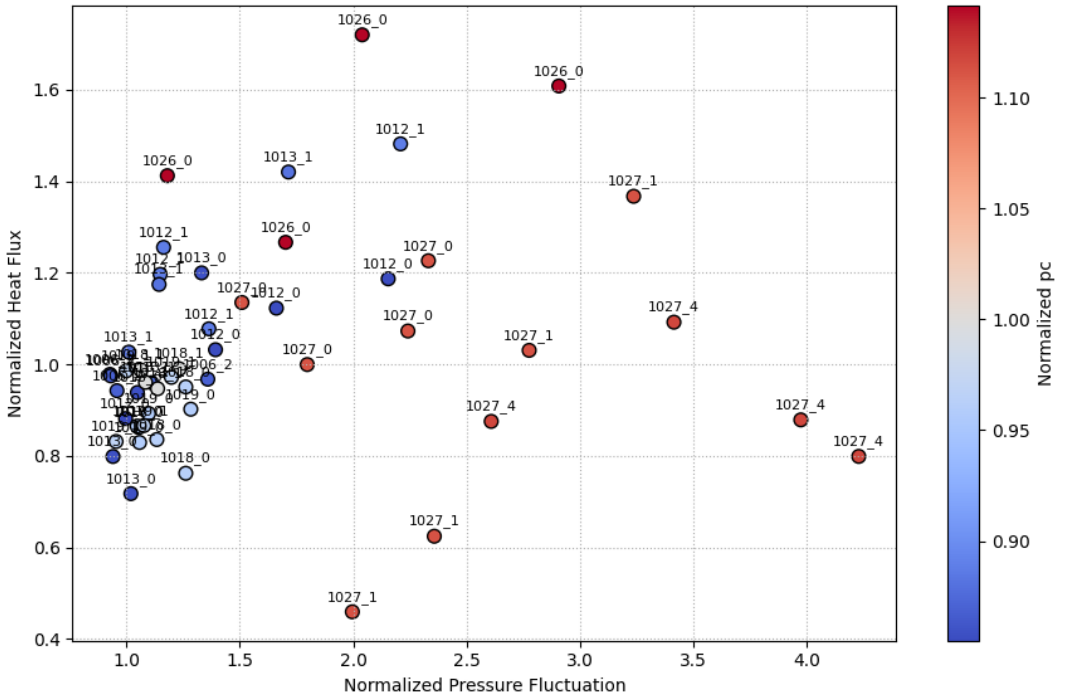

Figure D.6: Pressure fluctuation vs heat flux at azimuthal 7 in 2nd Campaign, with chamber pressure colour-mapped

D.3. Scatter plot of other variables

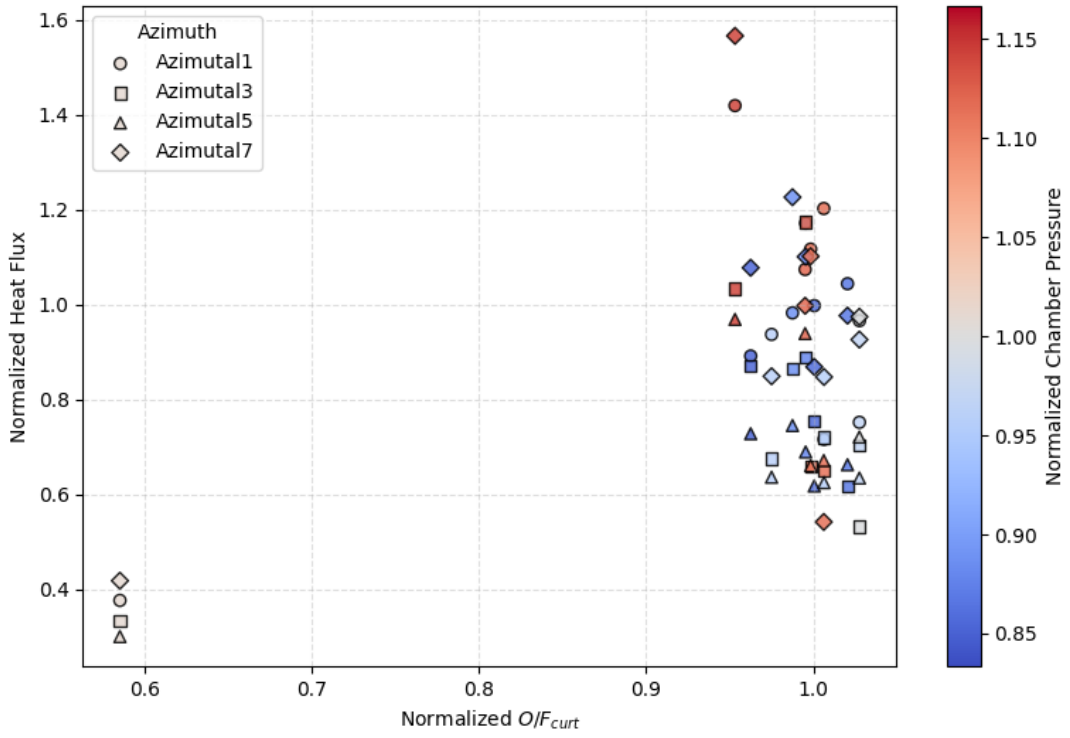

Figure D.7: O/F curtain vs heat flux in 2nd Campaign, with chamber pressure colour-mapped and azimuthal distinguished by marker shape

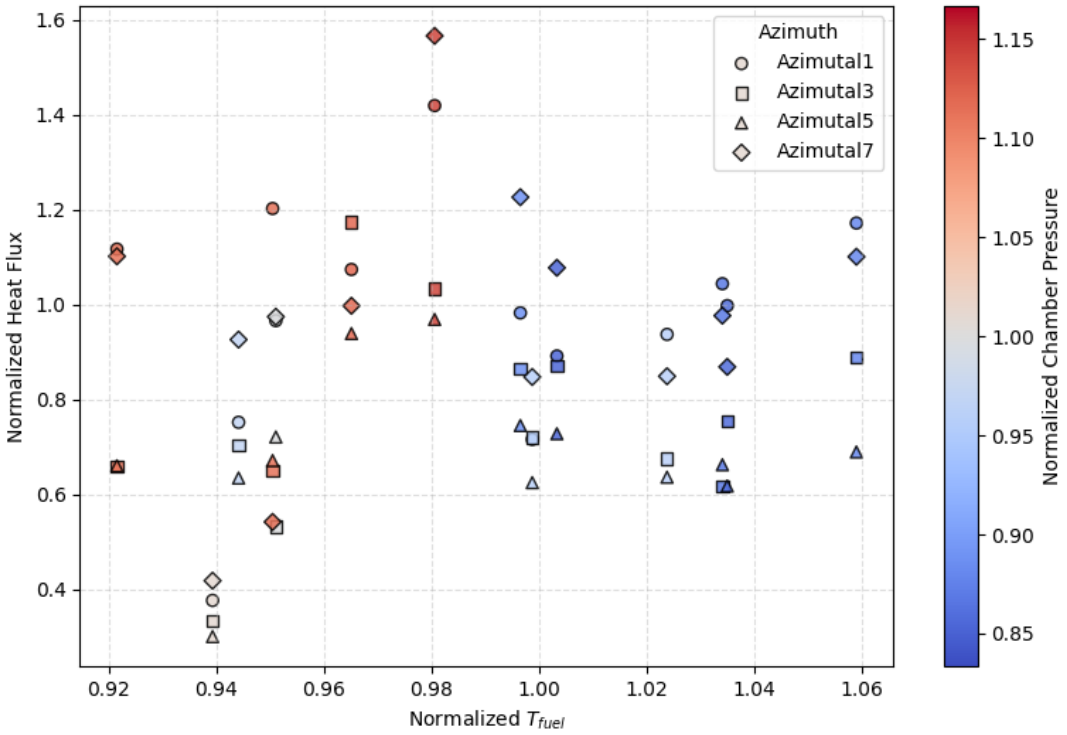

Figure D.8: Fuel temperature vs heat flux in 2nd Campaign, with chamber pressure colour-mapped and azimuthal distinguished by marker shape

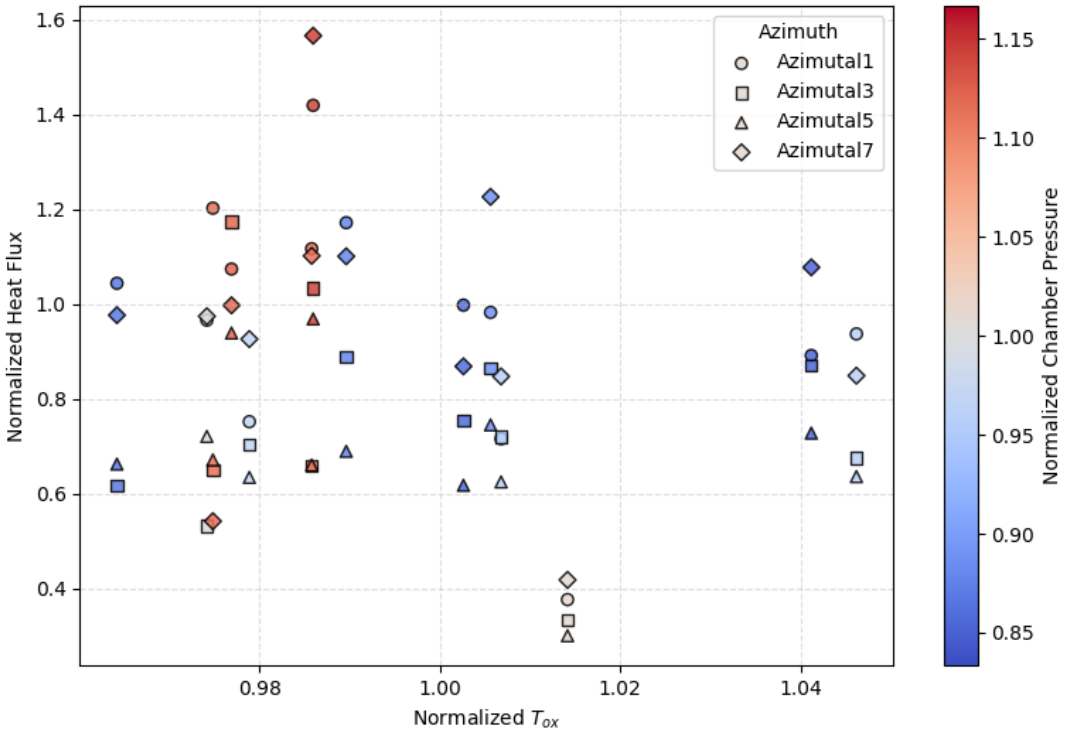

Figure D.9: Oxidizer temperature vs heat flux in 2nd Campaign, with chamber pressure colour-mapped and azimuthal distinguished by marker shape